UNIVERSITY OF CALIFORNIA
SANTA CRUZ

DOPING STRATEGIES IN METAL OXIDES: SYNTHESIS AND CHARACTERIZATION FOR ENERGY APPLICATIONS

A dissertation submitted in partial satisfaction
of the requirements for the degree of

DOCTOR OF PHILOSOPHY

in

CHEMISTRY

by

Samuel Eisenberg

June 2026

The Dissertation of Samuel Eisenberg is approved:

Professor Yat Li, Chair

Professor Jin Zhang

Professor Xiao Wang

Peter Biehl
Vice Provost and Dean of Graduate Studies

Table of Contents

List of Figures

Abstract

Doping Strategies in Metal Oxides: Synthesis and Characterization for Energy Applications

By

Samuel Eisenberg

Metal oxide semiconductors are ubiquitous in modern energy conversion, energy storage, and electronic technologies, yet their practical performance is frequently limited by poor electrical conductivity, defect-mediated charge recombination, structural instability, and thermodynamic constraints on compositional engineering. This dissertation addresses these challenges across four interconnected studies that share a common thesis: that rational manipulation of crystal defects through heteroatom doping, post-process surface treatments, and hydrogen incorporation, can unlock otherwise inaccessible performance in metal oxide systems relevant to photoelectrochemistry, multiferroics, electrochemical lithium recovery, and beyond. Chapter 2 investigates the persistent problem of dopant oxide formation in n-type doped hematite (α-Fe_2O_3), a leading photoanode and energy storage material. Through a combination of extended X-ray absorption fine structure spectroscopy, powder X-ray diffraction, and electrochemical measurements, it is shown that dopant oxide phases (SnO_2, $Fe_8Ge_3O_{18}$) form fractionally above a theoretically predicted critical dopant concentration that depends on dopant identity and synthesis temperature. Two remediation strategies are evaluated: rapid thermal quenching to kinetically trap dopants within the hematite lattice, and post-process alkaline washing

to selectively dissolve surface-segregated dopant oxides. While the washing procedure successfully removed approximately 90% of total measured dopant, it did so non-selectively, removing beneficial lattice-incorporated dopant alongside the targeted oxide phase. This resulted in degraded photoelectrochemical and energy storage performance, revealing that dopant spatial distribution (lattice-incorporated versus surface-segregated oxide) is a decisive parameter governing device performance.

Chapter 3 develops and compares four wet-chemical synthesis routes for bismuth ferrite ($BiFeO_3$, BFO), a rare room-temperature multiferroic perovskite of interest for optoelectronic, ferroelectric, photon upconversion, and energy storage applications. Potentiostatic co-electrodeposition, Pechini sol-gel deposition, solution drop-casting, and xerogel processing are evaluated for their ability to produce phase-pure, doped BFO thin films and nanoparticle powders. The xerogel route proved most versatile, reproducibly yielding phase-pure nanoparticles accommodating transition metal (Sn, Ge) and lanthanide (Yb, Er) dopants. Preliminary photoluminescence measurements of Yb/Er co-doped BFO revealed complete quenching of the near-band-edge emission, motivating further investigation of BFO as a host crystal for photon upconversion via energy transfer upconversion mechanisms. Electrochemical characterization established baseline pseudocapacitive behavior in aqueous electrolytes and demonstrated the expected multi-step conversion mechanism in lithium-ion battery configurations, while dielectric measurements revealed systematic

conductivity improvements with Sn doping consistent with small polaron hopping conduction.

Chapter 4 addresses the global challenge of lithium supply security by developing gallium-doped lithium manganese oxide ($LiMn_2O_4$, LMO) electrodes for electrochemical lithium extraction from dilute aqueous sources. Structural characterization by XRD, TEM, and XPS demonstrates that Ga^{3+} substitution at the Mn octahedral site induces measurable lattice contraction, suppresses Jahn-Teller distortion, and progressively increases the Mn^{4+}:Mn^{3+} ratio. Electrochemical evaluation in 50 mM LiCl, a concentration representative of the most dilute industrially relevant brines, reveals that LGMO-5 (5% Ga) retains 100% of its initial capacity over 100 cycles and 85% over 1000 continuous galvanostatic cycles, a dramatic improvement over undoped LMO, which loses approximately half its capacity within 100 cycles. Inductively coupled plasma optical emission spectroscopy confirms that Mn dissolution in LGMO-5 was approximately 40 times lower than in undoped LMO, directly linking the stability enhancement to suppressed Mn disproportionation. This 1000-cycle aqueous stability substantially exceeds published cycling lifetimes for doped LMO in electrochemical lithium recovery.

Chapter 5 provides a comprehensive review of hydrogen treatment methods for metal oxides and their effects on structural, optical, electronic, and magnetic properties. Post-process hydrogen annealing, proton-electron co-doping, electrochemical hydrogenation, and in-process incorporation during chemical and physical vapor deposition synthesis are critically compared. The review synthesizes evidence that

hydrogen treatment can narrow bandgaps through disorder-induced band tail states, enhance electrical conductivity through extended carrier lifetimes or improved mobilities, and even induce insulator-to-metal electronic phase transitions. Open questions regarding the long-term stability of hydrogen-induced modifications, the mechanistic distinction between surface hydrogenation and bulk interstitial doping, and the scalability of treatment processes are identified as priorities for continued research.

Collectively, this dissertation demonstrates that defect engineering is a versatile and powerful approach to overcoming intrinsic limitations of metal oxide semiconductors. The findings contribute both fundamental understanding of dopant behavior, phase stability, and defect-property relationships, and practical advances toward improved photoanodes, multiferroic materials, lithium recovery electrodes, and hydrogen-treated functional oxides.

Dedication

Dedicated to Danielle Eisendorn, Dobby, and Winky

Acknowledgements

This dissertation is the culmination of 5 years of hard work and represents one of the most trying periods of my life so far. Through this, there has been a long list of people who mentored me, inspired me, supported me, and pushed me to achieve this milestone. I would like to thank my advisor, Professor Yat Li, for giving me the opportunity to study in his lab. He has shown me seemingly endless patience and support and has always been a very kind mentor to me. I always felt I was able to ask him questions, no matter how dumb they felt, and that he was there to offer his thoughts and opinions at any time. I appreciate that he gave me freedom and trust to try things in the lab, even if many of my ideas did not pan out. He always reminded me that that is how research goes, and that an idea not working is still data that can be used to inform the next experiment.

I would also like to thank all of my colleagues in the Li lab who helped me develop as a researcher and as a person. My first grad student mentor, Mingpeng Chen, did a great job welcoming me to the lab and handing off his project that would become my main focus throughout my 5 years here. I did not know exactly what to expect in grad school and Mingpeng was the first to really show me the day to day life. Anica Pinongcos also modeled hard work and welcomed me with open arms. From working on the same project and having desks next to each other, she really helped me integrate into the lab early on. She also was always willing to show me something new, find some lab supply, analyze data, etc. all without a complaint. I joined the lab alongside 4 other first-years, Xinzhe Xue, Qiu Ren, Ella Davidi, and Riley Ball, and it

was a great honor to learn together. All have become good friends, and I will miss hanging around the office talking whatever nonsense. Each has been so generous with their time and energy, teaching me new electrochemical or X-Ray diffraction techniques, or offering to help out with an experiment when I got busy. Later lab members, Nathan Delaney and Cassidy Tran have also become like family. We spent a lot of time laughing together and talking about books or movies. A welcome break from lab work.

I would like to thank my family who had to listen to me complain for 5 years (and really, my whole life). My parents who never stopped believing in me, often treating my complaints with such nonchalance as to say “meh, it’ll all work out”, or “you’re doing just fine”. They always seemed so sure that I would pull this off, bearing no concern at all. That always helped me to recenter myself and look at the bigger picture. Both have influenced me greatly, fostering my interest in science, and especially chemistry from a young age. When people ask about why the hell I would want to do something like this, the first thing that comes to mind is when my dad had me help test some water samples he had from work. And every time he struggled to pronounce phenolphthalein. Seeing my mom start a whole new chapter in life, going back to school and working in a field that she missed was also a huge inspiration. My brother, having started his PhD at the same time, offered an opportunity for some friendly competition. I am very proud of the work he has done and thankful for all of the laughter and commiseration that he has offered me. My late grandfather, who passed so recently, showed me what it meant to live life to the fullest. Nobody knows

the meaning of life, but I always felt like if anybody might've had a clue, it was him. I often thought of him when I decided to take time away from school and treat myself. His wife has also always been so generous to me and always felt like my grandmother.

Of course, the biggest support for me has been Dani who I can very soon call my wife. We have grown and learned and changed together in a way that not many people get to experience. I will be forever grateful for her sacrifice to come to Santa Cruz with me. She never once hesitated to support me while I tried for this, even if it made her time in school and early career a little bit harder. I am grateful for the many hours she has let me vent and for all the effort she has given to keep me smiling and keep me movin'. I laugh and laugh and laugh with her and sing karaoke and dance until 3 am whenever I need a break from it all. I certainly could not have done this without her by my side. She muses about getting her PhD one day, and I often discourage it in my miserly way, but I hope that I can repay the great patience and support she has afforded me. Her mother, like a second mom to me, and many of her extended family have also been amazing support. Their generosity and genuine care always made me feel like I had a whole section of bleachers cheering me on.

And lastly, I would like to thank all of my pets who have loved me unconditionally (at least those capable of something like love). Tim, Lucy, Molly, P, and the many others from years past helped get me to grad school. They weren't around to see it through, but I know they would be proud. Dobby and Winky joined me after I started and have been hugged and squeezed and pet enough for a lifetime already. Thanks!

This dissertation includes reprints of the previously published material:

1. **Eisenberg, S.**, Li, Y. Hydrogen Treatment of Metal Oxides: Methods, Mechanisms, and Implications. *J. Phys. Chem. C* **2025**, 129, 19, 8817-8831

Chapter 1

Introduction to Metal Oxide Design, Synthesis, and Applications

1.1 Metal Oxide Semiconductors

Metal oxides (MOs) constitute one of the broadest and most technologically important classes of inorganic compounds. Their electronic properties arise from the bonding between electropositive metal cations and electronegative oxygen anions, producing electronic band structures that span from wide-gap insulators (Al_2O_3, $E_g \approx 9$ eV) through moderate-gap semiconductors (α-Fe_2O_3, $E_g \approx 2.0$ eV; $BiFeO_3$, $E_g \approx 2.5$ eV; TiO_2, $E_g \approx 3.2$ eV) to metallic conductors (RuO_2).[1–3] In most semiconducting MOs, the occupied valence band is primarily composed of O 2p orbitals hybridized with metal d or s states, while the unoccupied conduction band is primarily composed of the metal's d (for transition metals) or s (for main group metals) orbitals.[2–4] The magnitude of the bandgap, defined as the energy difference between the valence band maximum (VBM) and conduction band minimum (CBM), governs whether the material absorbs visible light, conducts electricity under ambient conditions, and can drive electrochemical reactions when photoexcited.

Charge transport in MO semiconductors proceeds through mechanisms distinct from those in conventional covalent semiconductors like Si or GaAs. In many transition metal oxides, particularly those with localized d-electron character such as Fe_2O_3 and $LiMn_2O_4$, the dominant charge carriers are small polarons rather than delocalized band electrons.[5–7] A small polaron is a charge carrier (electron or hole)

that locally distorts the surrounding lattice, creating a potential well that localizes the carrier at a single atomic site. Transport then proceeds by thermally activated hopping between adjacent sites, described by a hopping mobility of the form:

$$\mu_{hop} \propto \frac{1}{T} e^{-E_a/k_B T} \quad \text{(Eq. 1.1)}$$

where E_a is the activation energy for hopping, k_B is the Boltzmann constant, and T is temperature.[8] This thermally activated behavior contrasts with band-like transport in covalent semiconductors where mobility typically decreases with temperature due to phonon scattering. The polaron hopping mechanism has direct consequences for device performance: it means that bulk conductivity in materials like hematite ($\sigma \approx 10^{-14}$ S cm^{-1}) is intrinsically poor and cannot be improved simply by increasing crystallinity but rather requires increasing the density of available hopping sites through the introduction of aliovalent dopants or oxygen vacancies.[7,8]

Point defects, vacancies, interstitials, substitutional impurities, and antisites, play a governing role in MO properties because they introduce electronic states within the bandgap, modify the Fermi level position, alter local bonding environments, and create strain fields that influence ion transport.[9–11] The deliberate introduction or manipulation of these defects, broadly termed defect engineering, is the primary strategy by which MO semiconductors are tailored for specific applications. This dissertation investigates three principal defect engineering approaches: heteroatom doping, post-process surface treatments, and hydrogen incorporation; compared across four MO systems of current technological

importance. α-Fe_2O_3, $BiFeO_3$, $LiMn_2O_4$, as well as a host of other MOs are studied and discussed as defect engineering candidates.

1.2 Heteroatom Doping

Heteroatom doping is the intentional substitution of a fraction of host lattice cations with foreign ions and is the most widely employed defect engineering strategy in MO semiconductors.[6,9,11–15] The electronic consequences of doping depend on the charge state of the dopant relative to the host ion it replaces. In the Kröger-Vink notation used for defect chemistry in ionic solids, substitution of a trivalent host cation (e.g., Fe^{3+} in α-Fe_2O_3) with a tetravalent dopant (e.g., Sn^{4+}, Ge^{4+}, Ti^{4+}, Si^{4+}) creates a positively charged defect site that is compensated by an additional conduction electron, effectively acting as a one-electron donor:[11,14,16,17]

$$Sn^{4+} \rightarrow Sn_{Fe}^{\bullet} + e'$$

This increases the free electron (or small polaron) concentration, n, which in turn increases the electrical conductivity (σ):

$$\sigma = ne\mu \qquad \text{(Eq. 1.2)}$$

where μ is the carrier mobility and e is the fundamental charge . In the Mott-Schottky framework used to characterize semiconductor-electrolyte junctions, the donor density N_D is extracted from the inverse-square capacitance versus potential relationship:[18,19]

$$\frac{1}{C^2} = \left(\frac{2}{\varepsilon\varepsilon_0 e N_D}\right) \times \left(V - V_{fb} - \frac{k_B T}{e}\right) \quad \text{(Eq. 1.3)}$$

where C is the space charge capacitance, V is the applied potential, and V_{fb} is the flat-band potential, and ε and ε_0 are the permittivity and vacuum permittivity, respectively. The slope of a $\frac{1}{C^2}$ versus V plot is inversely proportional to N_D, providing a direct measure of the effectiveness of doping. Increases in N_D of 2–3 orders of magnitude have been reported for optimally doped hematite compared to pristine material.[11,14,16,20–22]

Isovalent doping, substitution with an ion of the same formal charge, does not directly alter carrier concentration but can stabilize crystal structures, modify bond lengths, and suppress irreversible or unwanted phase transitions. This is particularly important in spinel oxides such as $LiMn_2O_4$, where trivalent dopants (Al^{3+}, Ga^{3+}, Cr^{3+}) substituting for Mn^{3+} maintain the same formal charge but force the charge compensation onto the remaining Mn population, effectively oxidizing Mn^{3+} to Mn^{4+} to maintain electroneutrality:[23,24]

This has profound structural implications because Mn^{3+} (d^4, high spin) in an octahedral crystal field of relatively weak-field O^{2-} ligands experiences Jahn-Teller distortion. The octahedral crystal field splits the five d orbitals into a lower t_{2g} triplet and an upper e_g doublet. With four d electrons in the high-spin configuration ($t_{2g}^3\ e_g^1$), the single electron in the doubly degenerate e_g manifold breaks orbital degeneracy through a tetragonal elongation of the octahedron (Jahn-Teller effect), weakening the Mn—O bonds along the elongated axis and ultimately causing lattice instability

during cycling.[25,26] By contrast, Mn^{4+} (d^3, t_{2g}^3 e_g^0) has no e_g occupancy and therefore no Jahn-Teller distortion, making it structurally more stable. This principle of suppressing Jahn-Teller distortion by increasing the Mn^{4+}:Mn^{3+} ratio through doping is the fundamental mechanism behind most doping strategies for LMO stabilization, as explored in Chapter 4.

However, doping is constrained by the thermodynamic solubility of the dopant in the host lattice. In ionic oxides, aliovalent dopants experience elastic strain (due to ionic radius mismatch with the host site) and electrostatic interactions (due to the effective charge of the substitutional defect) that provide a driving force for segregation toward grain boundaries and free surfaces at elevated temperatures.[27–29] When the total dopant concentration exceeds a critical solubility limit (which is a function of dopant identity, temperature, oxygen partial pressure, and the elastic and electrostatic properties of the host lattice) the excess dopant precipitates as a secondary oxide phase. In hematite, this manifests as SnO_2, GeO_2 (or the more complex $Fe_8Ge_3O_{18}$), or TiO_2 overlayers on the hematite surface.[5,30] These dopant oxide phases can passivate catalytic surface sites, introduce additional recombination centers, impede hole transfer to the electrolyte, and reduce optical absorption—paradoxically degrading the very properties that doping was intended to improve.[31] The relationship between dopant concentration, synthesis temperature, and dopant oxide fraction is the central subject of Chapter 2.

1.3 Hematite (α-Fe_2O_3)

Hematite crystallizes in the corundum structure (space group $\bar{R}$ 3c) with Fe^{3+} ions occupying two-thirds of the octahedral interstices in a hexagonal close-packed oxygen sublattice.[32] Its bandgap of 1.9–2.2 eV enables absorption of approximately 40% of the solar spectrum, yielding a theoretical maximum photocurrent density of ~12.6 mA cm^{-2} and a solar-to-hydrogen efficiency approaching 15% under AM 1.5G illumination.[11,33–35] Beyond PEC water splitting, hematite's high ideal theoretical capacitance of 3625 F g^{-1} (based on the Fe^{3+}/Fe^{2+} and Fe^{3+}/Fe^{0} redox couples), non-toxicity, and crustal abundance make it attractive for electrochemical energy storage.[36–39]

Despite these intrinsic advantages, practical hematite performance is severely limited. Charge transport proceeds via small polaron hopping along the basal plane of the corundum structure, with the activation energy for hopping approximately 0.1 eV and an intrinsic bulk conductivity of only ~10^{-14} S cm^{-1} at room temperature.[7,8] The minority carrier (hole) diffusion length is 2–4 nm. This is roughly two orders of magnitude shorter than the optical absorption depth of ~100 nm at visible wavelengths, meaning that the vast majority of photogenerated holes recombine before reaching the electrolyte interface.[19,32,40] Surface charge transfer kinetics for the oxygen evolution reaction are slow, requiring significant overpotentials, and surface states act as recombination centers that pin the Fermi level and reduce photovoltage.[41,42] In the supercapacitor context, the same poor conductivity limits the

actual specific capacitance to 120–320 F g^{-1}, less than 10% of the theoretical value.[43,44]

n-type doping with tetravalent cations (Sn^{4+}, Ge^{4+}, Ti^{4+}, Si^{4+}) directly addresses the conductivity limitation by introducing donor electrons into the polaron transport network, increasing N_D by up to three orders of magnitude and improving photocurrent densities by factors of 100–300× over pristine hematite. Tin is particularly ubiquitous because Sn^{4+} diffuses unintentionally from fluorine-doped tin oxide (FTO) substrates into hematite during the high-temperature annealing (>700 °C) required for crystallization, a process that has been termed "self-doping".[45–48] Germanium has emerged as an especially promising alternative dopant because density functional theory (DFT) calculations predict that Ge has higher thermodynamic solubility in hematite than either Si or Sn, due to a favorable combination of ionic radius (Ge^{4+} = 0.53 Å, compared to Fe^{3+} = 0.645 Å in high spin) and a low formation enthalpy for the secondary phase GeO_2.[28,30,49]

The critical complication is that dopant solubility in hematite is finite and strongly temperature-dependent. Computational studies in this research group have established that a critical dopant concentration exists for each dopant–temperature combination, above which excess dopant precipitates as its native oxide phase rather than incorporating substitutionally into the Fe^{3+} site.[5] For example, at 900 °C in air, the predicted critical concentrations are approximately 0.52 at.% for Sn and 1.00 at.% for Ge; at 1000 °C, these increase to 1.11% and 2.02%, respectively. EXAFS characterization has confirmed that above these thresholds, the fraction of dopant

found in the oxide phase increases logarithmically with total dopant loading, while substitutional incorporation continues fractionally. This fractional co-existence of doped and precipitated dopant, rather than a sharp cutoff, motivates the strategies investigated in Chapter 2: rapid thermal quenching to kinetically trap dopants above the equilibrium solubility limit, and post-process alkaline washing to selectively dissolve the precipitated oxide phase while preserving the beneficial lattice-incorporated dopant.

1.4 Bismuth Ferrite ($BiFeO_3$, BFO)

Bismuth ferrite crystallizes as a rhombohedrally distorted perovskite of the general formula ABO_3 (space group R3c), where the large Bi^{3+} ion occupies the 12-fold coordinated A-site and the smaller Fe^{3+} ion occupies the 6-fold coordinated (octahedral) B-site.[50–53] BFO is one of very few single-phase materials exhibiting simultaneous ferroelectric and magnetic ordering at and well above room temperature, making it the prototypical magnetoelectric multiferroic.[54–57] Its ferroelectricity originates from the stereochemically active $6s^2$ lone pair of the Bi^{3+} ion, which creates an asymmetric charge distribution that displaces Bi^{3+} from its centrosymmetric position, breaking inversion symmetry and producing a large spontaneous polarization (~100 μC cm^{-2}) along the [111] pseudocubic direction.[54,57,58] This mechanism is categorized as a “proper” or Type-I ferroelectric, where the polar distortion is the primary order parameter. The antiferromagnetism arises independently from the Fe^{3+} sublattice: each Fe^{3+} (d^5, high spin, S = 5/2) possesses five unpaired electrons whose spins couple antiferromagnetically to

neighboring Fe^{3+} ions through superexchange interactions mediated by bridging O 2p orbitals along the Fe–O–Fe bonds.[55,59,60] This produces G-type antiferromagnetic ordering (each Fe spin antiparallel to all nearest neighbors) with a Néel temperature $T_N \approx 640$ K.[52,55] Because the ferroelectricity and antiferromagnetism originate from different sublattices (Bi^{3+} lone pair vs. Fe^{3+} d-electron ordering), the coupling between them is weak—a common characteristic of Type-I multiferroics that limits the magnitude of magnetoelectric effects but permits both orders to persist to high temperatures.[54,57]

The multiferroic character is of practical interest because magnetoelectric coupling, even if weak, in principle allows electric-field control of magnetic states and vice versa. This has implications for low-power magnetic memory, spintronic logic, and sensor technologies that exploit the additional degrees of freedom offered by coupled order parameters.[56,61,62] Moore's Law, the empirical observation that transistor density doubles approximately every 1–2 years, has held for over five decades but is approaching fundamental physical limits as feature sizes approach the atomic scale.[63,64] Materials like BFO that enable information encoding in ferroelectric polarization or magnetic spin orientation, rather than solely in charge, offer alternative pathways for continued scaling of information density.

BFO also possesses a moderate bandgap of approximately 2.1–2.7 eV (depending on morphology, crystallinity, and measurement method) arising from a valence band of hybridized O 2p / Fe 3d / Bi 6s,6p orbitals and a conduction band dominated by Fe 3d states.[65–67] This enables visible-light absorption for PEC and

photovoltaic applications. Importantly, the ferroelectric polarization in BFO provides an internal electric field that can enhance photogenerated charge separation beyond what band bending alone achieves in conventional semiconductor junctions.[68–70] The direction and magnitude of this polarization become critical variables, motivating the study of oriented thin films and the effects of doping on ferroelectric properties.

This dissertation proposes and provides preliminary investigation of a novel application: BFO as a host crystal for lanthanide-based photon upconversion (UC). UC is an anti-Stokes process in which sequential absorption of two or more low-energy photons results in emission of a single higher-energy photon, thereby converting sub-bandgap radiation into usable above-bandgap light.[71–74] The most technologically relevant UC mechanism is energy transfer upconversion (ETU), in which a "sensitizer" ion (typically Yb^{3+}, which has a single excited state $^2F_{5/2}$) absorbs a near-infrared photon (~980 nm), transfers the energy non-radiatively to a neighboring "activator" ion (e.g., Er^{3+}, Ho^{3+}, Tm^{3+}), whose ladder-like 4f energy levels allow sequential excitation to higher states and subsequent radiative relaxation at visible or UV wavelengths.[73,75,76] The rate of competing non-radiative relaxation, depends exponentially on the ratio of the energy gap between adjacent levels to the maximum phonon energy of the host. Minimizing non-radiative losses therefore requires host crystals with low phonon energy. Oxide matrices are moderate in this regard compared to fluorides but offer superior chemical and thermal stability. BFO offers three specific advantages as a UC host: (1) the large A-site can accommodate trivalent lanthanide ions (Yb^{3+}: 0.87 Å; Er^{3+}: 0.89 Å) with radii comparable to Bi^{3+}

(1.03 Å), enabling substitutional doping at high concentrations; (2) the noncentrosymmetric crystal field partially relaxes the Laporte selection rule that forbids f–f transitions, increasing transition probabilities and UC efficiency; and (3) as a photoactive semiconductor, BFO could in principle convert the UC emission internally for photocurrent generation, creating a self-sensitized spectral extension scheme.[71,77,78] Chapter 3 develops the wet-chemical synthesis routes needed to produce lanthanide-doped BFO and presents preliminary optical characterization.

Beyond multiferroics and optoelectronics, BFO has attracted interest as an energy storage material. In aqueous electrolytes, the Fe^{3+}/Fe^{2+} redox couple and partial Bi redox activity provide Faradaic pseudocapacitance with reported specific capacitances of 80–260 F g^{-1}.[79–81] In lithium-ion battery configurations, BFO undergoes a conversion reaction, followed by sequential Li–Bi alloying steps, providing an exceptionally high theoretical capacity through multi-electron reactions but suffering from the irreversibility inherent to conversion mechanismd.[82,83] These electrochemical applications are explored in Chapter 3 alongside the multiferroic and optical characterization.

A persistent challenge across all BFO applications is that wet-chemical synthesis of phase-pure material is non-trivial. The volatility of bismuth at the annealing temperatures (≥550 °C) required for perovskite formation, combined with the thermodynamic stability of competing phases (Bi_2O_3, Fe_2O_3, $Bi_2Fe_4O_9$, $Bi_{25}FeO_{40}$), makes stoichiometric control and phase purity highly sensitive to precursor chemistry, annealing profile, and atmosphere.[84–86] Most high-quality BFO

reported in the literature is grown by vacuum deposition techniques (pulsed laser deposition, molecular beam epitaxy, sputtering) that are costly, substrate-limited, and difficult to scale.[55,87–90] Developing accessible wet-chemical routes that can accommodate dopant incorporation while maintaining phase purity is an essential enabling objective.

1.5 Lithium Manganese Oxide ($LiMn_2O_4$, LMO)

The global transition toward electrified transportation and grid-scale energy storage has made lithium one of the most strategically critical elements of the twenty-first century. Global battery demand surpassed 1.0 TWh in 2024 and is projected to reach 4.2 TWh by 2030, with lithium demand expected to grow eightfold by 2040 under net-zero scenarios.[91–93] Conventional lithium extraction from continental brines (solar evaporation, 12–18 months) and hard-rock spodumene ores (sulfuric acid roasting at >1000 °C) are environmentally damaging, water-intensive, and incapable of accessing the vast lithium reserves in geothermal brines, produced waters, and seawater.[94–97]

Electrochemical lithium extraction (ELE) exploits the selective intercalation of Li^+ into battery-type cathode materials to concentrate lithium from dilute solutions.[98–100] The approach offers high selectivity arising from the size-selective intercalation sites in the electrode crystal structure, rapid kinetics (minutes to hours rather than months), low energy consumption, and minimal chemical waste compared to conventional methods.[100–102] Among candidate electrode materials, spinel $LiMn_2O_4$

(LMO) has attracted particular attention due to its three-dimensional Li^+ diffusion pathways through the interconnected tetrahedral 8a sites of the Fd̀3m spinel structure, its low cost from earth-abundant Mn, and its high theoretical Li^+ adsorption capacity of 35–60 mg g^{-1}.[100,103,104] The tetrahedral 8a sites are size-selective: the ionic radius of Li^+ (0.76 Å) matches the site geometry, while competing cations such as Na^+ (1.02 Å), K^+ (1.38 Å), Mg^{2+} (0.72 Å), and Ca^{2+} (1.00 Å) are either too large or possess prohibitively high hydration energies that disfavor desolvation and intercalation.[100,104]

The de/intercalation of Li^+ in LMO proceeds through a two-step reaction that maintains the spinel framework as the delithiated λ-MnO_2 phase. However, two persistent degradation mechanisms severely limit LMO's practical deployment in aqueous environments. First, the Mn^{3+} disproportionation reaction:

$$2Mn^{3+}_{(s)} \rightarrow Mn^{4+}_{(s)} + Mn^{2+}_{(aq)} \qquad \text{(Eq. 1.4)}$$

dissolves Mn^{2+} into the electrolyte, progressively depleting the electrochemically active material and causing irreversible capacity loss.[105,106] This dissolution is accelerated in aqueous environments by proton-assisted mechanisms and the high solvation capacity of water for Mn^{2+} ions compared to organic battery electrolytes.[106,107] Second, as described above, the Jahn-Teller distortion of octahedrally coordinated high-spin Mn^{3+} (d^4) causes tetragonal lattice deformation that accumulates over cycling, degrading structural coherence and further weakening Mn–O bonds along the distorted axes.[26,108] Together, these mechanisms cause LMO to lose approximately 50% of its initial capacity within 100 cycles in aqueous

electrolyte, a degradation rate incompatible with the thousands of cycles required for industrial ELE deployment.[106,107,109,110]

Heteroatom doping addresses both degradation pathways through a single mechanism: partial substitution of Mn with a stable trivalent cation (Ga^{3+}, Al^{3+}, Cr^{3+}) reduces the total Mn^{3+} population and forces charge compensation by oxidizing remaining Mn^{3+} to Mn^{4+}, simultaneously suppressing Jahn-Teller distortion and reducing the Mn^{3+} available for disproportionation.[23,24,111–117] Additionally, the typically smaller ionic radius of the dopant (Ga^{3+}: 0.62 Å vs. Mn^{3+} high spin: 0.645 Å) contracts the lattice, shortening and strengthening Mn–O bonds, and can narrow diffusion channels to improve selectivity for Li^+ over larger competing cations, though at the cost of increased kinetic resistance to Li^+ transport at high doping levels.[23,104,111] Chapter 4 investigates Ga doping of LMO as a strategy to achieve the long-cycle stability needed to bridge the gap between laboratory demonstrations and industrial electrochemical lithium recovery.

1.6 Hydrogen Treatment of Metal Oxides: Mechanisms and Effects

Hydrogen interacts with MO semiconductors through two primary mechanisms that produce distinct but often concurrent effects.[3,118] The first is chemical reduction: molecular H_2 adsorbs and dissociates on the MO surface, and the resulting atomic hydrogen reacts with lattice oxygen to form water, creating an oxygen vacancy (V_O) and reducing nearby metal cations to maintain local charge neutrality:

$$MO + H_2 \rightarrow M + H_2O + V_O \quad \text{(Eq. 1.5)}$$

The energy required to form an oxygen vacancy (E_v) correlates with the free energy of formation and M—O strength of the MO, and is phase-dependent for polymorphic oxides.[119,120] The resulting V_O acts as a two-electron donor, introducing occupied states near the CBM that increase carrier concentration and conductivity. However, V_O can also act as recombination centers for photogenerated carriers, creating a tradeoff between improved conductivity and reduced carrier lifetime that depends sensitively on V_O concentration and spatial distribution.[10,121]

The second mechanism is interstitial hydrogen incorporation, in which atomic hydrogen diffuses into the MO lattice and forms covalent O—H bonds (observable as the characteristic O—H stretch mode at ~3279 cm^{-1} in infrared spectroscopy).[122,123] The interstitial hydrogen atom donates its electron to neighboring metal cations, acting as a shallow donor and shifting the Fermi level toward the CBM. Theoretical studies have demonstrated that hydrogen doping can not only introduce mid-gap states but also partially populate conduction band edge states; when the conduction band occupancy exceeds a critical threshold, an insulator-to-metal transition can occur under ambient conditions.[124,125] This has been demonstrated computationally and experimentally for TiO_2, VO_2, ZnO, and other oxides.[125–129]

Methods of hydrogen treatment span a wide range of conditions. Post-process hydrogen annealing (200–1200 °C in H_2 or H_2/Ar atmospheres) is the most common

approach and was used in the seminal 2011 study by Chen et al. that demonstrated "black TiO_2" with a bandgap narrowed to ~1.5 eV through disorder-induced band tail states.[130] Electrochemical hydrogenation, in which the MO serves as the cathode in an aqueous electrolytic cell, introduces hydrogen species at ambient temperature but often produces transient rather than stable modifications.[123,131] The proton-electron co-doping strategy, in which a MO is placed in contact with a metal of lower work function in an acid solution, drives simultaneous injection of electrons from the metal and protons from the acid into the MO lattice, enabling room-temperature bulk hydrogenation.[128,132] In-process incorporation during chemical synthesis or physical vapor deposition introduces hydrogen during crystal growth, potentially achieving more uniform bulk distribution.[133–136] Chapter 5 provides a comprehensive review of these methods, synthesizes evidence for their structural, optical, electronic, and magnetic effects, and identifies the critical open questions regarding mechanism, stability, and scalability.

1.7 Photoelectrochemical Water Splitting

Many of the MO systems discuss herein are discussed in the context of their application in photoelectrochemical (PEC) reactions. Therefore, it is important to discuss the general process and most common case in the literature. PEC water splitting is a process in which a semiconductor photoelectrode absorbs solar photons to generate electron-hole pairs that drive the thermodynamically uphill decomposition of water into molecular hydrogen and oxygen. The overall reaction:

$$2H_2O \rightarrow 2H_2 + O_2 \qquad \text{(Eq. 1.6)}$$

requires a minimum Gibbs free energy input of $\Delta G° = 237.2$ kJ mol^{-1}, corresponding to a thermodynamic potential of 1.23 V. In practice, kinetic overpotentials for the oxygen evolution reaction (OER) at the photoanode and the hydrogen evolution reaction (HER) at the cathode demand semiconductor bandgaps of at least 1.6–2.0 eV for efficient operation under solar illumination.[137,138]

The process at an n-type semiconductor photoanode proceeds through several sequential steps, each of which must be efficient for the overall device to function. (1) Photon absorption: incident photons with energy $h\nu \geq E_g$ excite electrons from the valence band to the conduction band, creating electron-hole pairs (excitons). The fraction of the solar spectrum absorbed depends on the bandgap and optical absorption coefficient of the material. (2) Charge separation: the built-in electric field at the semiconductor-electrolyte junction separates the photogenerated electrons and holes. The electric field arises from equilibration of the semiconductor Fermi level with the electrolyte redox potential and the resulting band bending in the space charge region. The width of this space charge region, W, depends on the donor density N_D according to:

$$W = \left(\frac{2\varepsilon\varepsilon_0 V_{bi}}{eN_D}\right)^{1/2} \qquad \text{(Eq. 1.7)}$$

where V_{bi} is the built-in potential (difference between the flat-band potential and the applied/equilibrium potential).[15,139] A wider depletion region collects carriers from a greater depth, but excessively low donor densities reduce conductivity. This tension makes donor density optimization through doping a critical design variable. (3) Charge transport: separated electrons migrate through the bulk to the back contact (current collector) while holes migrate to the semiconductor-electrolyte interface. The critical parameter is the minority carrier diffusion length, L_p, which must be comparable to or greater than the optical absorption depth ($1/\alpha$, where α is the absorption coefficient) for efficient carrier collection. For hematite, $\alpha \approx 10^5$ cm^{-1} at visible wavelengths gives an absorption depth of ~100 nm, yet L_p is only 2–4 nm. This constitutes a mismatch of nearly two orders of magnitude that makes recombination the dominant loss pathway.[32,139] (4) Interfacial charge transfer: holes arriving at the surface must oxidize water through the four-electron OER, a kinetically sluggish multi-step reaction that competes with surface recombination. The rate of the OER depends on the density and catalytic activity of surface sites, the concentration of surface-accumulated holes, and the energetic alignment of the valence band edge with the O_2/H_2O redox potential.[138]

These requirements constrain the space of viable photoanode materials. The ideal material possesses a bandgap of 1.8–2.4 eV for maximal solar spectrum utilization, favorable band edge alignment straddling the water redox potentials, high optical absorption coefficient, long minority carrier diffusion length, good bulk conductivity, fast surface reaction kinetics, and stability in aqueous electrolytes under

illumination. No single material satisfies all criteria simultaneously, and the engineering challenge is to identify materials with the best combination of intrinsic properties and then use defect engineering to mitigate the most limiting deficiencies.

1.8 Electrochemical Energy Storage

Several of the MO systems investigated in this dissertation (hematite, BFO, LMO, hydrogen-treated oxides) are evaluated for electrochemical energy storage, and a brief discussion of the relevant charge storage mechanisms provides necessary context. Electrochemical energy storage devices span a continuum from pure capacitors to pure batteries, distinguished by their charge storage mechanisms.[140,141]

Electric double-layer capacitance (EDLC) stores charge electrostatically through reversible adsorption of ions at the electrode-electrolyte interface, with no charge transfer across the interface. The capacitance scales with electrode surface area and the compactness of the Helmholtz double layer but is limited to relatively low energy densities because only the outermost atomic layers participate.[140] Pseudocapacitance involves fast, reversible Faradaic (charge transfer) reactions at or near the electrode surface, including surface redox reactions, intercalation pseudocapacitance, and underpotential deposition. Pseudocapacitive materials like MnO_2, Fe_2O_3, and $BiFeO_3$ exhibit capacitances far exceeding EDLC because Faradaic processes access more charge per unit area, but they degrade faster due to the mechanical and chemical stresses of repeated redox cycling.[140–143] The areal

capacitance C_A of a pseudocapacitive electrode is typically extracted from galvanostatic charge-discharge (GCD) curves according to:

$$C_A = \frac{I\Delta t}{A\Delta V} \quad \text{(Eq. 1.8)}$$

where I is the applied current, Δt is the discharge time, A is the electrode area, and ΔV is the potential window accounting for iR drop.[141,144]

Battery-type charge storage relies on bulk Faradaic reactions that are kinetically limited by solid-state ion diffusion. Either intercalation (reversible insertion/extraction of ions into a host lattice, as in LMO) or conversion (irreversible decomposition of the electrode material into metallic nanoparticles and a lithium compound matrix, as in BFO anodes).[82,83,98,140] Intercalation reactions maintain the host crystal structure and are therefore highly reversible, while conversion reactions offer much higher theoretical capacities (multi-electron processes) but suffer from large volume changes, phase evolution, and poor cyclability. The distinction between pseudocapacitive and battery-type behavior is often assessed by the power-law relationship between peak current i_p and scan rate ν in cyclic voltammetry:

$$i_p = a\nu^b \quad \text{(Eq. 1.9)}$$

where $b = 0.5$ indicates diffusion-limited (battery-type) kinetics and $b = 1.0$ indicates surface-limited (capacitive) kinetics.[141] Many MO electrodes exhibit intermediate b values, reflecting a mixed mechanism.

1.9 Scope and Organization of This Dissertation

This dissertation investigates defect engineering strategies across four metal oxide semiconductor systems. The unifying thesis is that rational manipulation of point defects through heteroatom doping, post-process surface modification, and hydrogen incorporation, can overcome intrinsic limitations that constrain MO performance in energy conversion, energy storage, and electronic applications. Each chapter addresses a specific material system and application space while contributing to the broader understanding of how defects govern metal oxide properties.

Chapter 2 investigates dopant oxide formation in Sn- and Ge-doped hematite (α-Fe_2O_3) and evaluates rapid thermal quenching and post-process alkaline washing as strategies for circumventing or remediating parasitic dopant oxide phases. The critical dopant concentration framework is validated experimentally through EXAFS characterization, and the consequences of non-selective dopant removal for both PEC and energy storage performance are demonstrated.

Chapter 3 develops four wet-chemical synthesis routes for pure and doped bismuth ferrite ($BiFeO_3$) and presents preliminary characterization for PEC, ferroelectric, energy storage, and photon upconversion applications. The xerogel

nanoparticle synthesis is identified as the most versatile route for accommodating both transition metal and lanthanide dopants.

Chapter 4 introduces gallium doping of spinel lithium manganese oxide ($LiMn_2O_4$) for electrochemical lithium extraction from dilute aqueous sources. Structural characterization establishes that Ga^{3+} substitution suppresses Jahn-Teller distortion and increases the Mn^{4+}:Mn^{3+} ratio, and electrochemical testing demonstrates 1000-cycle stability in 50 mM LiCl that substantially exceeds published benchmarks.

Chapter 5 provides a comprehensive review of hydrogen treatment methods for metal oxides, synthesizing evidence across structural, optical, electronic, and magnetic property modifications and identifying key open questions regarding mechanism, stability, and scalability.

Together, these studies demonstrate that defect engineering remains a fertile and essential approach for advancing metal oxide technology, and that the specific challenges of dopant solubility, phase purity, structural stability, and hydrogen incorporation each demand tailored strategies informed by the unique crystal chemistry and target application of the material system.

1.10 References

1. Lany, S. *J. Phys.: Condens. Matter* **2015**, *27* (28), 283203.
2. Comini, E.; Baratto, C.; et al. *Progress in Materials Science* **2009**, *54* (1), 1–67.
3. Kofstad, P. *Oxid Met* **1995**, *44* (1), 3–27.
4. Deml, A. M.; Holder, A. M.; et al. *J. Phys. Chem. Lett.* **2015**, *6* (10), 1948–1953.
5. Smart, T. J.; Chen, M.; et al. *J. Appl. Phys.* **2021**, *130* (24), 245705.
6. Smart, T. J.; Baltazar, V. U.; et al. *Chem. Mater.* **2021**, *33* (12), 4390–4398.
7. Berglund, S. P.; Rettie, A. J. E.; et al. *Phys. Chem. Chem. Phys.* **2012**, *14* (19), 7065.
8. Smart, T. J.; Ping, Y. *J. Phys.: Condens. Matter* **2017**, *29* (39), 394006.
9. Dai, Z.; Qin, F.; et al. *ACS Catal.* **2016**, *6* (5), 3180–3192.
10. Cushing, Scott. K.; Meng, F.; et al. *ACS Catal.* **2017**, *7* (3), 1742–1748.
11. Li, M.; Yang, Y.; et al. *Nano Lett.* **2017**, *17* (4), 2490–2495.
12. Das, R.; Shelake, A. R.; et al. *Ionics* **2025**, *31* (10), 11115–11127.
13. Yang, C.-H.; Kan, D.; et al. *Phys. Chem. Chem. Phys.* **2012**, *14* (46), 15953–15962.
14. Zhao, L.; Xiao, J.; et al. *International Journal of Hydrogen Energy* **2018**, *43* (28), 12646–12652.
15. Park, J.; Kang, J.; et al. *Journal of Materials Chemistry A* **2023**, *11* (45), 24551–24565.

16. Deleuze, P.-M.; Magnan, H.; et al. *J. Phys. Chem. Lett.* **2021**, *12* (47), 11520–11527.
17. Liu, J.; Liang, C.; et al. *Chem. Commun.* **2011**, *47* (28), 8040–8042.
18. Zhao, Y.; Niu, Z.; et al. *Electrochem. Energy Rev.* **2023**, *6* (1), 14.
19. Pesci, F. M.; Wang, G.; et al. *J. Phys. Chem. C* **2013**, *117* (48), 25837–25844.
20. Irshad, I.; Nazir, A.; et al. *Journal of Energy Storage* **2025**, *107*, 114987.
21. Aalim, M.; Irshad, I.; et al. *J Mater Sci: Mater Electron* **2023**, *34* (18), 1409.
22. Shen, S.; Kronawitter, C. X.; et al. *J. Mater. Chem. A* **2013**, *1* (46), 14498–14506.
23. Yin, R.; Xu, W.; et al. *Desalination* **2026**, *620*, 119647.
24. Tian, G.; Gao, J.; et al. *Electrochimica Acta* **2024**, *475*, 143361.
25. Yamada, A.; Tanaka, M.; et al. *Journal of Power Sources* **1999**, *81–82*, 73–78.
26. Mukai, K.; Andreica, D.; et al. *J. Appl. Phys.* **2013**, *113* (5), 053904.
27. de Lima, F. C.; Schleder, G. R.; et al. *Appl. Phys. Lett.* **2021**, *118* (20), 201602.
28. Zhang, Z.; Tsuchimochi, T.; et al. *Nat Commun* **2022**, *13* (1), 1499.
29. Smart, T. J.; Baltazar, V. U.; et al. *Chem. Mater.* **2021**, *33* (12), 4390–4398.
30. Mayford, K.; McNair, S.; et al. *Phys. Rev. Mater.* **2025**, *9* (9), 095802.
31. Yoon, K.-Y.; Park, J.; et al. *Nat Commun* **2021**, *12* (1), 4309.
32. Wang, G.; Wang, H.; et al. *Nano Lett.* **2011**, *11* (7), 3026–3033.
33. Yang, Y.; Forster, M.; et al. *Angewandte Chemie International Edition* **2016**, *55* (10), 3403–3407.
34. Nasejje, S.; Mukhokosi, E. P.; et al. *Discov Mater* **2024**, *4* (1), 44.

35. Tamirat, A. G.; Rick, J.; et al. *Nanoscale Horiz.* **2016**, *1* (4), 243–267.

36. Chen, Q.; Chong, Y.; et al. *Processes* **2021**, *9* (7), 1102.

37. Pan, Q.; Yang, C.; et al. *Electrochimica Acta* **2021**, *393*, 139079.

38. Peng, S.; Yu, L.; et al. *Nanotechnology* **2016**, *27* (50), 505404.

39. Ramadan, A.; Ramadan, W. *Journal of Energy Storage* **2024**, *100*, 113702.

40. Cooper, J. K.; Ling, Y.; et al. *J. Phys. Chem. C* **2012**, *116* (33), 17360–17368.

41. Yan, X.; Wang, C.; et al. *Chemical Engineering Journal* **2025**, *507*, 160395.

42. Ai, M.; Li, X.; et al. *Chemical Engineering Science* **2022**, *250*, 117397.

43. Nithya, V. D.; Arul, N. S. *Journal of Power Sources* **2016**, *327*, 297–318.

44. Kumar Jha, B.; Chaule, S.; et al. *Materials Chemistry Frontiers* **2024**, *8* (10), 2197–2226.

45. Ma, H.; Chen, W.; et al. *Journal of Colloid and Interface Science* **2022**, *625*, 585–595.

46. Ma, H.; A. Mahadik, M.; et al. *Nanoscale* **2018**, *10* (47), 22560–22571.

47. Rodríguez-Gutiérrez, I.; Mouriño, B.; et al. *ECS J. Solid State Sci. Technol.* **2022**, *11* (4), 043001.

48. Li, M.; Yang, Y.; et al. *Nano Lett.* **2017**, *17* (4), 2490–2495.

49. Zhou, Z.; Huo, P.; et al. *J. Phys. Chem. C* **2015**, *119* (47), 26303–26310.

50. Priya, A. S.; Henry, J.; et al. *Ceramics International* **2025**, *51* (20, Part A), 29877–29908.

51. Gebhardt, J.; Rappe, A. M. *Phys. Rev. B* **2018**, *98* (12), 125202.

52. Palewicz, A.; Przeniosło, R.; et al. *Acta Cryst B* **2007**, *63* (4), 537–544.

53. Doig, K. I.; Aguesse, F.; et al. *Phys. Rev. B* **2013**, *88* (9), 094425.

54. Hill, N. A. *J. Phys. Chem. B* **2000**, *104* (29), 6694–6709.

55. Jiang, Z.-Z.; Guan, Z.; et al. *Materials Characterization* **2017**, *131*, 217–223.

56. Spaldin, N. A.; Fiebig, M. *Science* **2005**, *309* (5733), 391–392.

57. Catalan, G.; Scott, J. F. *Advanced Materials* **2009**, *21* (24), 2463–2485.

58. Calzada, M. L.; Bretos, I.; et al. *ACS Appl. Energy Mater.* **2025**, *8* (5), 2845–2868.

59. Das, R.; Mandal, K. *Journal of Magnetism and Magnetic Materials* **2012**, *324* (11), 1913–1918.

60. Liu, Y.; Wang, Y.; et al. *Progress in Materials Science* **2022**, *127*, 100943.

61. Dong, S.; Xiang, H.; et al. *Natl Sci Rev* **2019**, *6* (4), 629–641.

62. Chu, Y.-H.; Martin, L. W.; et al. *Materials Today* **2007**, *10* (10), 16–23.

63. Shalf, J. *Philos Trans A Math Phys Eng Sci* **2020**, *378* (2166), 20190061.

64. Etiemble, D. arXiv:2206.03201v1 [cs.ET].

65. Mocherla, P. S. V.; Karthik, C.; et al. *Appl. Phys. Lett.* **2013**, *103* (2), 022910.

66. Benyoussef, M.; Saitzek, S.; et al. *Catalysts* **2022**, *12* (2), 215.

67. Xu, H.-M.; Wang, H.; et al. *Nanomaterials* **2016**, *6* (11), 215.

68. Song, J.; Kim, T. L.; et al. *Nano Res.* **2018**, *11* (2), 642–655.

69. Lee, H.; Kim, H.-S.; et al. *J. Mater. Chem. A* **2020**, *8* (20), 10377–10385.

70. Wang, M.; Wei, H.; et al. *Physics Letters A* **2020**, *384* (32), 126831.

71. Richards, B. S.; Hudry, D.; et al. *Chem. Rev.* **2021**, *121* (15), 9165–9195.

72. Zhang, J.; Huang, Y.; et al. *ACS Appl. Mater. Interfaces* **2017**, *9* (9), 8142–8150.

73. Han, S.; Deng, R.; et al. *Angewandte Chemie International Edition* **2014**, *53* (44), 11702–11715.

74. Ende, B. M. van der; Aarts, L.; et al. *Phys. Chem. Chem. Phys.* **2009**, *11* (47), 11081–11095.

75. Wu, Y.; Chan, S. Y.; et al. *Chemistry – An Asian Journal* **2021**, *16* (18), 2596–2609.

76. Chen, G.; Qiu, H.; et al. *Chem. Rev.* **2014**, *114* (10), 5161–5214.

77. Bünzli, J.-C. G.; Piguet, C. *Chem. Soc. Rev.* **2005**, *34* (12), 1048–1077.

78. Feng, B.; Xue, H.; et al. *Chin. Sci. Bull.* **2010**, *55* (4), 452–456.

79. Nayak, A. K.; Gopalakrishnan, T. *ACS Appl. Nano Mater.* **2022**, *5* (10), 14663–14676.

80. Nayak, S.; Soam, A.; et al. *J Mater Sci: Mater Electron* **2018**, *29* (11), 9361–9368.

81. Geelani, K. A.; Alotaibi, B. M.; et al. *Journal of Energy Storage* **2024**, *85*, 111054.

82. Oli, N.; Flórez Gómez, J. F.; et al. *ACS Appl. Energy Mater.* **2023**, *6* (21), 10853–10861.

83. Li, J.; Hwang, S.; et al. *Nat Commun* **2019**, *10* (1), 2224.

84. Mohan, M.; Shetti, N. P.; et al. *Journal of Power Sources* **2023**, *574*, 233166.

85. Sagar, E.; Mahesh, R.; et al. *Journal of Physics and Chemistry of Solids* **2017**, *110*, 316–326.

86. Jha, S. K.; Priyadarshi, P. K. *International Journal of Engineering and Science Invention* **2024**, *13* (10), 40–44.

87. Béa, H.; Bibes, M.; et al. *Appl. Phys. Lett.* **2005**, *87* (7), 072508.

88. Acharya, M.; Joshi, C. R.; et al. *Chem. Mater.* **2024**, *36* (16), 7633–7646.

89. Brown, C.; Harris-Lee, T. R.; et al. *European Journal of Inorganic Chemistry* **2025**, *28* (25), e202500333.

90. Ihlefeld, J. F.; Tian, W.; et al. *IEEE Transactions on Ultrasonics, Ferroelectrics, and Frequency Control* **2009**, *56* (8), 1528–1533.

91. *Batteries and Secure Energy Transitions – Analysis*. IEA.

92. *Building new advantages for batteries by 2035 | McKinsey*.

93. *Executive summary – Global Critical Minerals Outlook 2025 – Analysis*. IEA.

94. Nilges, B.; Reinert, C.; et al. *Journal of Cleaner Production* **2024**, *434*, 140062.

95. Cai, B.; Feng, K.; et al. *Resources, Conservation and Recycling* **2024**, *205*, 107570.

96. Flexer, V.; Baspineiro, C. F.; et al. *Science of The Total Environment* **2018**, *639*, 1188–1204.

97. Dessemond, C.; Lajoie-Leroux, F.; et al. *Minerals* **2019**, *9* (6), 334.

98. Pasta, M.; Battistel, A.; et al. *Energy Environ. Sci.* **2012**, *5* (11), 9487–9491.

99. Kim, J.-S.; Lee, Y.-H.; et al. *Environ. Sci. Technol.* **2015**, *49* (16), 9415–9422.

100. Lee, J.; Yu, S.-H.; et al. *Phys. Chem. Chem. Phys.* **2013**, *15* (20), 7690–7695.

101. Liu, C.; Li, Y.; et al. *Joule* **2020**, *4* (7), 1459–1469.

102. Kong, L.; Yan, G.; et al. *Nat Commun* **2025**, *16* (1), 806.

103. Kanoh, H.; Feng, Q.; et al. *J. Electrochem. Soc.* **1995**, *142* (3), 702.

104. Xu, S.; Song, J.; et al. *Journal of Membrane Science* **2021**, *635*, 119441.

105. Zhou, G.; Sun, X.; et al. *J. Phys. Chem. Lett.* **2020**, *11* (8), 3051–3057.

106. Gonzalez-Rosillo, J. C.; Guc, M.; et al. *Chem. Mater.* **2024**, *36* (12), 6144–6153.

107. Tesfamhret, Y.; Liu, H.; et al. *ChemElectroChem* **2021**, *8* (8), 1516–1523.

108. Sun, X.; Xiao, R.; et al. *Langmuir* **2021**, *37* (17), 5252–5259.

109. Murphy, O.; Haji, M. N. *Front. Chem. Eng.* **2022**, *4*.

110. Xue, N.; Wu, X.; et al. *ACS Nano* **2024**, *18* (49), 33743–33753.

111. Tan, G.; Wan, S.; et al. *Advanced Materials* **2024**, *36* (14), 2310657.

112. Wu, Y.; Shi, P.; et al. *Energy Fuels* **2023**, *37* (5), 4083–4093.

113. Li, X.; Xu, Y.; et al. *Journal of Alloys and Compounds* **2009**, *479* (1), 310–313.

114. Liao, G.; Yu, L.; et al. *Water Research* **2025**, *274*, 123131.

115. Fan, W.; Ma, L.; et al. *Desalination* **2025**, *615*, 119260.

116. Fang, D.; Zhang, X.; et al. *Chemical Engineering Journal* **2025**, *521*, 166161.

117. Battistel, A.; Palagonia, M. S.; et al. *Advanced Materials* **2020**, *32* (23), 1905440.

118. Michalsky, R.; Botu, V.; et al. *Adv Energy Mater* **2015**, *5* (7), 1401082.

119. Hayashi, E.; Yamaguchi, Y.; et al. *J. Am. Chem. Soc.* **2019**, *141* (2), 890–900.

120. Belousov, V. M.; Vasylyev, M. A.; et al. *Chemical Engineering Journal* **2003**, *91* (2), 143–150.

121. Rex, R. E.; Yang, Y.; et al. *J. Phys. Chem. C* **2016**, *120* (6), 3530–3541.

122. Lee, B.-M.; Lee, B.-J. *Metall Mater Trans A* **2014**, *45* (6), 2906–2915.

123. Shi, G. A.; Saboktakin, M.; et al. *Applied Physics Letters* **2004**, *85* (23), 5601–5603.

124. Wang, Z.; Wang, X.; et al. *J. Phys. Chem. Lett.* **2020**, *11* (3), 1075–1080.

125. Zhu, Q.; Jiang, S.; et al. *Advanced Materials* **2020**, *32* (50), 2004059.

126. Zhou, X.; Yao, X.; et al. *Advanced Science* **2026**, *13* (1), e10771.

127. Cheng, H.; Wen, M.; et al. *J. Am. Chem. Soc.* **2016**, *138* (29), 9316–9324.

128. Li, B.; Xie, L.; et al. *Angewandte Chemie International Edition* **2019**, *58* (39), 13711–13716.

129. Hong, W.-K.; Park, J. B.; et al. *Nano Lett.* **2013**, *13* (4), 1822–1828.

130. Chen, X.; Liu, L.; et al. *Science* **2011**, *331* (6018), 746–750.

131. Kim, K.; Kim, M.-S.; et al. *Chem. Mater.* **2016**, *28* (5), 1453–1461.

132. Xie, L.; Zhu, Q.; et al. *J. Am. Chem. Soc.* **2020**, *142* (9), 4136–4140.

133. Huang, W.; Chien, P.-H.; et al. *Proceedings of the National Academy of Sciences* **2020**, *117* (31), 18231–18239.

134. Koida, T.; Fujiwara, H.; et al. *Jpn. J. Appl. Phys.* **2007**, *46* (7L), L685.

135. Tang, H.; Ishikawa, K.; et al. *Journal of Applied Physics* **2015**, *118* (20), 205703.

136. Hossein-Babaei, F.; Alizadeh, A. *J Mater Sci: Mater Electron* **2024**, *35* (20), 1420.

137. Liu, H.; Fan, X.; et al. *Journal of Environmental Chemical Engineering* **2023**, *11* (1), 109224.

138. Grätzel, M. *Nature* **2001**, *414* (6861), 338–344.

139. Xiao, J.; Huang, H.; et al. *Journal of Catalysis* **2017**, *350*, 48–55.

140. Poonam; Sharma, K.; et al. *Journal of Energy Storage* **2019**, *21*, 801–825.

141. Olabi, A. G.; Abbas, Q.; et al. *Energy* **2022**, *248*, 123617.

142. Yan, Y.; Tang, H.; et al. *Energies* **2017**, *10* (9), 1296.

143. Shivakumara, S.; Penki, T. R.; et al. *Materials Letters* **2014**, *131*, 100–103.

144. Li, B.; Sun, Q.; et al. *Nanomaterials* **2018**, *8* (1), 41.

Chapter 2

Circumventing Dopant Oxide Formation in α-Fe_2O_3 Through Synthesis and Post-Process Modification

2.1 Abstract

α-Fe_2O_3 (hematite) is a moderate band gap metal oxide semiconductor with a strong history of photoelectrochemical, photocatalytic, and energy storage applications. Several landmark studies established heteroatom doping as a simple and effective way to modulate the optoelectronic properties of the material. However, successful doping is highly dependent on synthesis conditions, particularly the temperature and O_2 partial pressure during annealing. Computational and experimental work has shown that dopant precipitation to native oxide occurs above a critical dopant saturation point. In addition to temperature and pressure, this point is dependent on the identity of the dopant element. Often, these native dopant oxide secondary phases interfere with several important properties of the bulk material such as optical absorption, conductivity, and charge separation, and can be considered a parasitic phase. It is therefore important to study the formation conditions of these dopant oxides, and develop strategies to increase dopant solubility in hematite, or otherwise remove the dopant oxide in a post-process wash. Herein, two main methods of circumventing dopant oxide formation are implemented and discussed. A rapid cooling protocol is employed to thermally quench the powder in order lock the dopants within the hematite crystal and avoid diffusion and precipitation during

cooling. Both Sn and Ge dopant are studied using a variety of X-ray and electrochemical characterization techniques, to reveal that there is no appreciable reduction in the formation of dopant oxide with the developed rapid cooling procedure. The same dopants were also studied using a post-process alkaline washing protocol to see if the removal of dopant oxide may improve doped hematite's photoelectrochemical or energy storage performance. In both dopant cases and across different etching procedures, no major changes to the dopant concentrations were observed.

2.2 Introduction

The growing need to develop sustainable, carbon-neutral energy technologies has driven intense research into photoelectrochemical (PEC) water splitting to convert solar energy directly into chemical fuel in the form of hydrogen (Figure 2.1a).[1–4] Among the many semiconductor photoanode candidates investigated for this purpose, hematite (α-Fe_2O_3) has attracted exceptional and enduring interest. Hematite possesses several advantageous properties, including abundant availability in nature, eco-friendliness, high photochemical stability, a narrow bandgap of 1.9 – 2.2 eV (Figure 2.1b) enabling broad visible light absorption, and the ability to achieve a theoretical maximum solar-to-hydrogen efficiency of nearly 15%.[5–10] Beyond PEC water splitting, hematite has also emerged as a worthy candidate for electrochemical energy storage due to its non-toxicity, high ideal theoretical capacitance (3625 F g^{-1}), and abundant reserves.[11–16]

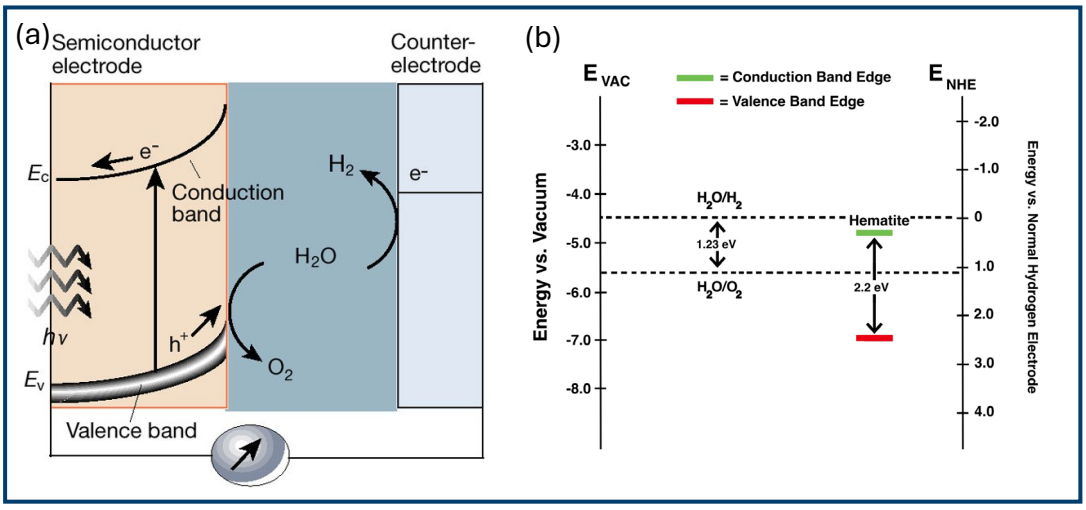

Figure 2.1 (a) Schematic diagram of photoelectrochemical water splitting cell. The left side represents a photoanode where water oxidation (oxygen evolution reaction) takes place. Reproduced with permission from ref. ([1]). Copyright 2001 Nature. (b) The band gap of hematite compared to the redox potential of water splitting. The energy scale is in eV and compared to the normal hydrogen electrode and the vacuum level. The lower edge of the conduction band (green) and upper edge of the valence band (red) are presented along with the band gap in eV.

Despite this, the practical performance of hematite in both applications falls well short of theoretical figures. Several intrinsic factors limit hematite's water oxidation activity, including poor electrical conductivity, high charge recombination rates, slow charge transfer kinetics at the electrolyte interface, low oxygen evolution reaction kinetics, and short hole diffusion length.[17,18] The hole diffusion length is particularly constraining, being only 2 – 4 nm, making recombination a severe

limiting factor in charge transport.[17,19] Similarly in the supercapacitor context, the low conductivity of α-Fe_2O_3 (~10^{-14} S cm^{-1}) severely limits its actual capacitance (120–320 F g^{-1}), which is far below the theoretical value.[20,21] These shared limitations, which are fundamentally rooted in poor electronic conductivity and high carrier recombination, motivate a common solution: extrinsic doping.

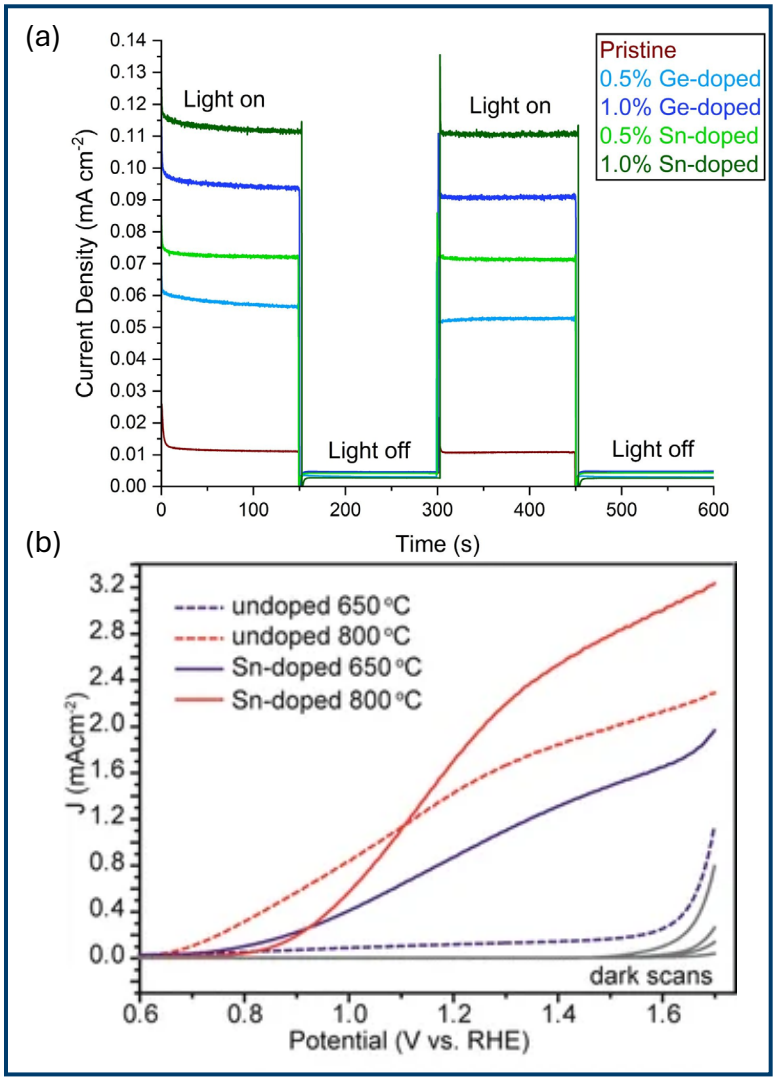

Figure 2.2 (a) Chronoamperometric plot of pristine and Ge and Sn doped hematite with chopped illumination. Collected in a quartz, 3 chamber photoelectrochemical

cell with 1 M NaOH electrolyte and Ag/AgCl (sat. KCl) reference, carbon rod counter, and hematite working electrodes. Potential held at 1.6 V vs. RHE. (b) Linear sweep voltammogram of pristine and Sn doped hematite nanowires. Reproduced with permission from ref. ([22]). Copyright 2011 American Chemical Society.

Elemental doping is among the most widely investigated strategies to address hematite's intrinsic deficiencies (Table 2.1). Incorporation of tetravalent cations such as Ti^{4+}[23–25], Sn^{4+}[9,26,27], Si^{4+}[28,29], and Ge^{4+}[30–32] as n-type dopants increases the donor density and improves electron mobility, enhancing both bulk charge transport and surface charge transfer kinetics.[33] Elemental doping and/or creating oxygen vacancies are effective approaches to improve hematite's conductivity by enhancing the charge carrier density and therefore energy conversion or storage performance (Figure 2.2).[6,19,32]

Among these dopants, tin has been particularly ubiquitous in the literature, partly by design and partly by accident. High-temperature annealing has been widely applied to enhance crystallinity, improve the hematite–substrate interface, and introduce tin dopants from the fluorine-doped tin oxide (FTO) substrate.[34] This unintentional self-doping from the FTO substrate in which Sn^{4+} ions diffuse into the hematite lattice during the requisite high-temperature sintering step has been extensively documented.[9,35] Many report that mesoporous hematite showed improved PEC performance after 800 °C annealing, attributing the enhancement to Sn diffusion from the FTO substrate.[36,37]

Table 2.1 Compilation of recent works studying various hematite dopants for photoelectrochemical water splitting. Reproduced from ref. ([38]).

Dopant	Photocurrent density (mA cm^{-2})	Potential *vs.* RHE	Electrolyte	Carrier density (10^{20} cm^{-3})
Ti	1.25	1.23	1 M NaOH	—
Ti	0.92	1.23	1 M KOH	—
P	2.70	1.23	1 M NaOH	1.01
P	1.48	1.23	1 M KOH	5.80
P/Ti	2.50	1.23	1 M NaOH	3.48
P/Ru	4.55	1.23	1 M KOH	—
Si	2.20	1.23	1 M NaOH	—
Si/Ti	2.44	1.23	1 M NaOH	—
Si/Ti	2.36	1.23	1 M NaOH	—
Si/Ti	3.00	1.23	1 M NaOH	1.52
Sn	0.56	1.23	1 M NaOH	—
Sn	1.24	1.23	1 M NaOH	0.538
Sn	0.98	1.23	1 M NaOH	—
Sn	1.38	1.23	1 M KOH	—
Sn/Be	1.70	1.23	1 M NaOH	0.803
Sn/Si	3.00	1.23	1 M NaOH	2.90

Ge	1.40	1.23	1 M NaOH	0.302
Ge	3.50	1.23	1 M NaOH	3.10
B	~0.1	1.23	1 M NaOH	—
B/Ti	1.92	1.23	1 M NaOH	8.50
Mg	~0.5	1.23	1 M KOH	—
Mg	0.763	1.23	1 M NaOH	41.1
Mg/P	2.4	1.23	1 M NaOH	2.97
Al	~0	1.23	1 M NaOH	0.02
Al/Ti	1.30	1.23	1 M NaOH	1.70
Zr	1.50	1.23	1 M KOH	5.88
Ta	1.93	1.23	1 M NaOH	—
Ta/Sn	2.37	1.23	1 M NaOH	—
Pt	2.19	1.23	1 M NaOH	0.0277
Pt	2.71	1.23	1 M KOH	
Nb	0.63	1.00	0.5 M Na_2SO_4	9.42
Nb/Sn	1.88	1.23	1 M KOH	0.321
Gd	~1.5	1.23	1 M KOH	0.0217

Germanium has emerged as a particularly promising alternative n-type dopant. Ge can dramatically enhance donor density while maintaining the crystallinity of hematite, and exhibits outstanding solubility in the hematite lattice.[30,31] DFT calculations have shown that Ge is more soluble in hematite than Si and Sn due to a

favorable balance of atomic size and electronic factors.[39–41] The advantages of Ge as a dopant include its feasible atomic radius and the low formation enthalpy of the secondary phase GeO_2.[34,38] These properties, combined with its ability to suppress unintentional Sn co-doping from FTO substrates, have made Ge-doped hematite a subject of increasing study.[34]

Nevertheless, a critical and often underappreciated complication in the doping of hematite is the thermodynamic tendency of dopant cations to segregate toward the surface or precipitate entirely during high-temperature processing. In ionic oxide systems, aliovalent dopants are driven by elastic and electrostatic interactions to migrate from the bulk to grain boundaries and external surfaces, where they can accumulate as oxide overlayers (Figure 2.3). In many cases, only small amounts of dopants segregate due to the poor driving force for ion migration and/or the presence of substantial grain boundaries that confine dopants within a nanoscale region.[42] Previous work in this group has demonstrated that while perhaps minimal, it can have a significant effect on the performance of hematite.[43]

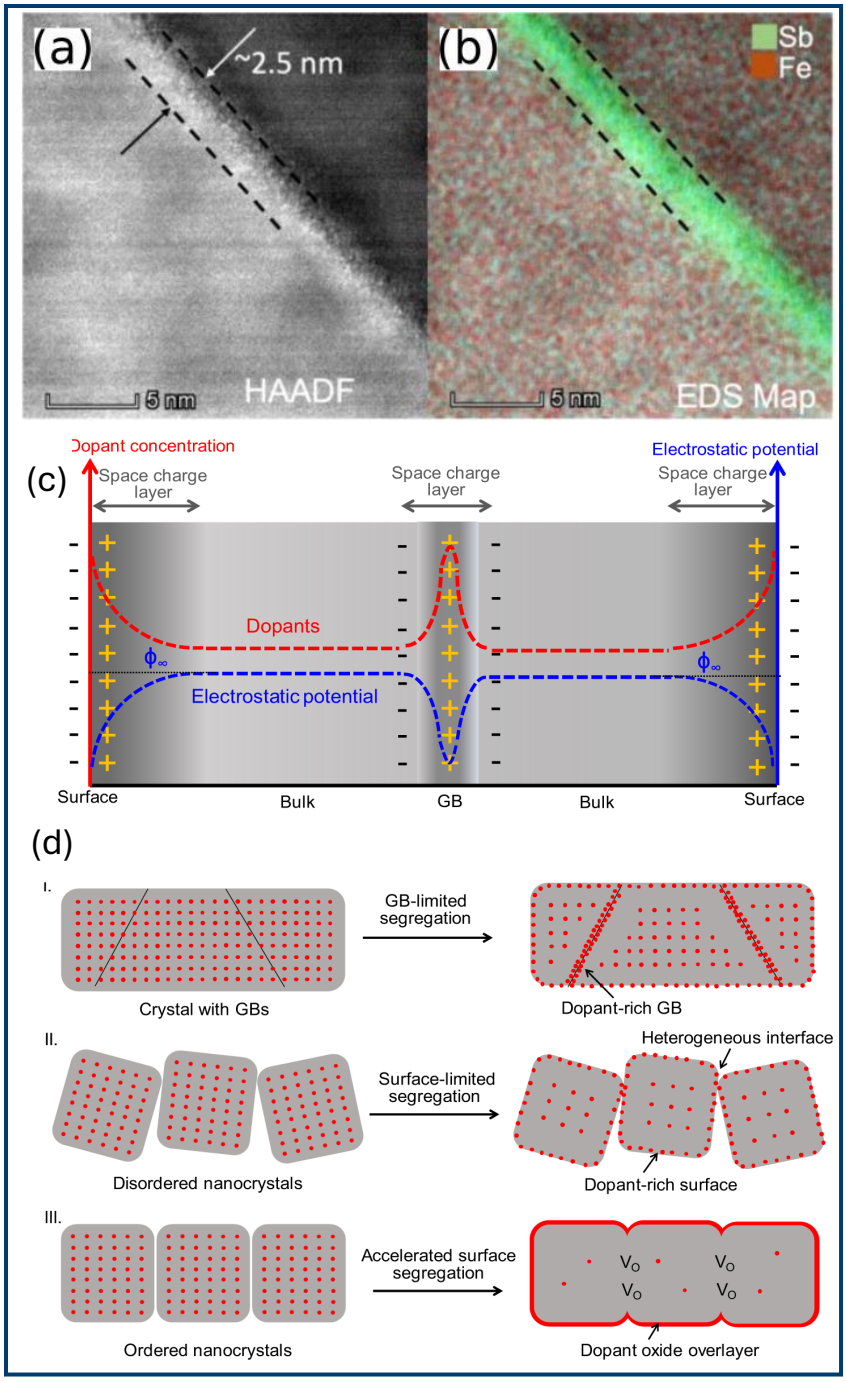

Figure 2.3 (a,b) HAADF-STEM/EDS elemental mapping of Sb doped hematite. Sb in green clearly segregated to the grain boundary. Reproduced with permission from ref. ([44]). Copyright 2021 American Institute of Physics. (c) Distribution of dopants

and electrostatic potential (donor-doping case) in ionic oxides based on the space charge theory. (d) Schematic illustration of the dopant segregation in different types of ionic oxide crystals: (I) Crystal with numerous grain boundaries: dopants tend to segregate at the surface and grain boundaries. (II) Disordered nanocrystals: a small number of dopants tend to segregate on the surface due to the lack of driving force even at high temperatures. (III) Ordered nanocrystals with highly aligned interfaces: a large number of dopants segregate on the outer surface because of interface sintering (grain boundary elimination), creating numerous interfacial V_O and narrowing the space charge layer to drive the charge migration. Reproduced with permission from ref. ([42]). Copyright 2022 Nature Communications

This surface segregation of dopants into their secondary oxide phases like SnO_2, GeO_2, TiO_2, etc. sometimes manifests paradoxically. On one hand, some degree of segregated oxide overlayer has been observed to be beneficial in certain configurations: hematite mesocrystals with thin rutile TiO_2 overlayers exhibit excellent PEC water oxidation performance owing to suppressed surface recombination of photogenerated electrons and holes.[42,45] On the other hand, uncontrolled dopant oxide accumulation at the hematite surface can block active sites for the oxygen evolution reaction, introduce additional surface recombination centers, impede hole transfer to the electrolyte, and interfere with optical absorption. Metal ions such as Sn^{4+} and Ti^{4+} that segregate to the hematite surface can simultaneously act as electron–hole pair recombination sites,[46] creating a fundamental tension

between the beneficial bulk doping effect and the detrimental surface oxide formation.

The interaction between intentional dopants and inadvertent Sn from FTO substrates adds a further layer of complexity. When Ge and Sn dopants are co-present, the crystallinity of hematite can significantly deteriorate due to structural distortion, and the interaction between unintentional tin and intentional dopant remains poorly understood. Resolving this complexity by ensuring that dopants such as Sn and Ge reside substitutionally within the hematite lattice rather than precipitating as surface oxide phases is therefore central to unlocking the true potential of doped hematite photoanodes and supercapacitor electrodes.

Several processing strategies have been explored to control dopant distribution and minimize surface oxide formation. Rapid thermal processing one way proposed to kinetically trap dopant atoms within the hematite lattice before surface segregation equilibria can be established.[47] Related work has demonstrated that a post-rapid thermal process can enhance PEC performance by introducing oxygen vacancy defects alongside Sn doping, with transfer efficiency increasing from 13 to 87% through co-doping by Sn and oxygen vacancies.[35] However, the exact chemical environment about Sn is not fully characterized.

Post-synthetic surface treatments represent a complementary approach. Chemical etching, both acidic and alkaline, has been employed to selectively remove surface-passivating overlayers or modify surface state densities. Zou et al. reported a

surface corrosion method in acid solution to reduce the overpotential of Ti^{4+}-doped hematite by suppressing the back reaction,[48] while Li et al. reported an acid treatment method to improve the photocurrent density by suppressing electron–hole recombination in Sn^{4+}-doped hematite.[49] The selectivity of alkaline solutions for etching amphoteric or soluble metal oxides such as SnO_2, GeO_2, and more complicated dopant oxides, over the comparatively inert α-Fe_2O_3 surface offers an attractive route for the targeted removal of unwanted dopant oxide in a post-process washing step.

The work presented in this chapter directly addresses the detrimental formation of dopant oxide surface phases in Sn- and Ge-doped hematite. Two distinct strategies are developed and evaluated: (i) circumvention of dopant oxide formation through optimized rapid cooling procedures that kinetically suppress dopant precipitation during high-temperature annealing, and (ii) post-process remediation via alkaline etching to selectively dissolve and remove dopant oxide from the hematite. The impact of these approaches on PEC water splitting performance and electrochemical charge storage is systematically evaluated, demonstrating that control over the dopant's spatial distribution, lattice-incorporated versus dopant oxide, is a decisive parameter governing device performance in both applications.

2.3 Experimental

2.3.1 General Hematite Nanowire Synthesis

Hydrothermal Preparation of β-FeOOH Precursor

Previous work in our lab prepared hematite nanowire powder samples via a hydrothermal formation of Fe precursor followed by high temperature annealing in air to convert to α-Fe_2O_3. A 0.15 M $FeCl_3 \bullet 6H_2O$ and 1 M $NaNO_3$ solution was prepared in a beaker with stirring. The solution was adjusted to pH = 1.5 dropwise with concentrated HCl which was accompanied by a slight color change from dark yellow/orange to a bright yellow solution. Then, 33 mL of the solution was transferred to a Teflon-lined 50 mL autoclave and heated at 95 ˚C for 4 h. The nanowires could be grown directly on conductive substrates like carbon paper or fluorine tin oxide (FTO) glass, or as a loose powder. In direct growth samples, the conductive substrate was placed at an angle in the autoclave. The autoclave was allowed to cool, and the resulting powder or film was washed twice with isopropyl alcohol and thrice with deionized water before drying in a 60 ˚C for 24 h. The dried β-FeOOH sample with an ochre color served as the solid-state precursor for pristine and doped hematite in the subsequent annealing step.

In the case of doped samples, some amount of β-FeOOH (or α-Fe_2O_3 in the case of some rapid cooling samples),was weighed out (or mass loading on substrate was determined by difference in the case of hydrothermally grown samples) and a stoichiometric amount of dopant precursor solution was added to the powder or to the surface of the film. Precursor solutions were $SnCl_4$ and $GeCl_4$ in ethanol and concentration was adjusted so that the amount added to the β-FeOOH powder never exceeded 1 mL. Then, a complementary volume of ethanol was added to the mixture so that the total volume of dopant precursor solution + pure ethanol added to the

sample was 1 mL. The powder slurry was then sonicated for 10 min before drying in a 60 ˚C oven for 1 h to evaporate ethanol solvent. Substrate deposited samples were allowed to air dry for some time before being placed in a 60 ˚C oven for 1 h. The resulting dried samples were then annealed according to the above procedure. Pristine samples were used as is without the addition of dopant precursor solution.

High Temperature Annealing

Exact amounts vary, but generally, a small amount (~50 mg) β-FeOOH powder was weighed out and placed in an alumina crucible. Substrate deposited samples were taken as is. For pristine (undoped) hematite, the sample was then annealed in open air in a tube furnace (model) at 550 ˚C for 30 min then ramped to another higher temperature for another 30 min. Prototypical samples were annealed at 800 ˚C during the second part of the heating profile but other temperatures (900, 1000, 1100 ˚C) were also tested. The ramp rate during heating was 20 ˚C min^{-1}. In the case of carbon paper sample, annealing temperature was kept to 300 ˚C to avoid burning the carbon entirely.

2.3.2 Rapid Cooling Synthesis

Due to the anatomy of the tube furnace, extreme temperatures involved, and open nature of the alumina crucible, a sufficiently rapid cooling protocol was not possible. Therefore, a new heating device and rapid cooling apparatus was constructed. The device consisted of a vertical handheld induction heating coil, 316 stainless steel Swagelok heating element, and a sample suspension system using a

stripped alligator clip (Figure 2.4). The entire apparatus was suspended approximately 3 in above an insulated glass beaker filled with ice water. The powder samples prepared as described above were loaded into the bottom of a 0.5 x 5 cm 316 stainless steel cylindrical tube with one sealed end. During loading the powder, a thin glass pipette was placed in the center so that when removed, there was a channel down the center of the powder column. This is essential to allow sufficient access to air for complete conversion of the precursor. The tub was carefully clipped to the heating element and a glass pipette attached to a hose was placed to deliver compressed air at a rate of 40 mL min^{-1} into the tube during heating. The induction heater was then turned on for 5 min, and the temperature was monitored with an infrared thermometer gun. Precise temperature control was difficult because of the sensitivity of the induction heating method, but generally samples heated to 820 - 850 ˚C over 2 minutes then held at this temperature for 3 min. The sample was then unclipped from the heating element where the tube was allowed to fall through the open heating element into the ice bath below.

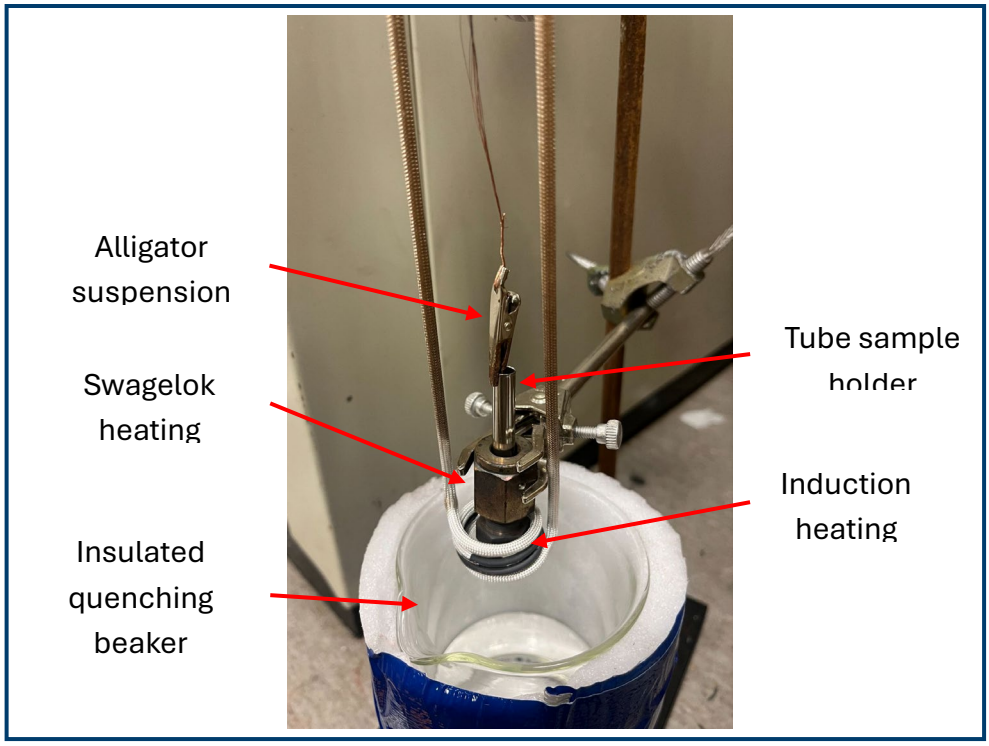

Figure 2.4 Close-up photo of the rapid cooling apparatus. Not pictured: glass pipette air flow delivery, and incandescence during operation.

2.3.3 Post-Process Washing

Both powder and substrate deposited samples could be treated with the same procedure but placing the sample in a Teflon-lined autoclave with 5 M NaOH and heated at 120 ˚C for 24 h. Hematite is very stable in alkaline environments even at elevated temperature while SnO_2 and GeO_2 are expected to be slightly soluble in alkaline environments and more so at high temperature allowed by the autoclave. Once cooled, the samples was washed thoroughly with deionized water and dried in a 60 ˚C oven for 24 h before characterization and testing.

2.3.4 Characterization

Powder X-Ray Diffraction (XRD)

Thin film and powder samples were analyzed using a Rigaku SmartLab high-resolution powder X-ray diffractometer with a Cu K_α X-ray source in parallel beam mode. Substrate deposited samples were placed on the flat sample plate, and the Z-axis was adjusted based on the substrate thickness (2.2 mm FTO glass. 0.4 mm carbon paper). Powder samples were finely ground with a mortar and pestle and spread in a depressed glass slide samples holder. Scans were run at various 2θ angles ranges with 0.02˚ steps at a rate of 1˚ min^{-1}. The resulting scans were generally background corrected and indexed using entries from the Crystallography Open Database (COD).

X-Ray Absorption Spectroscopy

X-ray absorption near-edge structure (XANES) and extended X-ray absorption fine-structure (EXAFS) measurements of pure and doped BFO powder samples were carried out at multiple beamlines of the Stanford Synchrotron Radiation Lightsource on the SLAC National Accelerator Laboratory campus. X-ray absorption fluorescence was collected at the K edge of the dopant in question using a 32 element Ge fluorescence detector and Si 220 double monochromator. All data was collected at 10 K using an Oxford He cryostat.

Photoelectrochemical Water Splitting

Substrate deposited samples on FTO were generally ready for photoelectrochemical measurements and were used directly as the working electrode

in the cell. Powder samples had to be deposited on a conductive substrate (FTO) via airbrushing or drop casting. For this, an ink suspension of 5 mg mL^{-1} in ethanol was prepared and sprayed onto a 1 x 1 cm^2 exposed area of a 1 x 1.5 cm^2 piece of clean FTO. A two-part, alkaline resistant epoxy was put around the edges of the sample to ensure that only the active material surface was in contact with the electrolyte in the cell. After drying, the electrode was placed in a 3-cell quartz glass separated cell with a saturated Ag/AgCl reference electrode, carbon rod counter electrode, and 1 M NaOH electrolyte with pH 13.6. J-V and i-t measurements were recorded using a CHI 660D electrochemical workstation (CH instruments Inc.) with a Newport Model 69907 solar simulator fitted with an AM 1.5G filter on the 150 W Xe lamp white light source. The cell was placed so that the electrode surface was in line with 100 mW cm^{-2} incident power density reading.

Energy Storage

Pristine and post treated substrate deposited samples, as well as slurry cast powder samples were used as aqueous energy storage electrodes. In the case of powder samples, the slurry was made by mixing 70 wt.% hematite, 20 wt.% acetylene black, 10 wt.% polyvinylidene fluoride binder in N-methyl-2-pyrrolidone solvent spread at a thickness of 200 μm onto 400 μm thick carbon paper. The electrodes were then placed in a vacuum oven at 60 ˚C for 12 h. The electrodes' performances as aqueous supercapacitors were studied in a 3-electrode beaker cell with a saturated calomel reference electrode, carbon paper counter electrode, and 3 M LiCl

electrolyte. All electrochemical measurements were taken using a SP-300 BioLogic electrochemical workstation.

Conductivity Measurements

For bulk conductivity measurements, hematite powder samples were pressed into circular pellets of 1 cm diameter and approximately 2 mm thickness in a high-precision steel pellet die. The optimized process involved mixing 185 mg of hematite powder with 37 μL of 100 mg mL^{-1} polyvinyl alcohol in water in Thinky planetary centrifugal mixer with ZrO_2 mixing beads. The resulting suspension was pressed to a pressure of 160 MPa for 5 min in a benchtop hydraulic press before slowly releasing the pressure over 2 min. The resulting pellet was dried in an oven at 60 ˚C for 4 h and were mechanically stable enough for testing. Both sides of the pellet were painted with Ag paint to ensure good contact and placed into a Swagelok cell, pressed between the two steel piston contacts. Linear sweep voltammetry measurements were carried out using a CHI 660D electrochemical workstation (CH instruments Inc.).

2.4 Results and Discussion

2.4.1 Fractional Dopant Oxide Precipitation

Heteroatom doping is well known to generally improve electronic properties of hematite, and it is therefore of interest to see exactly how far this type of material engineering can go before that enhancement is diminished or otherwise disappears entirely. Previous theoretical work done in our lab calculated the critical dopant concentration of various n-type dopants as a function of synthesis temperature. It is

suggested that this is a functional saturation point in the hematite crystal and that the majority of dopant present beyond that concentration will precipitate from the material and manifest as dopant oxide. Sn and Ge doped hematite photoanode performance aligned quite well with the theoretical critical concentration for both dopants. As seen in (Table 2.2), Sn and Ge are expected to be maximally doped at 0.52% and 1.00% at 900 ˚C and 1.11% and 2.02% at 1000 ˚C. (Figure 2.5a,b) show greatly enhanced photocurrent with 100 mW cm^{-2} simulated solar irradiation when the dopant is at or below this critical concentration. 0.5% Sn exhibits a nearly 200x increase in photocurrent over pristine hematite, but 1.0% and 2.0% (both significantly above the critical concentration) show hampered performance. Ge samples strongly support trend because the 0.5% and 1.0% additively improve over pristine hematite (~130x and ~320x photocurrent respectively) but the 2.0% sample shows significantly decreased performance due to exceeding the critical concentration. The same pattern is observed in samples prepared at 1000 ˚C (Figure 2.6c,d). Photocurrent increases with doping concentration until the critical concentration for that particular dopant prepared at a given temperature is surpassed.

Table 2.2 The calculated critical concentration of common (4+) dopants in hematite. Temperatures are synthesis temperatures at standard pressure in air. Concentrations expressed as at.%. Data from ref. ([41]).

Dopant	800 °C	900 °C	1000 °C
Ti	0.37%	0.82%	1.67%
Ge	0.44%	1.00%	2.02%
Sn	0.22%	0.52%	1.11%

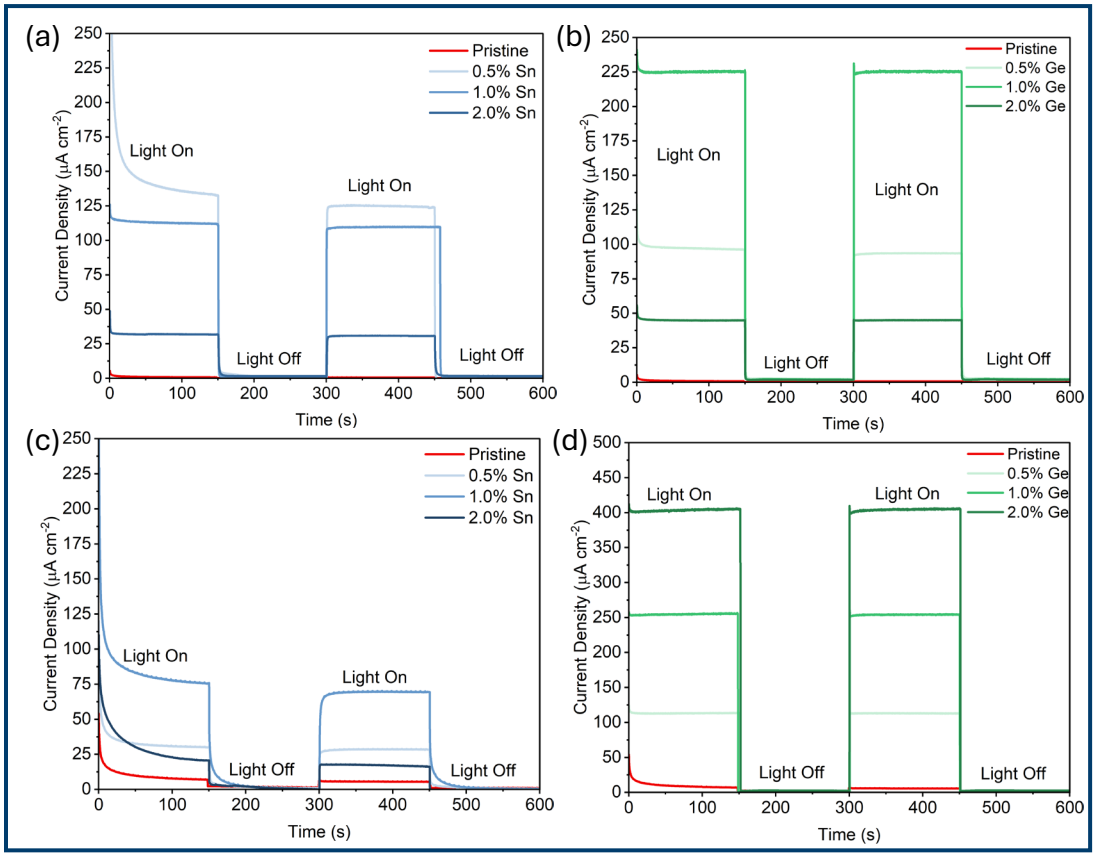

Figure 2.5 Chronoamperometric plots of pristine and Sn and Ge doped hematite powder annealed at 900 ˚C (a,b) and 1000 ˚C (c,d) drop cast on FTO with chopped

illumination. Collected in a quartz, 3 chamber photoelectrochemical cell with 1 M NaOH electrolyte and Ag/AgCl (sat. KCl) reference, carbon rod counter, and hematite working electrodes. Potential held at 1.6 V vs. RHE.

This is further supported by a following EXAFS study that shows that dopant oxide does indeed begin to form above the calculated critical concentrations (Figure 2.6). However, EXAFS data did show that a sample prepared above the critical concentration had a fraction of dopant found to be in the oxide phase rather than substitutionally doped into hematite, and that it increased logarithmically with total dopant concentration. Dopant oxide fraction is determined from fitting of the r-space EXAFS with models of pure hematite, doped hematite, and dopant oxide. The best fit for Ge doped samples was the exotic $Fe_8Ge_3O_{18}$ oxide and seems to be the most likely manifestation of Ge precipitation from hematite. The real part of the Fourier Transform (R) gives the identity and position of neighboring atoms. Importantly, the Sn-O peak at the dotted line at 1.5 Å is maintained across concentrations, while the average Ge-O peak at the dotted line at 1.4 Å shifts to shorter distances with concentration increase. Also, the amplitude of the 2.75 Å peak near 2.75 Å decreases but the overall shape of R does not change as the Sn concentration increases. Without meaningful change in structure from 2.25 – 3.25 Å, this amplitude change suggests a decreasing fraction of Sn-substituted hematite. Meanwhile, larger changes occur above 3 Å: a peak-dip-peak structure (3.2–3.6 Å) becomes a dip-peak-dip structure. For Ge, the amplitude evolution is slower, and small changes begin halfway through the sample series. At low concentrations, there

is little structure in far shells, however, beginning at 2.28% Ge, a well-defined peak corresponding to $Fe_8Ge_3O_{18}$ emerges near 4.0 Å, denoted by a vertical line. From these features, variable fits yield quantitative fractions of dopant in hematite and in the oxide. The fits suggest that above the critical concentration for a given temperature, excess dopant was still substituting Fe as well as precipitating.

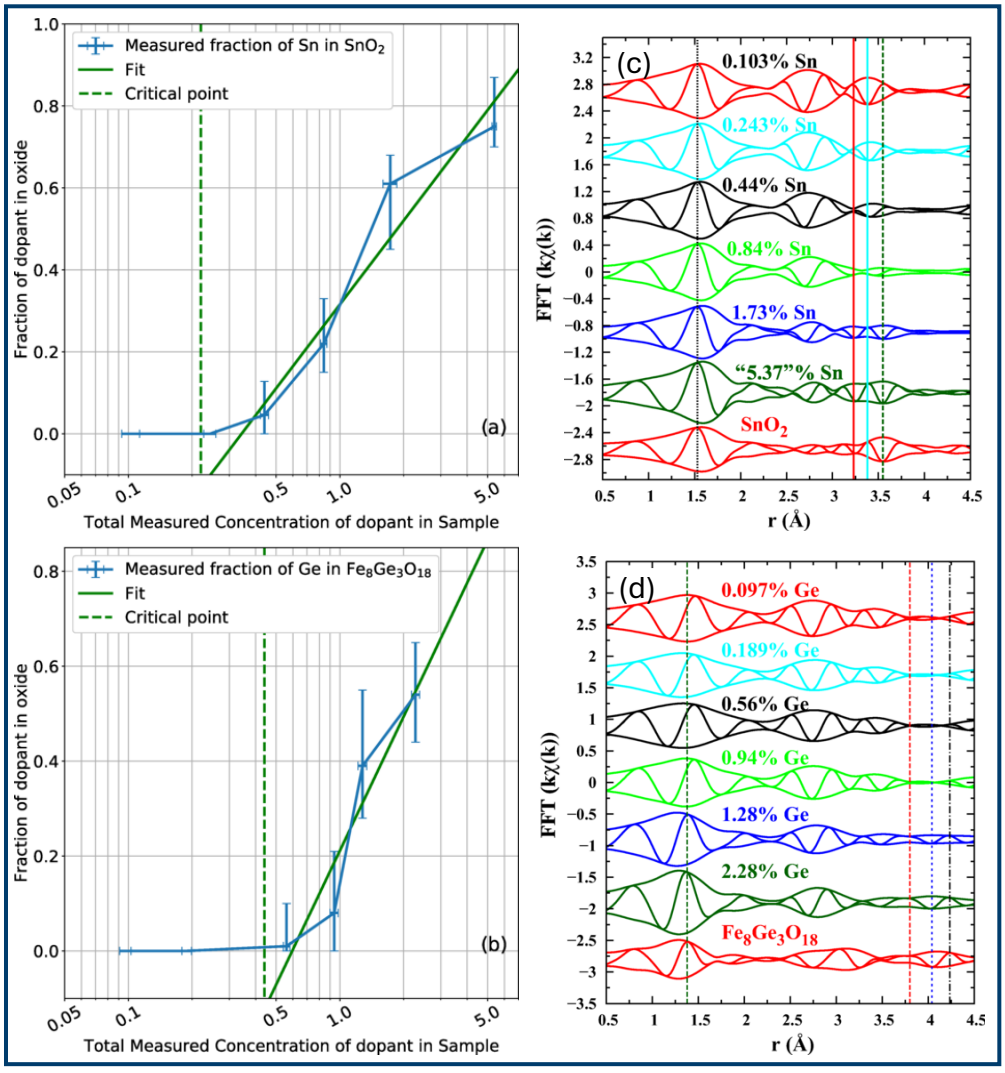

Figure 2.6 (a, b) Logarithmic plots of fraction of dopant oxide in samples as a function of total measured dopant concentration from X-ray absorption step heights.

SnO_2, and $Fe_8Ge_3O_{18}$ are the native dopant oxides for Sn and Ge dopant determined via EXAFS characterization. Samples were prepared at 800 ˚C. (c, d) Evolution of EXAFS structure in r-space. Both profiles evolve from doped hematite toward dopant oxide in both position and amplitude particularly at distances marked by vertical solid and dashed lines. Reproduced with permission from ref. ([43]). Copyright 2025 American Physical Society.

It is particularly significant that above the critical concentration, dopant is still being incorporated into hematite, only fractionally. It was upon this discovery that it is hypothesized that it may be possible to dope hematite above the critical concentration at a given temperature without dopant oxide interference by overshooting the critical concentration to exploit the extra doping and then subsequently selectively removing any oxide that forms. Secondly, it is reasonable to assume that dopant diffusion and precipitation occurs during sample cooling as the thermal energy dissipates and is no longer able to overcome the electrostatic forces that cause dopant segregation. It is proposed that rapid thermal quenching can halt the precipitation and supersaturate the dopant.

2.4.2 Selective Removal of Sn and Ge Oxides via Post-Process Washing

To see if dopant oxide can be selectively removed from the material, very high concentrations, nominally 10% Sn or 12% Ge, samples were prepared. By having a large excess of dopant, it is expected that some dopant will continue to fractionally dope beyond the critical concentration. Samples were prepared and washed, then

characterized using energy dispersive X-ray spectroscopy (EDS), XRD, Raman spectroscopy, and EXAFS. Elemental mapping and quantitative total dopant concentrations for Ge samples show that post-process washing greatly reduced the amount dopant present in the sample (Figure 2.7).

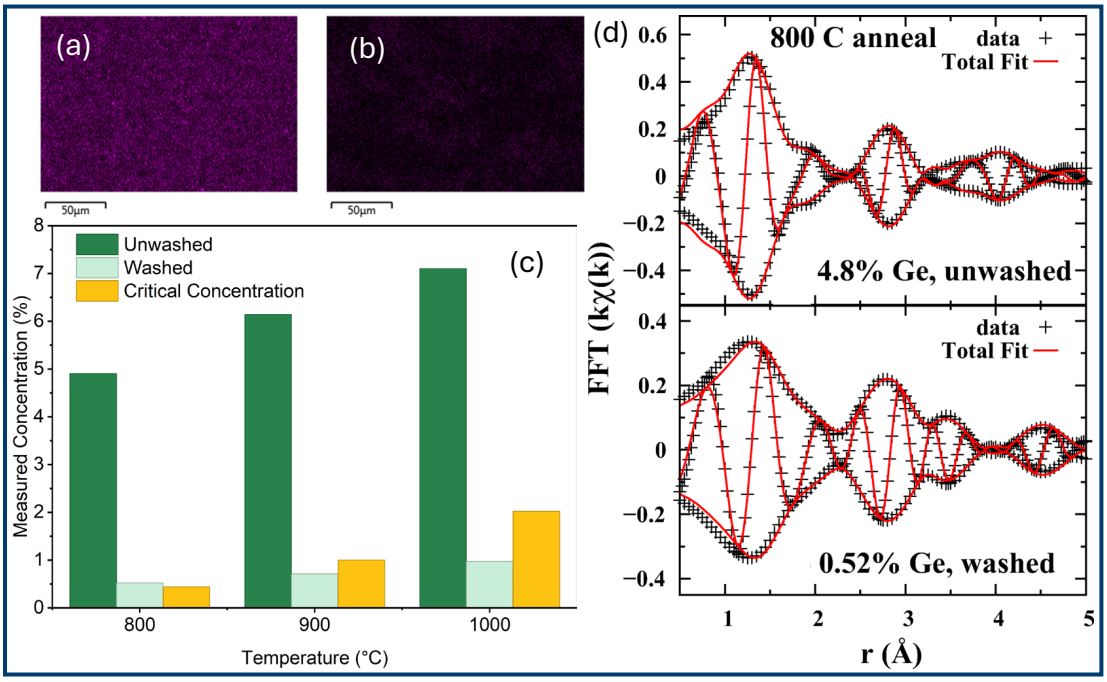

Figure 2.7 EDS Elemental mapping of 800 ˚C 12% Ge unwashed (a) and washed (b) and bar graph showing measured concentrations of each compared to the critical concentration for a given temperature. (d) r-space EXAFS plots of 800 ˚C 12% Ge with measured concentrations. Reproduced with permission from ref. ([43]). Copyright 2025 American Physical Society.

The EDS and EXAFS measured concentrations being significantly below the nominal 12% Ge concentration is attributed to the volatility of Ge precursors and intermediate phases and has been observed in previous work in our lab as well as

other studies.[50–53] While washing successfully removed approximately 90% of dopant in each case, it did not exhibit the expected behavior. For example, for 800 ˚C 12% (4.8% measured) Ge, EXAFS fits show that approximately 60% (amounting to 2.9%) of total measured dopant was in the oxide phase and 40% (amounting to 1.9%) was doped into hematite. This means that a sizable fraction of doped Ge was removed along with the unwanted dopant oxide, i.e. the wash was not as selective as expected. This also serves as evidence to corroborate other studies that aliovalent dopants, and especially Ge, tend to segregate to the particle surface.[34,44] This doped surface layer is susceptible to the highly alkaline, high temperature washing procedure.

These same powder samples were then tested as electrodes in a PEC cell and aqueous supercapacitor system (Figure 2.8). The areal capacitance, C_A, of the electrode can be calculated from the galvanostatic charge-discharge curves according to the following equation:

$$C_A = \frac{I\Delta t}{A\Delta V} \qquad \text{(Eq. 2.1)}$$

where I is the applied current, Δt is the discharge time, A is the electrode area, and ΔV is the potential window accounting for iR drop. As expected, the unwashed doped samples show significant increase in photocurrent and areal capacitance over pristine samples. However, the performance is still worse than samples doped below the critical concentration, again suggesting that excess dopant found in oxide is detrimental to the performance. After washing, the doped samples perform worse than unwashed, with both photocurrent and areal capacitance dropping significantly. In the

case of areal capacitance, the washed samples actually perform worse than pristine hematite. In the PEC mechanism, bulk electronic properties matter more. Ge that successfully doped into the bulk lattice and was therefore protected form the washing procedure are able to contribute donor density and charge transport in the bulk. This is a net benefit for PEC performance. The supercapacitor mechanism is surface and interface dominated, meaning that major changes to the material surface from the alkaline wash can affect the performance. While slight, α-Fe_2O_3 does have some solubility in alkaline environments, especially at high temperature. The wash may etch and dissolve the α-Fe_2O_3 surface and disrupt surface chemistry. Also, it is likely that surface segregated Ge is not exclusively in the oxide phase and may actually be in a substituted/grain boundary segregated state that is still electrochemically active and beneficial for capacitance. Removing this Ge decimates the capacitance improvement observed in unwashed samples. And finally, Ge and Sn oxides themselves contribute some capacitive behavior. This highlights the goal-specific engineering required in hematite doping. Different dopants have different benefits and activities depending on the system the material is used in and thus demands consideration of what dopant should be used and how it should be implemented. In light of this, it becomes necessary to probe these systems further to better understand surface chemistry and the potential for post-process washing as a strategy to optimize doped hematite toward specific applications.

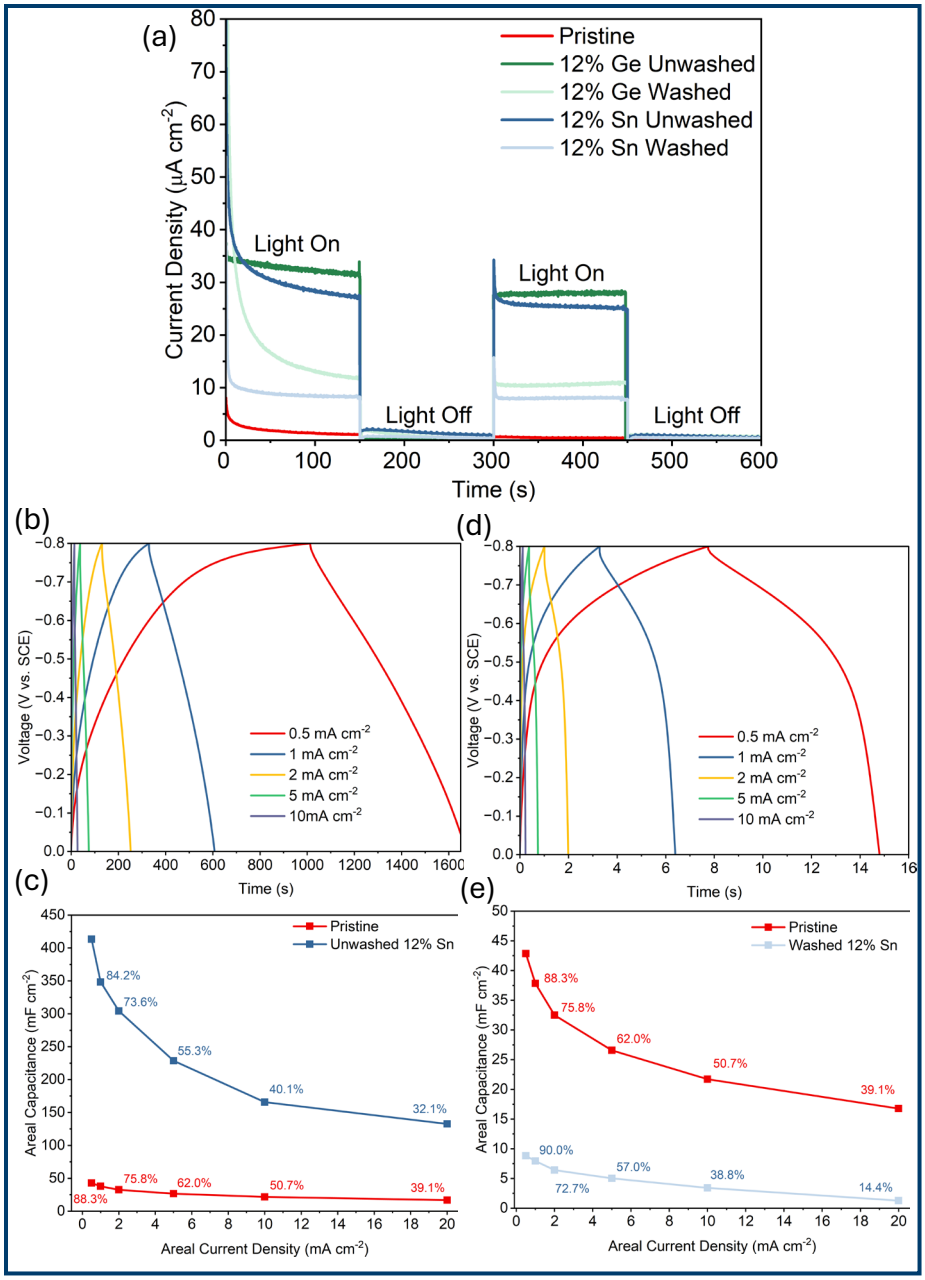

Figure 2.8 (a) Chronoamperometric plots of pristine and Sn and Ge doped hematite powder annealed at 800 ˚C drop cast on FTO with chopped illumination. GCD curves of unwashed (b) and washed (d) and areal capacitance calculated from GCD as a

function of operating current density for unwashed (c) and washed (e) 12% Sn samples annealed at 800 ˚C and slurry cast onto carbon paper.

2.4.3 Dopant Oxide Suppression via Rapid Cooling

Rather than retroactively remediating any dopant oxide that may form via post-process washing, it is of interest to see if it is possible to hinder its formation during the synthesis of the material. This would, in principle, allow for dopant concentrations to exceed the equilibrium solubility limit dictated by the critical concentration. Several studies in the PEC hematite literature have suggested that incorporating dopants via a β-FeOOH (akaganeite) precursor, followed by high-temperature conversion to α-Fe_2O_3 yields more uniform dopant distribution and better lattice incorporation than doping pre-formed hematite directly. The akaganeite structure features 2 × 2 octahedral tunnels (~0.5 nm across) that natively host anions and accommodate cation guests, providing a low-barrier diffusion pathway that is unavailable in the dense corundum framework of α-Fe_2O_3 .[54] The subsequent transformation to hematite proceeds topotactically through related oxyhydroxide systems, preserving the oxygen sublattice and minimizing cation displacement, which is invoked to explain how dopants already coordinated in the precursor are carried into octahedral Fe sites of the product.[55,56] In practice, this rationale underlies the now-common synthesis of Sn-, Ti-, Si-, Zr-, Ge-, and Be-doped hematite photoanodes via β-FeOOH templates, with reports noting that this "ex situ" approach decouples the dopant variable from morphological changes.[57–59] Despite these discussions the literature does not, to our knowledge, contain a controlled head-to-head comparison

of dopant solubility or diffusion coefficients in β-FeOOH versus α-Fe_2O_3. The case for the precursor route is thus assembled from structural, kinetic, and empirical strands rather than direct measurement. The collective evidence strongly suggests that the oxyhydroxide route enables dopant uptake beyond what diffusion-limited incorporation into hematite can achieve.

For this reason, a series of Ge doped samples, 1%, 5%, 10% prepared with either β-FeOOH or α-Fe_2O_3, were made using the rapid cooling apparatus. They are denoted FeOOH and Fe_2O_3 to signify the starting material, but all samples were annealed at high temperature and converted to doped hematite. In one case, samples are allowed to cool normally and are denoted U (unquenched) and in another were rapidly cooled and denoted Q (quenched). This set of samples lets us compare the effect of quenching on the dopant incorporation in the traditional synthesis route (starting from β-FeOOH), and also provide direct insight into the differences in dopant incorporation when starting from already formed α-Fe_2O_3.

XRD patterns show no major differences in phase or crystallinity among samples made with FeOOH precursor (Figure 2.9). This is not entirely surprising as even if 100% of the dopant added was converted to dopant oxide, it would likely be in too low concentration to detect with the diffractometer used. EXAFS reciprocal space data show that 1% FeOOH-U and 1% FeOOH-Q have similar structures to each other: a mixture of doped Ge and Ge oxide. In general, 5% FeOOH-U and 5% FeOOH-Q have a similar structure as the 1% samples, but at approximately 2.75 Å, 5% FeOOH-Q exhibits a larger amplitude. According to the best model fits, this

suggests that a higher fraction of Ge is substitutionally doped than in 5% FeOOH-U. While the difference is small, it is a significant clue that quenching may, in fact, be increasing the fraction of substitutional dopant versus dopant oxide.

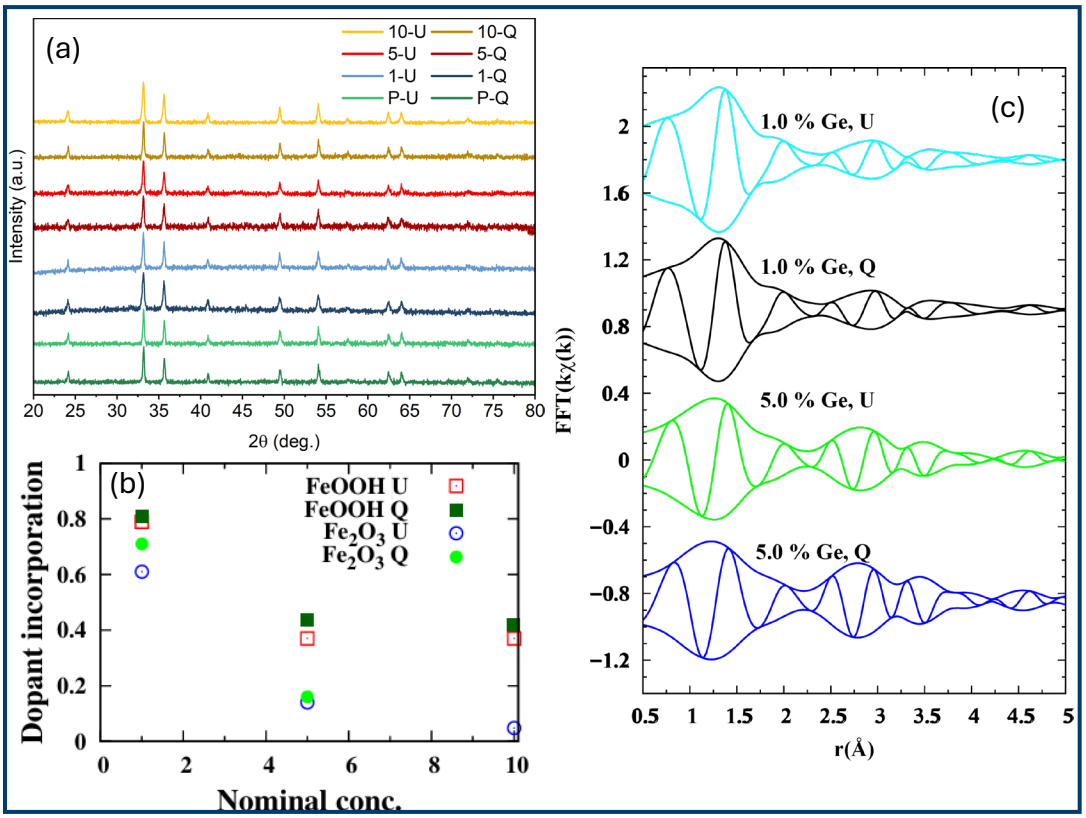

Figure 2.9 (a) XRD patterns of unquenched (U) and quenched (Q) pure (P), 1% (1), 5% (5), and 10% (10) Ge doped hematite made from FeOOH precursor. (b) Plot of measured concentration as a function of nominal concentration. Dopant incorporation expresses measured concentration as a percentage of nominal concentration. (c) EXAFS FFT plots of select unquenched and quenched Ge doped samples.

This is supported by the plot of measured concentrations as a function of nominal concentration. Concentration (C) is measured from XANES step-height analysis using the following equation:

$$C = \frac{SH_{Ge}}{SH_{Fe}} \times SH\ Ratio_{Theory} \quad \text{(Eq. 2.2)}$$

where SH_{Ge} is the Ge absorbance step height, SH_{Fe} is the Fe absorbance step height, and $SH\ Ratio_{Theory}$ is the theoretical ratio of Ge/Fe per-atom step heights derived from the absorption cross-section of each element.

In all cases, quenched samples measured higher Ge content compared to unquenched samples. This is then taken as a percentage of the nominal concentration and then plotted as a function of nominal concentration for each sample (Figure 2.9b). As Ge volatilization is generally from Ge oxides[50,51,53], this suggests that quenching does incorporate more Ge substitutionally. While this result is systematic and exhibited by all measured samples, the effect is quite small, ranging from 0.02% - 0.1% difference. It is now hypothesized that the quenching did not occur rapidly enough, and that the multi-second process of dropping the sample into the coolant and then fully cooling was insufficient. If a more controlled rapid cooling apparatus can be constructed, it is likely that the difference in synthesis will produce self-consistent results that can provide prove or disprove the hypothesis. A vertical induction heater with precise temperature control and a series of cooling rates would allow for a detailed investigation of this process.

Table 2.3 Measured step heights for Fe and Ge X-ray absorption and resultant measured concentration for rapid cooling samples.

Sample	Fe SH	Ge SH	Measured Ge Concentration (at.%)
1% FeOOH-U	0.4687	0.002218	0.79%
1% FeOOH-Q	0.5369	0.00260	0.81%
1% Fe_2O_3-U	0.661	0.00242	0.61%
1% Fe_2O_3-Q	0.4655	0.00195	0.70%
5% FeOOH-U	0.67	0.00742	1.9%
5% FeOOH-Q	0.711	0.00928	2.2%
5% Fe_2O_3-U	0.548	0.00231	0.71%
5% Fe_2O_3-Q	0.554	0.00256	0.78%
10% FeOOH-U	0.621	0.0137	3.7%
10% FeOOH-Q	0.611	0.0153	4.2%
10% Fe_2O_3-U	0.5969	0.00173	0.48%`
10% Fe_2O_3-Q	N/A	N/A	N/A

The conductivity of these samples was measured by pressing the sample into pellets and measuring current response when voltage was applied across the pellet (Figure 2.10). In all cases, unquenched samples had much better conductivity than quenched samples, and doped samples were significantly worse than pristine samples. However, while doped samples performed worse overall, the higher the doping percentage, the higher the current. While this measurement is inherently flawed due to the large contribution of resistance at grain boundaries in the polycrystalline pellet, the relative measured current does reflect an interesting result. Adding Ge dopant to this synthesis greatly hindered conductivity but still showed improvement with increasing concentration. This aligns with the understanding that Ge dopant is likely segregated to the surface. Once pellets were pressed, grain boundaries consist mostly of Ge oxide and have large resistance. Nevertheless, as observed before, the small fraction of Ge that acts as a bulk substitutional dopant does improve the conductivity within the crystallite.

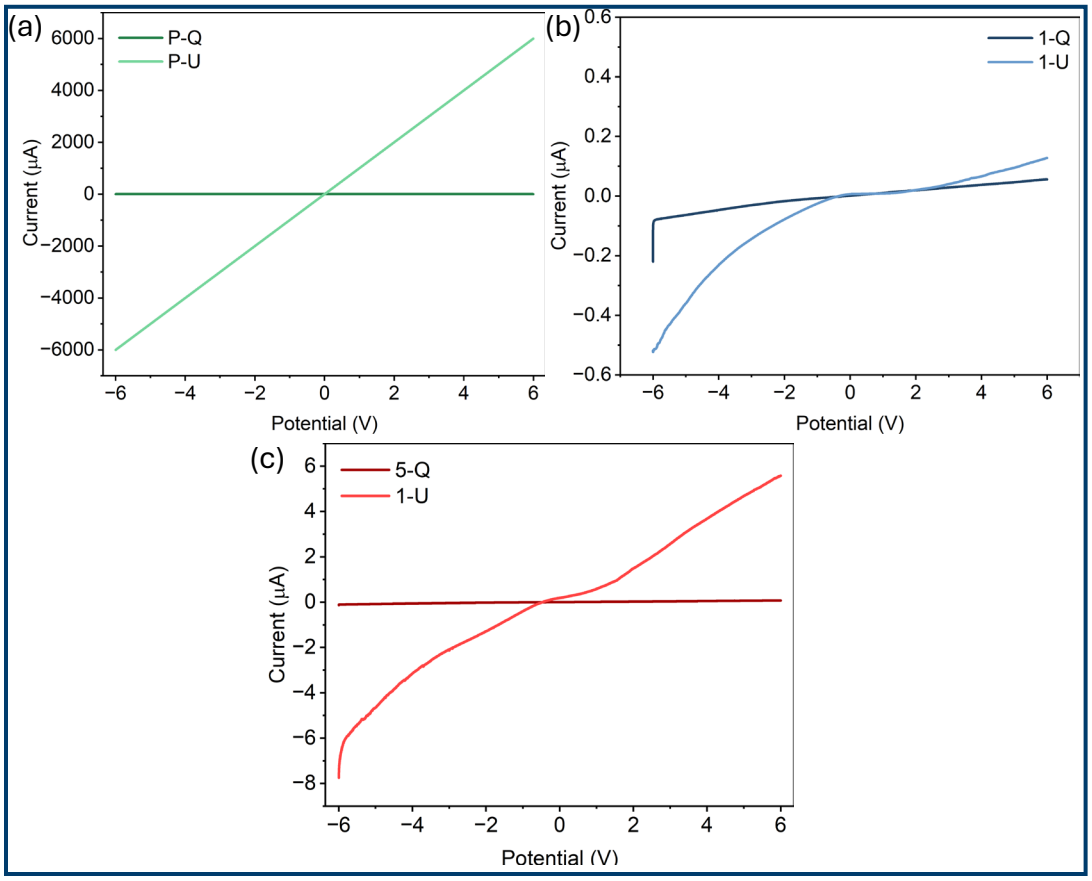

Figure 2.10 i-V plots of pristine (a), 1% Ge doped (b), and 5% Ge doped (c) samples comparing quenched to unquenched.

2.5 Conclusion

This chapter investigated two synthetic strategies to circumvent the detrimental formation of dopant oxide secondary phases in Sn- and Ge-doped hematite: rapid thermal quenching and post-process alkaline etching. Prior EXAFS analysis established that dopant oxide formation manifestsas SnO_2 and the exotic $Fe_8Ge_3O_{18}$ phase and tends to increase logarithmically with total dopant concentration above the thermodynamically derived critical concentration. Critically, EXAFS fitting

confirmed that even above this threshold, dopant continues to fractionally incorporate substitutionally into the hematite lattice alongside the precipitating oxide, motivating both the washing and quenching strategies explored here.

Alkaline etching at 120 °C in 5 M NaOH successfully removed approximately 90% of total dopant from heavily loaded samples (nominally 12% Ge, measured ~4.8% by XANES step-height analysis). However, EXAFS fitting of the washed 800 ˚C 12% Ge sample revealed that roughly 60% of measured dopant had resided in the oxide phase and 40% was substitutionally incorporated. The loss of this substitutional fraction alongside the oxide confirmed that the wash was insufficiently selective, likely because surface-segregated Ge occupies grain boundary and near-surface lattice sites that are equally accessible to the alkaline etchant. The electrochemical consequences were application-dependent: washed Ge-doped samples retained some PEC benefit from bulk-protected substitutional dopant, while areal capacitance of washed 800 °C 12% Sn samples fell below that of pristine hematite, reflecting the dominant role of surface and interfacial chemistry in the supercapacitor mechanism. This result highlights a fundamental tension in post-process surface treatments: strategies that remove parasitic oxide phases risk simultaneously stripping electrochemically active, near-surface dopant that is beneficial, particularly for energy storage.

The rapid cooling experiments produced more ambiguous results. Ge-doped samples prepared at nominally 1% and 5% and quenched into ice water showed consistently higher total dopant retention than unquenched counterparts (e.g., 2.2 vs.

1.9 at.% measured Ge at 5% nominal loading), consistent with suppression of Ge volatilization that occurs during slow cooling. However, EXAFS fitting suggested that the 5% unquenched sample contained a higher fraction of substitutionally incorporated Ge than the quenched equivalent, the opposite of what kinetic trapping predicts. This counterintuitive result is attributed to the limited reproducibility of the induction heating apparatus, which precluded precise temperature control during the annealing plateau. Conductivity measurements on pressed pellets corroborated that Ge segregation to grain boundaries dominates transport in these samples: all doped pellets showed dramatically reduced conductivity relative to pristine hematite, though conductivity did improve with increasing Ge concentration within the doped series, consistent with a small but real bulk substitutional doping contribution.

Taken together, these results establish that the dopant phase is a decisive parameter governing hematite performance in both photoelectrochemical and energy storage contexts, and that neither alkaline etching nor rapid quenching, as implemented here, achieved the selectivity or reproducibility required to reliably exploit this distinction. A more precisely controlled rapid cooling apparatus, combined with surface-sensitive techniques such as XPS depth profiling or operando XANES, would be valuable to rigorously test the kinetic trapping hypothesis and deconvolute the contributions of bulk and surface dopant environments to device performance.

2.6 References

1. Grätzel, M. *Nature* **2001**, *414* (6861), 338–344.
2. Holmes-Gentle, I.; Tembhurne, S.; et al. *Nat Energy* **2023**, *8* (6), 586–596.
3. Lyu, H.; Hisatomi, T.; et al. *Chem. Sci.* **2019**, *10* (11), 3196–3201.
4. Fujishima, A.; Honda, K. *Nature* **1972**, *238* (5358), 37–38.
5. Nasejje, S.; Mukhokosi, E. P.; et al. *Discov Mater* **2024**, *4* (1), 44.
6. Kumar Jha, B.; Chaule, S.; et al. *Materials Chemistry Frontiers* **2024**, *8* (10), 2197–2226.
7. Pina, J.; Dias, P.; et al. *J. Phys. Chem. C* **2021**, *125* (15), 8274–8284.
8. Liu, H.; Fan, X.; et al. *Journal of Environmental Chemical Engineering* **2023**, *11* (1), 109224.
9. Ling, Y.; Wang, G.; et al. *Nano Lett.* **2011**, *11* (5), 2119–2125.
10. Wang, G.; Ling, Y.; et al. *Nano Lett.* **2011**, *11* (8), 3503–3509.
11. Shivakumara, S.; Penki, T. R.; et al. *Materials Letters* **2014**, *131*, 100–103.
12. Poonam; Sharma, K.; et al. *Journal of Energy Storage* **2019**, *21*, 801–825.
13. Nithya, V. D.; Arul, N. S. *Journal of Power Sources* **2016**, *327*, 297–318.
14. Gao, Y.; Wu, D.; et al. *Electrochimica Acta* **2016**, *191*, 275–283.
15. Nie, G.; Lu, X.; et al. *Electrochimica Acta* **2017**, *231*, 36–43.
16. Yan, Y.; Tang, H.; et al. *Energies* **2017**, *10* (9), 1296.
17. Tofanello, A.; Shen, S.; et al. *APL Mater.* **2020**, *8* (4), 040905.
18. Rohilla, J.; Ingole, P. P. *Current Opinion in Green and Sustainable Chemistry* **2021**, *29*, 100455.

19. Ho-Kimura, S.; Williamson, B. A. D.; et al. *ACS Omega* **2019**, *4* (1), 1449–1459.
20. Tang, X.; Jia, R.; et al. *ACS Appl. Mater. Interfaces* **2015**, *7* (49), 27518–27525.
21. Safari, M.; Mazloom, J.; et al. *Sci Rep* **2022**, *12* (1), 14919.
22. Ling, Y.; Wang, G.; et al. *Nano Lett.* **2011**, *11* (5), 2119–2125.
23. Shen, S.; Kronawitter, C. X.; et al. *J. Mater. Chem. A* **2013**, *1* (46), 14498–14506.
24. Deleuze, P.-M.; Magnan, H.; et al. *J. Phys. Chem. Lett.* **2021**, *12* (47), 11520–11527.
25. Shen, S.; X. Kronawitter, C.; et al. *Journal of Materials Chemistry A* **2013**, *1* (46), 14498–14506.
26. Aalim, M.; Altaf, U.; et al. *J Solid State Electrochem* **2024**, *28* (1), 1–18.
27. Tian, C. M.; Li, W.-W.; et al. *J. Phys. Chem. C* **2020**, *124* (23), 12548–12558.
28. Yoon, K.-Y.; Park, J.; et al. *ACS Catal.* **2022**, *12* (9), 5112–5122.
29. Liu, J.; Liang, C.; et al. *Chem. Commun.* **2011**, *47* (28), 8040–8042.
30. Liu, J.; Cai, Y. Y.; et al. *Nano Energy* **2014**, *9*, 282–290.
31. Liu, J.; Liang, C.; et al. *Nano Energy* **2013**, *2* (3), 328–336.
32. Zhao, L.; Xiao, J.; et al. *International Journal of Hydrogen Energy* **2018**, *43* (28), 12646–12652.
33. Liu, J.; Liang, C.; et al. *J. Phys. Chem. C* **2012**, *116* (8), 4986–4992.
34. Yoon, K.-Y.; Park, J.; et al. *Nat Commun* **2021**, *12* (1), 4309.
35. Xiao, C.; Zhou, Z.; et al. *Nanoscale Res Lett* **2020**, *15*, 54.

36. Qiu, P.; Yang, H.; et al. *Electrochimica Acta* **2018**, *266*, 431–440.

37. Sivula, K.; Zboril, R.; et al. *J. Am. Chem. Soc.* **2010**, *132* (21), 7436–7444.

38. Park, J.; Kang, J.; et al. *Journal of Materials Chemistry A* **2023**, *11* (45), 24551–24565.

39. Zhou, Z.; Huo, P.; et al. *J. Phys. Chem. C* **2015**, *119* (47), 26303–26310.

40. Smart, T. J.; Baltazar, V. U.; et al. *Chem. Mater.* **2021**, *33* (12), 4390–4398.

41. Smart, T. J.; Chen, M.; et al. *J. Appl. Phys.* **2021**, *130* (24), 245705.

42. Zhang, Z.; Tsuchimochi, T.; et al. *Nat Commun* **2022**, *13* (1), 1499.

43. Mayford, K.; McNair, S.; et al. *Phys. Rev. Mater.* **2025**, *9* (9), 095802.

44. de Lima, F. C.; Schleder, G. R.; et al. *Appl. Phys. Lett.* **2021**, *118* (20), 201602.

45. Zhang, Z.; Karimata, I.; et al. *Nat Commun* **2019**, *10*, 4832.

46. Ahn, H.-J.; Yoon, K.-Y.; et al. *ACS Catal.* **2018**, *8* (12), 11932–11939.

47. Xiao, J.; Huang, H.; et al. *Journal of Catalysis* **2017**, *350*, 48–55.

48. Zhang, H.; Hyun Park, J.; et al. *Chemical Science* **2019**, *10* (44), 10436–10444.

49. Yang, Y.; Forster, M.; et al. *Angewandte Chemie International Edition* **2016**, *55* (10), 3403–3407.

50. Villaescusa, L. A.; Camblor, M. A. *Chem. Mater.* **2016**, *28* (20), 7544–7550.

51. Oh, J.; Campbell, J. C. *J. Electron. Mater.* **2004**, *33* (4), 364–367.

52. Kaiser, R. J.; Koffel, S.; et al. *Microelectronic Engineering* **2011**, *88* (4), 499–502.

53. Altay, M. C.; Eroglu, S. *Thin Solid Films* **2019**, *677*, 22–27.

54. Post, J. E.; Heaney, P. J.; et al. *American Mineralogist* **2003**, *88* (5–6), 782–788.

55. Cudennec, Y.; Lecerf, A. *Solid State Sciences* **2005**, *7* (5), 520–529.

56. Cudennec, Y.; Lecerf, A. *Journal of Solid State Chemistry* **2006**, *179* (3), 716–722.

57. Subramanian, A.; Gracia-Espino, E.; et al. *Applied Surface Science* **2018**, *427*, 1203–1212.

58. Annamalai, A.; Lee, H. H.; et al. *Sci Rep* **2016**, *6* (1), 23183.

59. Liu, J.; Cai, Y. Y.; et al. *Nano Energy* **2014**, *9*, 282–290.

Chapter 3

Chemical Synthesis Routes for Doped Bismuth Ferrite: Phase Optimization and Preliminary Characterization

3.1 Abstract

Bismuth ferrite ($BiFeO_3$, BFO) is a room-temperature multiferroic perovskite oxide of sustained interest for optoelectronic, ferroelectric, and photocatalytic applications. Despite decades of study, reliable wet-chemical synthesis of phase-pure BFO remains non-trivial due to the volatility of bismuth and the thermodynamic favorability of competing secondary phases. Heteroatom doping further complicates synthesis by perturbing the lattice tolerance factor and introducing additional phase stability constraints. Herein, four wet-chemical synthesis routes: potentiostatic co-electrodeposition, Pechini polymer deposition, solution drop-casting, and xerogel processing, are developed and compared for the production of pure and doped BFO thin films and powders. Transition metal (Sn, Ge) and lanthanide (Yb, Er) dopants are incorporated across methods to probe structural and optical responses. Powder X-ray diffraction reveals route-dependent phase purity, with secondary phase formation observed as a function of synthesis conditions. Preliminary photoluminescence measurements of Yb/Er co-doped BFO motivate further investigation of BFO as a host crystal for photon upconversion. Photoelectrochemical and ferroelectric characterization are presented as exploratory measurements establishing baseline behavior and identifying instrumentation and contact-quality constraints for future

optimized studies. Finally, application in energy storage systems highlights yet another area where BFO may be of interest. Together, these results constitute a synthetic and preliminary characterization foundation for continued investigation of doped BFO in energy conversion and storage and photonic applications.

3.2 Introduction

Bismuth ferrite, with the chemical formula $BiFeO_3$ (commonly abbreviated to BFO), is a material whose properties sit at the intersection of several high interest fields. Current technological, environmental, and economic conditions have prompted worldwide mobilization to address the approaching ceiling of tradition electronic component miniaturization[1–3], and the need for fossil fuel alternatives for energy generation and storage.[4–6] Both dilemmas require creative approaches such as alternative physics for memory and computing, or cutting-edge efficiencies in solar utilization or electrochemical energy storage mechanisms.

Since first articulated in 1965, Moore's Law has been the preeminent observation/projection regarding semiconductor industry scaling. It posits that the transistor density of a microchip doubles approximately every 1-2 years. This is a trend that held mostly true until very recently as we approach the physical limit with near-atomic sized transistors and circuitry.[2,3] As computational needs continue to grow, researchers have begun to consider alternative physical principles by which to perform basic logic for computation. Some of the most promising leads are spintronics[7] and magnetoelectric materials.[8–10] Spintronics utilizes the inherent spin states of electrons as the basis for compute. One entry point for this would be

materials where electric and magnetic fields are coupled to allow control of one property through the other. These so-called magnetoelectric materials are a type of multiferroic material being developed for this and many other applications. The additional degree-of-freedom offered electronic spin orientation may allow a whole new dimension to encode information, thus increasing information density further.[11]

Global need for clean and renewable energy has pushed for rapid development of photovoltaic and solar fuel technologies. Demand has risen at a faster-than-average rate since 2024, with electricity demand increasing almost twice as fast as overall energy consumption. This is primarily driven by industrial growth, transport electrification, and the new demand of data centers.[12] Expected to continue growing at 4% through the next several years, total consumption is projected to increase by a staggering 3,500 TWh in that time.[13] Solar photovoltaics have been broadly implemented in recent years, reaching 2.2 TW and providing approximately 10% of global electricity at the end of 2024.[13] Despite this, the inherent limitations of intermittent sunlight from weather patterns and rotation of the planet cause serious concern of electric grid instability. Photoelectrochemical devices provide an alternative to use-it-or-lose-it electricity generation from photovoltaics or the need for large-scale battery centers. These devices utilize solar energy to drive electrochemical reactions to produce essential fuels and chemical precursors.[14–18] One of the most direct reactions is solar water-splitting to convert solar energy directly to stored chemical energy in the form of H_2 gas. The goal is to produce an integrated semiconductor system capable of generating hydrogen from water at high efficiency

and stability to store the absorbed energy. Hydrogen's exceptionally high gravimetric energy density of 143 kJ g^{-1} and clean combustion or use in a fuel cell make it a compelling candidate.[16,19,20] There are many initiatives calling for research in these fields in an effort to address our growing energy concerns.[21–24]

To address these questions through rational design and engineering, it is important to understand the crystal and electronic structure of the material. It is from this structure, and the manipulation of it, that the multiferroic, optoelectronic, and potential photoluminescent properties of BFO begin to come into focus. Many studies of doped BFO for these applications rely on highly precise, advanced, and costly growth techniques such as vacuum depositions like physical laser[25–27], chemical vapor[28–31], sputtering[32–34], and molecular beam epitaxy[35–37]. It is therefore of high importance to find simpler, more cost effective, and scalable chemical syntheses to produce pure and modified BFO for study and application.

3.2.1 Material Structure

BFO crystallizes as a distorted perovskite oxide of the general formula ABO_3, with two distinct cation sites of notably different sizes.[38] The ideal perovskite possesses a cubic structure where site A is occupied by a relatively large cation, surrounded by 16 oxygen ions, and site B is occupied by a relatively smaller cation, octahedrally coordinated to 6 oxygen ions.[39] Generally, the larger A-site and O ions form a face-centered cubic packing. Many stable perovskites deviate from this ideal structure due to its specific composition (ionic radii) or with variation in temperature

or pressure.[40] Compositional distortion can be predicted by the Goldschmidt tolerance factor t defined as:

$$t = \frac{r_A + r_O}{\sqrt{2}(r_B + r_O)} \quad \text{(Eq. 3.1)}$$

where r_A, r_B, and r_O are the ionic radii of the A-site cation, B-site cation, and oxygen anion respectively. With distortion, t decreases from 1, and generally ranges from 0.75 to 1 for stable perovskite structures.[41] Because the distortion can vary, naturally occurring and synthetic perovskites with rhombohedral, orthorhombic, monoclinic, tetragonal, etc. have all been observed. In the case of pure BFO, the Goldschmidt tolerance factor is approximately 0.90 (Shannon ionic radii)[41], and distorts to a rhombohedral structure of space group R3c, with a lattice constant $a = 5.63$ Å and rhombohedral angle $\alpha = 89.45°$.[42,43] This can be represented in both the rhombohedral and pseudocubic representations of the BFO unit cell (Figure 3.1). The rhombohedral distortion from the ideal cubic is of particular significance as it becomes noncentrosymmetric, fundamental to several of BFO's defining properties.

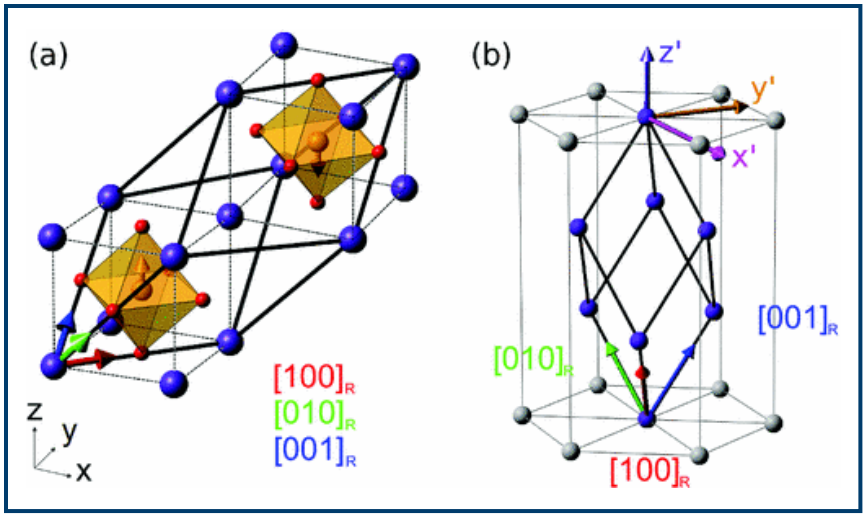

Figure 3.1 (a) Pseudocubic representation (dotted lines) of rhombohedral BFO with blue, orange, and red spheres representing bismuth, iron, and oxygen atoms respectively. Orange arrows represent spin, and red, green, and blue arrows represent unit vectors of the rhombohedral cell. Cartesian coordinates of the pseudocubic structure are depicted in the corner. (b) Trigonal cell (gray spheres, thin lines) with emphasis on the rhombohedral structure (blue spheres, thick lines). Reproduced with permission from ref ([44]). Copyright 2013 American Physical Society.

3.2.2 Multiferroic Properties

Since its initial synthesis in 1957 by Royen and Swars[45] and subsequent characterization of its antiferromagnetic, and ferroelectric properties[46], BFO has held the interest of solid-state physicists, material scientists, and chemists as one of the very few room-to-high-temperature multiferroic materials. These are materials that display two or more ferroic orderings simultaneously in a single crystalline phase (Figure 3.2a). The primary ferroic orders include ferromagnetism (spontaneous

aligned magnetic moments), ferroelectricity (spontaneous electric polarization), and ferroelasticity (spontaneous strain). The definition of multiferroic is often extended to include secondary orders such as ferrimagnetism (spontaneous alternating magnetic moments with net magnetization) or antiferromagnetism (spontaneous alternating magnetic moments with net zero magnetization) as in the case of BFO.[47,48]

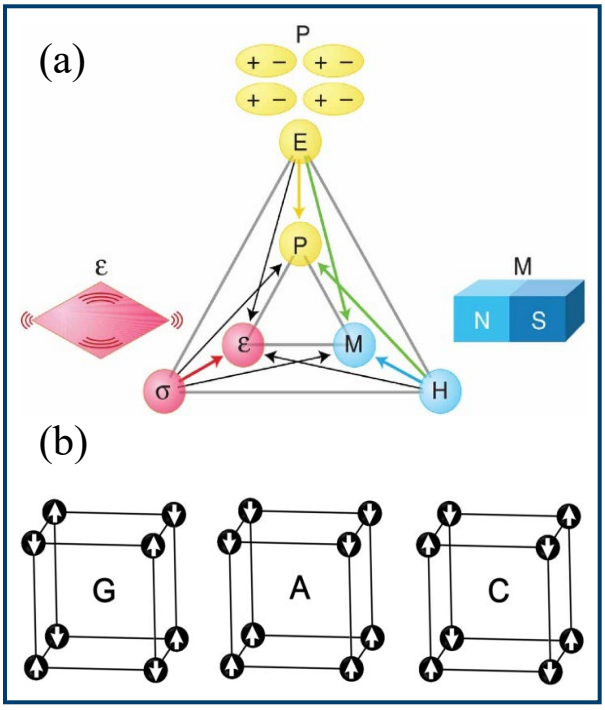

Figure 3.2 (a) Schematic diagram of coupling relationships among properties in multiferroic materials. The electric field E, magnetic field H, and stress σ control the electric polarization P, magnetization M, and strain ε, respectively. Reproduced with permission from ref. ([49]). Copyright 2005 AAAS. (b) Schematic depiction of G-, A- and C- type antiferromagnetic structures. Arrows represent spin orientation. Reproduced with permission from ref. ([50]). Copyright 2014 AIP Publishing.

Generally, magnetoelectric multiferroics (materials that specifically exhibit ferroelectricity and one form of magnetism) are exceedingly rare. This has been recognized for some years, particularly by Nicola Hill in 2000[51] who demonstrated that spontaneous electric polarization and spontaneous magnetism are properties that emerge from generally contradictory conditions. There are three main reasons for this, but simply put, the transition metal d electrons required for magnetism often interfere with the necessary symmetry-breaking that allows ferroelectricity from that same transition metal ion. As discussed by Hill, this can be circumvented, both naturally and synthetically, through a variety of mechanisms. In the case of BFO, classified as a Type-I magnetoelectric, its ferroelectricity and antiferromagnetism are independent in origin. The ferroelectricity is induced by the A-site Bi^{3+} ion, while the antiferromagnetism is induced by alternating magnetic ordering of the B-site Fe^{3+} ion. Because they originate from different locales, the coupling between the two is greatly diminished compared to Type-II magnetoelectrics that achieve ferroelectricity and magnetism from the same origin through other means.[48,51–53] Magnetoelectric coupling is of particular interest for the possible applications of electric field modulation of magnetism and vice-versa.[54] The ferroelectricity of BFO arises from the loss of inversion center when Bi^{3+} shifts from its ideal lattice site due to its 6s lone pair.[51,54–56] The antiferromagnetism arises via a common mechanism in Fe^{3+} scenarios where the d^5 electrons are all spin moment aligned, and through O 2p mediated exchange interaction, order with the neighboring Fe^{3+} d^5 so that they align antiparallel. This is a well-understood G-type magnetic ordering (Figure 3.2b) from

the large exchange interaction from the overlap integral of the aligned e_g and O 2p orbitals along the Fe—O bond.[57]

3.2.3 Optoelectronic Properties

In addition to its antiferromagnetic and ferroelectric ordering, BFO is an intrinsic semiconductor with a moderate bandgap of approximately 2.1-2.7 eV.[57,58] This broad range accounts for most reported measured and calculated values with the lower end characteristic of nanocrystalline and theoretical reports[59–61], and the higher values characteristic of bulk BFO or extended films.[27,62–64] It is highly dependent on the morphology, crystallography, and method of measurement/calculation. As with many metal oxide semiconductors, the valence band is comprised of hybridized O 2p and Fe 3d orbitals with some contribution from Bi 6s and 6p orbitals, while the low conduction band is primarily comprised of Fe 3d orbitals (Figure 3.3).[27,61] At room temperature there is an appreciable concentration of intrinsic defects that contribute mid-bandgap states and depending on the equilibrium Fermi level of the system and intended application, these can be beneficial as acceptor or donator states enhancing conductivity or can function as detrimental trap states interfering with absorption and charge transfer mechanisms.[38,42,57,65] These can be manipulated with extrinsic defect engineering, such as heteroatom doping (alio- or isovalent) or oxygen vacancy.

The most common exploitation of this band structure is in photovoltaic[67–71] or photoelectrochemical applications.[61,65,72–75] The moderate bandgap allows for visible light absorption to create excitons that can be used for electricity in a circuit or for

redox reactions in an electrochemical cell.[59,63,65,71] As a photo-active material, it does not necessarily outperform other state-of-the-art materials, but it does have potential for coupling its ferroelectric polarization with these technologies.[76–80] One very common drawback of metal oxide semiconductors is poor charge separation and fast electron-hole recombination.[81–85] This drastically decreases the efficiency of the material even if it has a high absorption coefficient. The ferroelectric polarization present in BFO can help improve charge separation and therefore the efficiency of the device.[86,87] This is highly dependent on the orientation and magnitude of the polarization, making them critical variables to be researched. Pure and doped BFO have both been studied used in work to decrease the bandgap (improve solar spectrum utilization) and affect the ferroelectric polarization to address charge separation concerns.

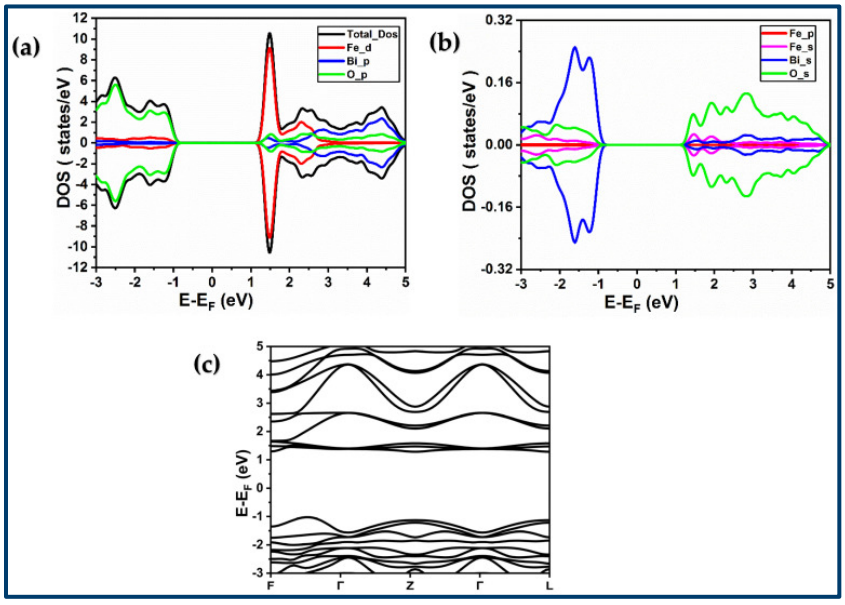

Figure 3.3 (a, b) Total and partial spin-resolved densities of states of $BiFeO_3$. (c) Band structure of $BiFeO_3$. Reproduced with permission from ref. ([66]). Copyright 2025 by authors.

3.2.4 BFO as a Photon Upconversion Host Crystal

This work proposes a novel use and preliminary investigation of employing BFO as the host crystal for photon upconversion active lanthanide dopants. Photon upconversion (UC) is an anti-Stokes emission whereby sequential absorption of two or more photons results in emission of a higher energy photon (Figure 3.4).[70,88–90] This is of great value to photoactive materials like BFO, because although it has a moderate bandgap compared to some metal oxide semiconductors, it still misses well over 50% if the incident solar radiation at the Earth's surface.[71,91] UC may extend solar utilization by allowing absorption of lower energy (red, near-IR, and even IR) radiation. There are several UC mechanisms, the most common and technologically relevant are excited-state absorption (ESA) and energy transfer upconversion (ETU).[92,93] ESA relies on the relatively long excited state lifetime where a single "activator" ion absorbs a photon, exciting the electron, and within the lifetime of this excited state, another photon is absorbed promoting the electron to a final higher excited state. The excitation pathways and probability of this are generally limited, and so the more commonly observed mechanism is ETU. ETU relies on two absorption sites, the same "activator" ion where the UC occurs, and the "sensitizer" ion that acts as a satellite absorption center that can then transfer the additional energy to the already excited activator neighbor. The probability of each of these processes

occurring together is quite low but is still observed if non-radiative relaxation is minimized. Crystals with lower phonon energy reduces non-radiative relaxation probability and is an essential consideration for UC materials.[70,89,90,93]

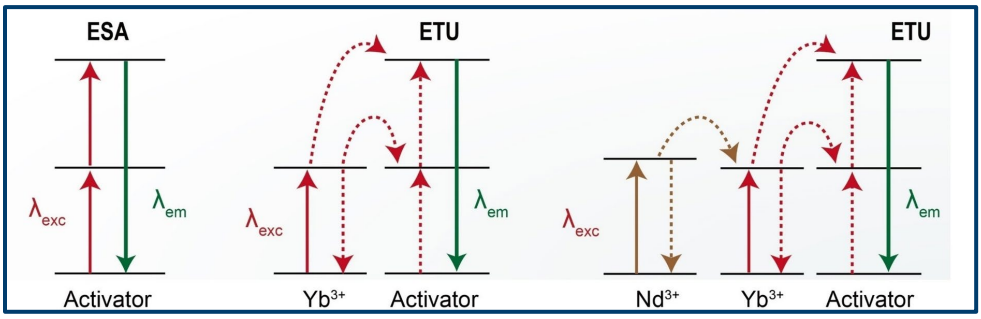

Figure 3.4 Schematic depictions of three common upconversion mechanisms. Solid arrows represent absorption or emissions; dotted arrows represent non-radiative energy transfers. Reproduced with permission from ref. ([94]). Copyright 2021 Wiley-VCH.

Lanthanides, making up most of the rare-earth metals, are the f-block elements of period 6 succeeding lanthanum, and are particularly suited for this phenomenon. Having a general electron configuration of $[Xe]6s^2 4f^n 5d^m$ (5d takes precedent in the case of lanthanum and gadolinium), most of their large 4f shells have many energy levels. The outer 5 and 6 shells tend to shield these orbitals, so their native electronic energy structure is maintained across many chemical environments.[95–98] Furthermore, these f orbitals often take a "ladder-like" structure where the energy differences among levels are near-equal (Figure 3.5a). These self-similar energy differences are perfect for sequential absorption.[90,93,99,100] Generally, f-f transitions are forbidden according to the Laporte selection rule, but this can be

relaxed when inversion is broken.[99] It is because of this unique electronic structure and selection rule exception that lanthanides comprise the most famous luminescent materials and are the prototypical UC centers. Yb^{3+} is a common sensitizer ion because it possesses only one excited state, while most other lanthanide ions have been demonstrated as activator centers in ESA or ETU systems (Figure 3.5b).

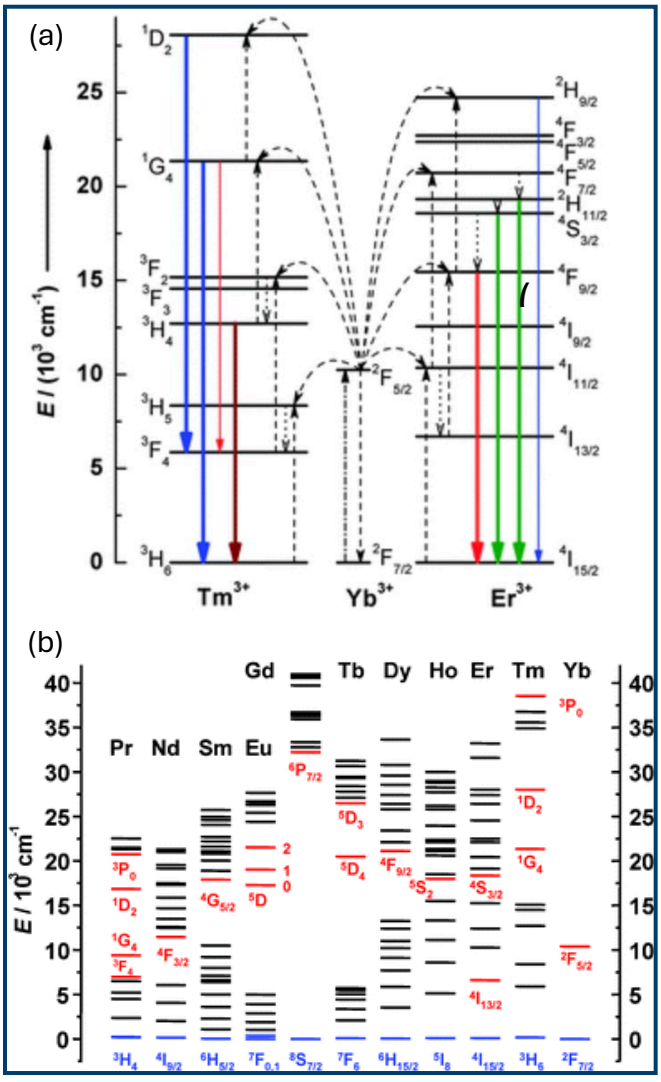

Figure 3.5 (a) Energy diagram of a dual-activator ETU system demonstrating the role of Yb^{3+} as a sensitizer ion. Reproduced with permission from ref. ([90]). Copyright 2009

The Royal Society of Chemistry. (b) Energy diagram for select lanthanide ions. The main luminescent levels are depicted in red, while the fundamental level is indicated in blue. Reproduced with permission from ref. ([101]). Copyright 2005 The Royal Society of Chemistry.

BFO offers a special case where the distorted perovskite oxide structure featuring the particularly large A-site Bi^{3+} is an ideal UC host. Most lanthanides readily form 3+ ions with radii similar enough to Bi^{3+} that they have long been studied as BFO dopants.[38,102] The lack of inversion center in the rhombohedral structure increases the probability and lifetime of f-f transitions overall increasing UC efficiency. And lastly, as an oxide, it has moderate phonon energy compared to other minerals, minimizing non-radiative relaxation pathways[94]. The rate of non-radiative relaxation, K_{NR}, can be estimated according to the proportionality:

$$K_{NR} \propto exp\left(-\beta \frac{\Delta E}{\hbar\omega_{max}}\right) \quad \text{(Eq. 3.2)}$$

where β is an empirical constant of the host lattice, ΔE is the energy difference between a populated energy level and the next lower energy level, and $\hbar\omega_{max}$ is the highest vibrational mode of the host. Er^{3+} is an ideal activator due to its relatively large ΔE compared to other lanthanide ions. With this in mind, coupling high concentration Yb^{3+} sensitizer and relatively lower concentration Er^{3+} activator doping makes a suitable ETU system for study in a BFO host. The relative concentrations are essential for the function of the ETU mechanism. High sensitizer concentration allows for sufficient absorption cross-section to maximize incident photon absorption,

while low activator concentration minimizes activator proximity which can cause cross-relaxation quenching.[90,101] This lays the groundwork for a potential lanthanide-doped (and therefore long wavelength sensitized) BFO photoactive device that uses expanded-spectrum photo-excited charge carriers for electricity or chemical reactions.[103–106] The schema for the operation of this device is that absorption of incident solar radiation of sufficient energy (green visible to UV) for conduction band excitation would be supplemented by the absorption of solar radiation of insufficient energy (green visible to IR) and subsequent internal emission/reabsorption of UC emission light now sufficient for usable charge carrier formation. It should be noted that while this is an exciting area of research as a proof-of concept, it likely has little industrial application as UC itself has low conversion efficiency and the low lanthanide doping concentrations severely limit the absorption cross-section of UC active sites.

3.2.5 Electrochemical Energy Storage

BFO has also garnered attention as an electrode material for electrochemical energy storage, motivated by its multicomponent redox chemistry, structural tunability, and the ability to leverage defect engineering to tailor its electrochemical behavior. Electrochemical capacitors, commonly referred to as supercapacitors, store charge through two distinct mechanisms: non-Faradaic electric double-layer capacitance (EDLC), which arises from electrostatic ion adsorption at the electrode-electrolyte interface, and Faradaic pseudocapacitance, which arises from rapid, reversible surface and near-surface redox reactions.[107] BFO exhibits both

contributions, though pseudocapacitance is generally dominant and is the principal source of its appreciable charge storage capability.

The pseudocapacitive behavior of BFO in alkaline and neutral aqueous electrolytes is attributed to reversible redox transitions of the Fe^{3+}/Fe^{2+} couple and partial redox activity at Bi sites, which together contribute multi-electron Faradaic reactions across the accessible potential window.[107,108] Phase-pure BFO nanoparticles have demonstrated specific capacitances in the range of ~80–260 F g^{-1} in alkaline electrolytes such as KOH and NaOH, with substantially lower performance in neutral electrolytes such as Na_2SO_4. This is attributed to differences in ion solvation energy, anion intercalation efficiency, and the accessibility of surface redox sites.[107,109] EDLC, by contrast, is primarily governed by the accessible surface area of the electrode, and consequently benefits from nanostructured BFO morphologies like nanorods, nanoflakes, and nanowires, rather than dense thin films.[110]

A persistent limitation of BFO as a supercapacitor electrode is the inherently poor electronic conductivity of the bulk perovskite, which increases equivalent series resistance and restricts rate capability. The densely packed perovskite crystal structure also impedes ion diffusion into the bulk, concentrating redox activity at the surface and limiting volumetric utilization of the material.[111] Two broad strategies have been pursued to address these constraints: morphological engineering and defect engineering through heteroatom doping. High surface area nanostructures reduce diffusion path lengths and increase the density of electrochemically active sites.[110] Aliovalent doping at either the A-site (Bi^{3+}) or B-site (Fe^{3+}) induces compensating

oxygen vacancies as a charge neutrality requirement, which simultaneously improve bulk ionic conductivity by opening diffusion pathways, enhance electronic conductivity through partial reduction of Fe^{3+} to Fe^{2+}, and activate additional Faradaic sites within the bulk of the material.[111,112] For example, aliovalent B-site doping with In^{3+} at varying concentrations has been shown to systematically improve specific capacitance, conductivity, and ion transport relative to undoped BFO, with optimal performance tied to a balance between defect density and structural disorder. Similarly, V-doped BFO nanoflake electrodes demonstrate that electrochemically induced oxygen vacancies, generated during cycling itself, can progressively improve rate capability and Li^+ diffusion coefficients.

BFO has also been investigated as an anode material for lithium-ion batteries, where charge storage proceeds through a fundamentally different conversion-alloying mechanism rather than surface pseudocapacitance.[113] The multi-electron conversion reaction in which BFO is reduced to metallic Bi and Fe nanoparticles embedded in a Li_2O matrix, followed by sequential Li-Bi alloying steps, provides a theoretical capacity far exceeding that of conventional intercalation anodes such as graphite (~372 mAh g^{-1}). Reported first-discharge capacities for BFO anodes range broadly, with optimized formulations using appropriate binders and electrolyte additives achieving ~750 mAh g^{-1} with stable cycling over 1000 cycles.[113] However, the practical limitations of this mechanism are well-established: large volume changes during conversion drive electrode delamination, the initial conversion reaction exhibits low coulombic efficiency due to irreversible solid-electrolyte interphase

(SEI) formation, and capacity degrades with cycling as Li_2O passivation layers accumulate and impede electron access to active material.[114] As with the pseudocapacitor case, compositing BFO with conductive carbon supports such as reduced graphene oxide has been shown to significantly mitigate these mechanical and transport limitations by buffering volume change and providing continuous electron pathways.

Together, these considerations motivate investigating BFO nanoparticles, particularly those produced through wet-chemical routes compatible with dopant incorporation, as electrodes in both aqueous pseudocapacitor and non-aqueous lithium-ion battery configurations, and establish defect engineering via heteroatom doping as a primary lever for improving performance in both cases.

3.3 Experimental

3.3.1 Synthesis

With each of these applications in mind, a series of pure and doped BFO thin films and powders were synthesized. BFO is a notoriously difficult compound to synthesize using wet chemical or solid-state techniques due to the volatility of Bi and the tendency to form secondary phases such as Bi_2O_3, and iron oxides. Due to a lack of access to higher precision techniques like molecular beam epitaxy, physical vapor deposition, pulsed laser deposition, etc. considerable work went into optimizing wet chemical routes to single phase pure and doped BFO. These included forming precursors from potentiostatic co-electrodeposition of bimetallic BiFe alloy, a

Bi^{3+}/Fe^{3+} Pechini polymer deposition, or a Bi^{3+}/Fe^{3+} solution drop-cast, all followed by high temperature annealing in air to form $BiFeO_3$ thin films directly on a conductive substrate. Additionally, a xerogel synthesis was done to produce BFO nanoparticles, and allow more control over dopant content.

For each thin film, fluorine doped tin oxide (FTO) was cut to the desired size and thoroughly washed with acetone, ethanol, and deionized water. It was then dried with compressed air before use.

3-electrode potentiostatic co-electrodeposition of BiFe

The electrodeposition electrolyte consisted of 14 mM $Bi(NO_3)_3 \bullet 5H_2O$, 21 mM $FeCl_2 \bullet 4H_2O$, and 100 mM $NaClO_4$ as the supporting electrolyte in N_2 purged dimethyl sulfoxide solvent. A saturate Ag/AgCl reference electrode, carbon rod counter electrode and washed FTO working electrode with approximately 1 cm^2 exposed area were placed in 30 mL of the electroplating solution polarized to -1.8 V vs. Ag/AgCl for approximately 1 min until 100 mC cm^{-2} of charge had passed. The samples were immediately removed, rinsed with ethanol, dried, and annealed in air at 600 ˚C for 3 h with a ramp rate of 6.7 ˚C min^{-1} in a tube furnace.

Pechini Polymer Deposition

A solution of 1 M $Fe(NO_3)_3 \bullet 9H_2O$, 1.25 M $Bi(NO_3)_3 \bullet 5H_2O$, and 2.5 M citric acid in ethylene glycol was heated with stirring at 70 ˚C for 10 min to induce polymerization. Bi^{3+} is present in higher concentration due to its volatility and tendency to vaporize during the high temperature annealing steps. The citric acid

polymer chelates the metal ions along the polymer backbone sterically fixing the ions before forming the oxide. The solution was then allowed to cool to room temperature before being deposited via spin coating. 50 μL of solution was placed in the center of cleaned FTO and spun at 500 rpm for 30 s to evenly disperse the solution, then accelerated to 7000 rpm for 1 min to remove excess and thin the deposited layer. The sample was then dried in an oven at 60 ˚C for 20 min before annealing in air at 300 ˚C for 30 minutes in a preheated muffle oven to burn off the organic residue. Al previous steps were completed again to add the desired number of layers to the surface. Once the desired layers were deposited, the sample was then annealed in air at 600 ˚C for 3 h with a ramp rate of 6.7 ˚C min^{-1} in a tube furnace.

Solution Drop-Cast

Precursor solutions for each ion were prepared at 50 mM concentration in dimethyl formamide solvent. $Bi(NO_3)_3 \cdot 5H_2O$, $Fe(NO_3)_3 \cdot 9H_2O$, and $SnCl_4 \cdot 5H_2O$ solutions were combined in the desired molar ratio with polyethylene glycol 200 to form the drop-cast solution. In the case of pristine BFO, a ratio of 2:2:1 Bi:Fe:PEG-200 and in the case of 1% Sn doped BFO, a ratio of 100:99:1:50 Bi:Fe:Sn:PEG-200 was used. 30 μL of the drop-cast solution was dropped onto a 1 x 2 cm^2 piece of clean FTO before drying in an oven at 115 ˚C for 50 min. The sample was then annealed at 300 ˚C for 30 minutes in a preheated muffle oven to burn off the organic residue. The sample was then annealed in air at 600 ˚C for 3 h with a ramp rate of 6.7 ˚C min^{-1} in a tube furnace.

Xerogel Nanoparticles

The xerogel precursor solution was made by adding 0.01 mol $Bi(NO_3)_3 \cdot 5H_2O$, 0.01 mol $Fe(NO_3)_3 \cdot 9H_2O$, and 0.02 mol tartaric acid to 2 N HNO_3. A stoichiometric amount of dopant precursor could also be added when making doped samples. $SnCl_4 \cdot 5H_2O$, $GeCl_4$, $Yb(CH_3CO_2)_3 \cdot 4H_2O$, and $Er(CH_3CO_2)_3 \cdot 4H_2O$ were used as dopant precursors across different studies. The solution was stirred at room temperature for 15 h to ensure chelation by tartaric acid. The solution was then heated at 100 ˚C for approximately 10 h until most of the water evaporated leaving behind a highly porous xerogel. This xerogel was dried at 120 ˚C overnight before ground to a fine powder and annealed in air at 600 ˚C for 3 h with a ramp rate of 3 ˚C min^{-1} in a tube furnace.

3.3.2 Characterization

Powder X-Ray Diffraction (XRD)

Thin film and powder samples were analyzed using a Rigaku SmartLab high-resolution powder X-ray diffractometer with a Cu K_α X-ray source in parallel beam mode. Thin film samples were placed on the flat sample plate, and the Z-axis was adjusted based on the FTO glass substrate thickness of 2.2 mm. Powder samples were finely ground with a mortar and pestle and spread in a depressed glass slide sample holder. Scans were run from 2θ angles of 20˚- 60˚ with 0.02˚ steps at a rate of 1˚ min^{-1}. The resulting scans were generally background corrected and indexed using entries from the Crystallography Open Database (COD).

Photoluminescence

BFO samples were analyzed using an Agilent Cary Eclipse Fluorescence Spectrophotometer with an excitation wavelength of 350 nm. Thin films and powders were deposited on a quartz glass substrate transparent to UV light and placed in a reflectance chamber setup.

Photoelectrochemical Water Splitting

Thin film samples deposited on FTO were generally ready for photoelectrochemical measurements and were used directly as the working electrode in the cell. Powder BFO samples had to be deposited on a conductive substrate (FTO) via airbrushing. For this, an ink suspension of 5 mg mL^{-1} in ethanol was prepared and sprayed onto a 1 x 1 cm^2 exposed area of a 1 x 1.5 cm^2 piece of clean FTO. A two-part, alkaline resistant epoxy was put around the edges of the sample to ensure that only the BFO surface was in contact with the electrolyte in the cell. After drying, the electrode was placed in a 3-cell quartz glass separated cell with a saturated Ag/AgCl reference electrode, carbon rod counter electrode, and 1 M NaOH electrolyte with pH 13.6. J-V and i-t measurements were recorded using a CHI 660D electrochemical workstation (CH instruments Inc.) with a Newport Model 69907 solar simulator fitted with an AM 1.5G filter on the 150 W Xe lamp white light source. The cell was placed so that the electrode surface was in line with 100 mW cm^{-2} incident power density reading.

Energy Storage

BFO powders were used in both aqueous and nonaqueous energy storage electrodes. Both used a slurry of 70 wt.% BFO powder, 20 wt.% acetylene black, 10 wt.% polyvinylidene fluoride binder in N-methyl-2-pyrrolidone solvent spread at a thickness of 200 μm onto 400 μm thick carbon paper. The electrodes were then dried in a vacuum oven for 24 h at 60 ˚C. In the case of nonaqueous Li-ion systems, the electrode was transferred to an Ar containing glove box and used in a 2-electrode beaker cell with a Li foil counter/reference electrode and 1 M $LiPF_6$ in 1:1 ethylene carbonate:diethyl carbonate electrolyte. The electrode's performance as an aqueous supercapacitor was carried out in a 3-electrode beaker cell with an Ag/AgCl reference electrode, carbon rod counter electrode, and either 3 M KOH or 1 M Na_2SO_4 electrolyte. All electrochemical measurements, aqueous and nonaqueous, were taken using a SP-300 BioLogic electrochemical workstation.

Ferroelectricity

BFO powder samples were pressed into circular pellets of 1 cm diameter and approximately 2 mm thickness by weighing out 300 mg of powder and placing into a high-precision steel pellet die. The powder was pressed to a pressure of 40 MPa for 5 min in a benchtop hydraulic press before slowly releasing the pressure over 2 min. The resulting pellet was mechanically robust without further treatment. Both sides of the pellet were painted with Ag paint to ensure good contact and placed into a Swagelok cell, pressed between the two steel piston contacts. Ferroelectric

measurements were carried out using a CHI 660D electrochemical workstation (CH instruments Inc.).

3.4 Results and Discussion

The primary goal of this work is to explore different wet chemical synthesis techniques to produce pure and doped BFO for a variety of commonly studied applications as well as the novel application as a photon upconversion host material. In all cases, it is well documented that the high volatility of Bi metal and Bi precursors makes high temperature synthesis notably more complicated as vaporization must be accounted for. This often requires rigorous optimization for each synthesis, to account for the rate of vaporization of Bi depending on the phase it is in and the heating profile of the annealing step. Furthermore, each synthesis was differently suited for introducing dopant ions to the system. Generally, with each metal introduced to the system, the complexity of the synthesis increases exponentially as the chemical potentials, enthalpies of formation, etc. change and the possibilities of secondary phases arise.

Each application demands different forms and morphology, depending on how the material is utilized and tested. In the case of optical applications like photoelectrochemical water splitting, it is important that the BFO is deposited directly on a transparent, conductive substrate with good adhesion to minimize internal resistance of the photoelectrode. In energy storage applications, it is often best to have nanostructured material to increase surface area. As such, four approaches were taken

to produce pure and doped BFO. Three direct substrate-deposited and a loose nanoparticle powder synthesis were developed.

The first direct deposit synthesis was a potentiostatic co-electrodeposition of metallic Bi and Fe onto FTO substrate followed by air annealing to form BFO. This synthesis was limited to pure BFO as a baseline and to avoid the difficulty of simultaneously depositing three metals in ideal ratios. As deposited samples appeared black in color and were characterized using energy dispersive X-ray spectroscopy (EDS) and scanning electron microscopy (SEM) to determine the atomic ratio between deposited Bi and Fe, and the morphology of metallic deposition (Figure 3.6a). The deposition was determined to be difficult to reproduce, with Bi:Fe ratios differing among trials. Atomic percentages calculated from EDS spectra over 10 x 10 μm areas show vary significantly despite the same electrodeposition conditions (Table 3.1). This is likely due to the nucleation kinetics of each metal competing for the substrate surface. The samples are further treated by air annealing to convert deposited metallic BiFe to BFO. XRD of the deposited metallic precursor and annealed final samples show inconsistent results demonstrating that this approach is not ideal for pure phase samples. In only one case was mostly pure phase BFO deposited on FTO (Figure 3.6b).

Table 3.1 Representative atomic percentages of Bi and Fe co-electrodeposited on FTO calculated from EDS spectra collected over 10 x 10 μm area.

Trial	Bi (at.%)	Fe (at.%)
1	76.2 ± 0.2	23.8 ± 0.2
2	17.0 ± 0.2	83.0 ± 0.2
3	88.7 ± 0.2	11.3 ± 0.2
4	45.5 ± 0.2	54.5 ± 0.2
5	48.9 ± 0.2	51.9 ± 0.2
6	67.0 ± 0.2	33.0 ± 0.2

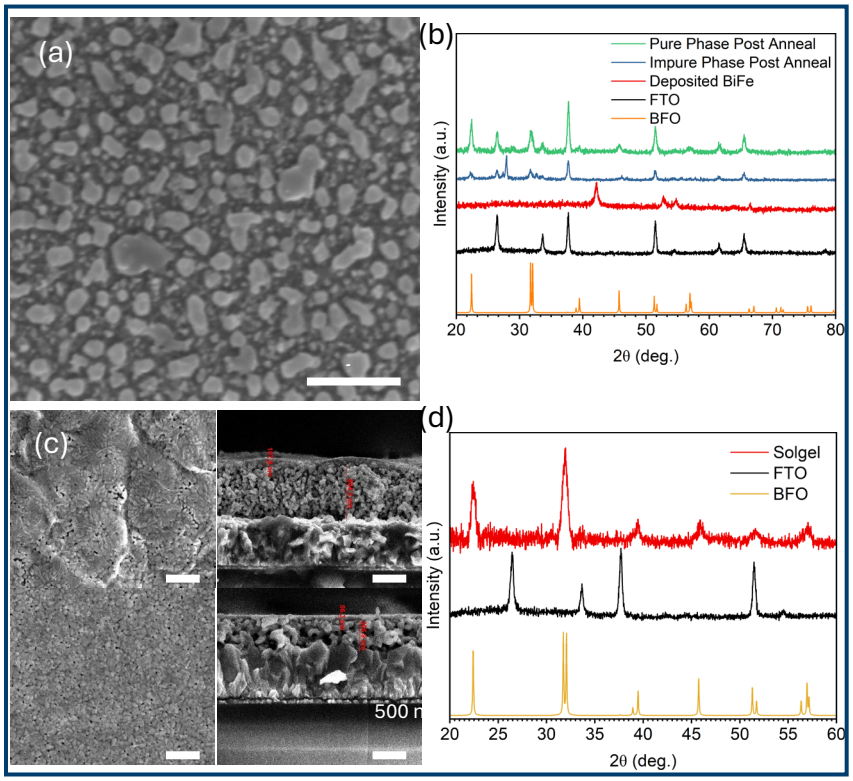

Figure 3.6 (a) SEM image of deposited BiFe on FTO. (b) XRD patterns depicting representative samples of co-electrodeposited deposited BiFe and pure and impure

final products. (c) SEM images of solgel deposited BFO on FTO glass. Top is 3 deposited layers, and bottom is 1 deposited layer. Left are top-down view of electrode surface and right are cross-sectional view. (d) XRD patterns of solgel deposited electrode. BFO reference COD 2102909.

The second direct deposit synthesis was a Pechini solgel, spin coated onto the FTO substrate. While this also sometimes resulted in secondary phases, namely Bi_2O_3, it also allowed for a much more uniform deposition and surface, as well as a tunable coating thickness. A single layer of solgel deposition resulted in a porous channeled structure ranging from 250 – 300 nm with a thin overlayer or more tightly packed particles with smaller channels ranging from 40 – 60 nm thickness (Figure 3.6c). This result scaled approximately linearly with the number of layers deposited. Secondary phases were often observed as very long, thin nanowires approximately 200 nm long, and less than 10 nm in diameter. Importantly, dopants were able to be added to the solgel, making doped BFO samples possible using this technique. Despite unwanted secondary phases forming in some cases, this proved to be a reliable and tunable deposition technique for photoelectrochemical and upconversion applications.

The third direct deposit synthesis was a viscous solution drop cast. This is a simple method, involving little chemical workup of the precursors in order to form pure and doped BFO films. A viscous solution containing metal nitrates was deposited on the FTO surface, then dried to leave atomically mixed precursors on the surface. The sample was then air annealed to form the pure and doped BFO.

Using linear sweep voltammetry under ambient and solar simulation conditions of pure and 1.0% Sn doped BFO as a baseline comparison, it can be seen that the solgel deposited samples have significantly higher current density compared to the solution drop cast samples (Figure 3.7). Solgel samples have current response nearly 1000 times more than their solution drop cast counterpart. This is indicative of higher inherent conductivity of the solgel deposited BFO, which is an important performance indicator for most applications. Both samples show a similar improvement in conductivity upon doping with 1.0% Sn, reaching approximately 10 times the current response over the pure BFO sample at 1.6 V vs. RHE. Interestingly, both showed minimal photocurrent upon illumination, but solution drop cast samples had a larger relative photocurrent. Despite having an optimal band gap for photoelectrochemical water splitting, BFO is limited by poor charge carrier separation and conductivity, as well as suboptimal reactive sites for the generally complicated oxygen evolution reaction that takes place on its surface when used as a photoanode. Addressing these issues is the main motivation for studying BFO as a photoanode in these systems and rarely yields photocurrents higher than the $\mu A\ cm^{-2}$ scale. Only highly engineered, epitaxial films have been demonstrated to exceed this[115,116]. Still this comparison demonstrates that the fabrication of the electrodes is an essential first step in addressing these challenges.

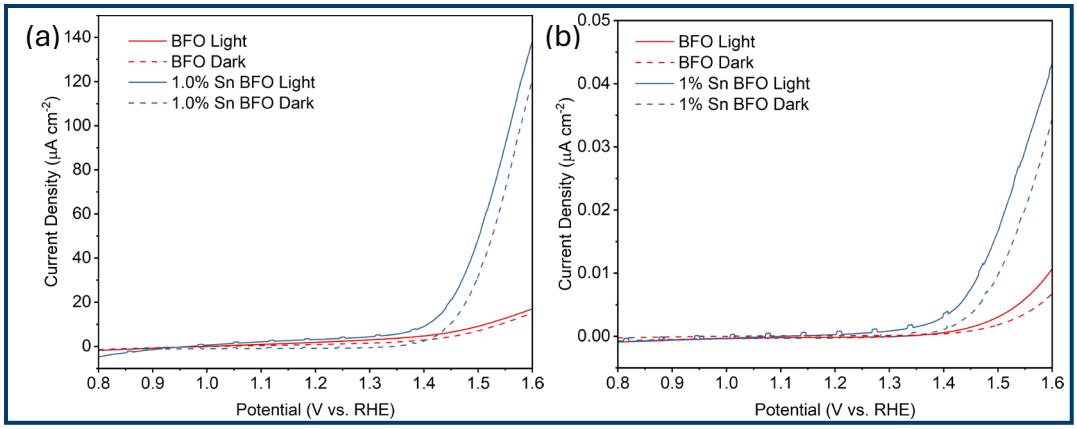

Figure 3.7 Linear sweep voltammetry plots under dark and solar simulator illumination of solgel deposited (a) and solution drop cast (b) pure and 1.0% Sn doped BFO samples.

The fourth synthesis yields nanoparticles as a loose powder and is therefore more versatile than the direct substrate deposited samples discussed above. It is for this reason that the majority of synthesis optimization and characterization was done on these samples. The synthesis was a modified xerogel synthesis in which metal nitrate or acetate precursors are dissolved in solution and chelated by a polymerized organic acid. This is a highly tunable synthesis that allows for including multiple dopants as in the case of targeting lanthanide ETU mechanisms. This also allows for studying and tuning another important synthesis parameter: annealing temperature. This was generally limited by the melting point of the glass and stability of the FTO coating in direct substrate deposition techniques. The xerogel nanoparticle synthesis reproducibly produced pure and doped BFO with diameter approximately 50 nm and no significant secondary phase formation according to XRD (Figure 3.8a).

With photon upconversion and photoelectrochemical applications in mind, the photoluminescence spectra of pure, 1.0% Sn, and 20% Yb/2% Er doped BFO were collected. This provides some insight into the band gap and presence of significant defect states or recombination pathways that can hinder the performance of the material (Figure 3.8b). Both pure and 1.0% Sn doped BFO show very similar photoluminescence profiles with the primary emission at approximately 446 nm (2.78 eV) corresponding to the band gap of the material[117]. The next largest emission at 482 nm and the smaller shoulder extending out to 560 nm usually indicate near-band-edge radiative relaxation and defect-related transitions[118]. These are most commonly associated with significant oxygen vacancy or Fe defect concentration. Of most interest is the complete quenching of the primary band emission in the Yb/Er codoped sample prepared for ETU. The reason for this is not entirely clear and requires more study, but it could be due to the high doping concentration of lanthanide heteroatoms, clearly significantly changing the crystal structure and more appropriately considered as a solid solution or different phase entirely. Another possibility is severe disruption to the band structure of the material, possibly increasing the band gap to greater than 350 nm excitation wavelength. In order to probe the upconversion capability of these materials it is necessary to collect emission spectra at wavelengths shorter than the excitation wavelength. This likely requires a custom experimental design with an infrared or near-infrared excitation laser and detector scanning at shorter wavelengths. This was not easily accessible and remains

an area of important need for the full characterization of lanthanide doped BFO for photon upconversion.

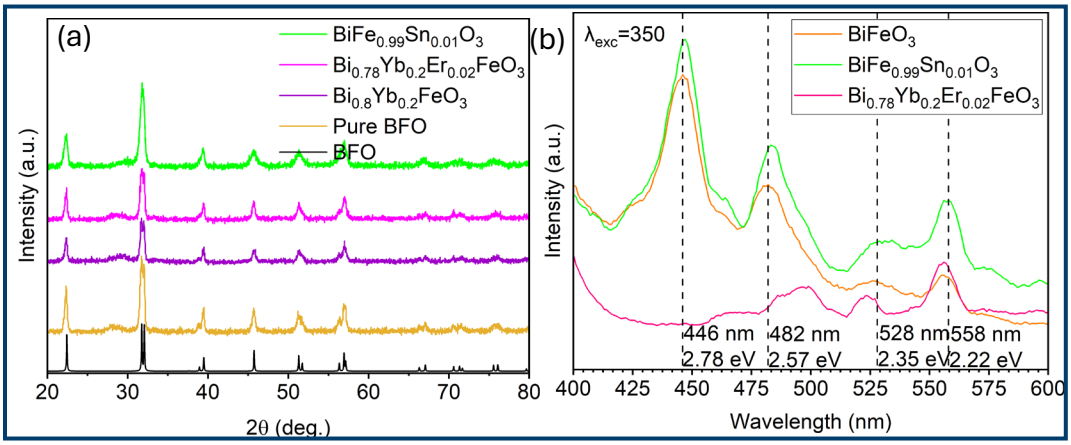

Figure 3.8 (a) XRD patterns of representative samples of pure and doped BFO xerogel nanoparticle samples. (b) Photoluminescence spectra of pure and doped BFO.

Xerogel nanoparticles were investigated as both aqueous and non-aqueous energy storage materials by incorporating into a slurry and cast onto a carbon paper conductive substrate. The resulting electrodes were tested in 1 M Na_2SO_4 and 3 M KOH to study possible differences in charge storage mechanisms in different media. Both electrolyte systems display Faradaic redox pseudocapacitance rather than simple EDLC (Figure 3.9). A detailed understanding of the charge storage mechanism of BFO in aqueous systems is still not agreed upon but the resolved peaks likely involve redox reactions $Bi^{3+}/Bi^{<3+}$, Fe^{3+}/Fe^{2+}.[119,120] Full reduction to Fe^0 or Bi^0 have also been proposed but are generally deep reductions associated with battery-like reactions and require more negative potentials.[108,121] Neutral 1 M Na_2SO_4 electrolyte has a similar profile, but there is significant peak broadening and separation

especially at high scan rate indicating slow ion diffusion. Galvanostatic charge-discharge curves show similar pseudocapacitive behavior with battery-like plateaus forming as surface redox reactions take place. Electrical impedance spectroscopy was also performed to compare the electrolyte systems but there were no major differences as both electrolyte systems provided sufficient ionic conductivity so as to not limit the performance of the electrodes.

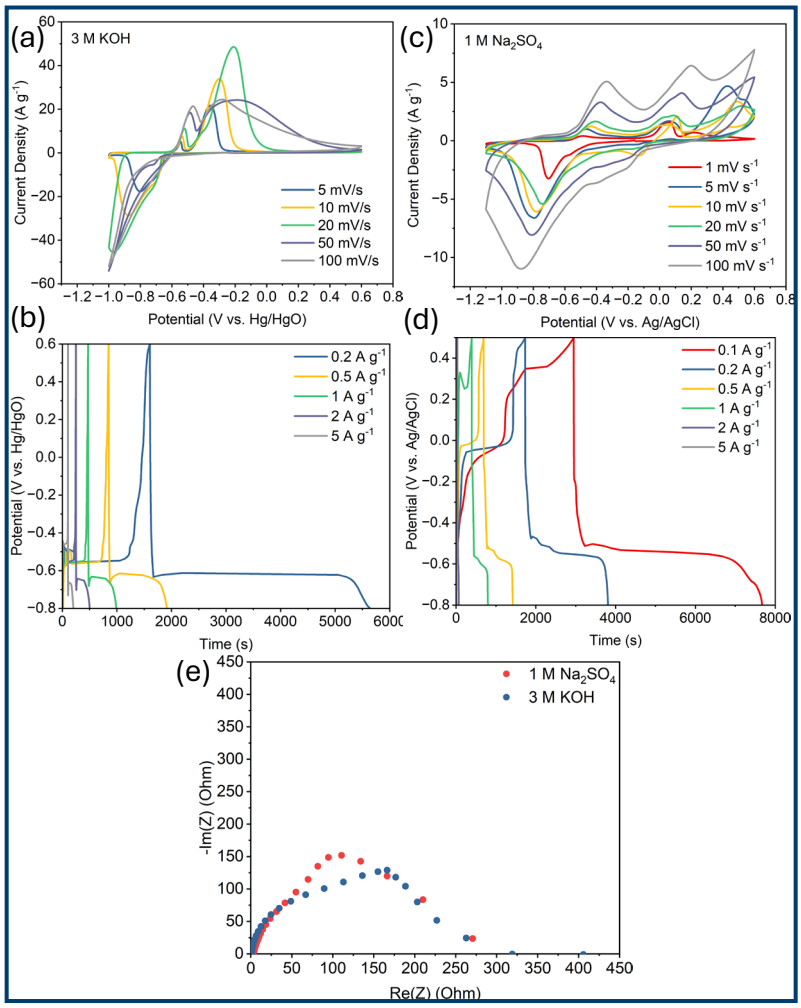

Figure 3.9 Cyclic voltammograms, galvanostatic charge-discharge curves, Nyquist plots of pure BFO slurry electrodes in 3 M KOH (a,b,e), 1 M Na_2SO_4 (c,d,e).

The same electrodes were also applied to a lithium-ion battery system. In this case, the charge storage mechanism is better characterized and follows a conversion mechanism[113]:

R3	$BiFeO_3 + 6Li^+ + 6e^- \rightarrow Bi + Fe + 3Li_2O$	E = 1.33 V
R2	$Bi + Li^+ + e^- \rightarrow LiBi$	E = 0.75 V
R1	$LiBi + 2Li^+ + 2e^- \rightarrow Li_3Bi$	E = 0.59 V
O1	$Li_3Bi - 3Li^+ - 3e^- \rightarrow Bi$	E = 0.95 V
O2	$2Bi - 6e^- + 3Li_2O \rightarrow Bi_2O_3 + 6Li^+$	E = 1.84 V
O3	$2Fe - 6e^- + 3Li_2O \rightarrow Fe_2O_3 + 6Li^+$	E = 2.32 V

This conversion reaction consists of a series of many electron reactions allowing for high capacity but is limited in its reversibility. Upon Li^+ intercalation during discharging, the initial BFO electrode will reduce to metallic Bi, Fe, and various alloys. The subsequent deintercalation during charging will oxidize the metals to their representative oxides. This is an ideal reaction series, and it is possible that more complicated mixed oxides will form as well. In general, this is a major limitation of the system as it fundamentally changes after the first several cycles eventually becoming a composite Bi_2O_3 and Fe_2O_3 electrode. Cyclic voltammetry of the pure BFO slurry electrodes in 1 M $LiPF_6$ in 1:1 ethylene carbonate:diethyl carbonate versus a Li foil counter electrode adhere to the above mechanism (Figure 3.10). Capacity is calculated from the galvanostatic discharge curve and plotted as a function of cycle number and current density. The capacity fades quickly with each cycle as the intercalation/conversion reaction is not completely reversible.

The coulombic efficiency starts at approximately 70% and begins to climb as the system stabilizes, and the SEI forms. As expected with an intercalation/conversion reaction mechanism, it is kinetically limited and capacity drops off severely as current density increases, as well as a degradation of the reversibility due to phase evolution.[114] All are serious limitations of BFO in lithium ion battery systems. The potential for very large capacity from the conversion reaction mechanism might not ever been meaningfully utilized in commercial applications.

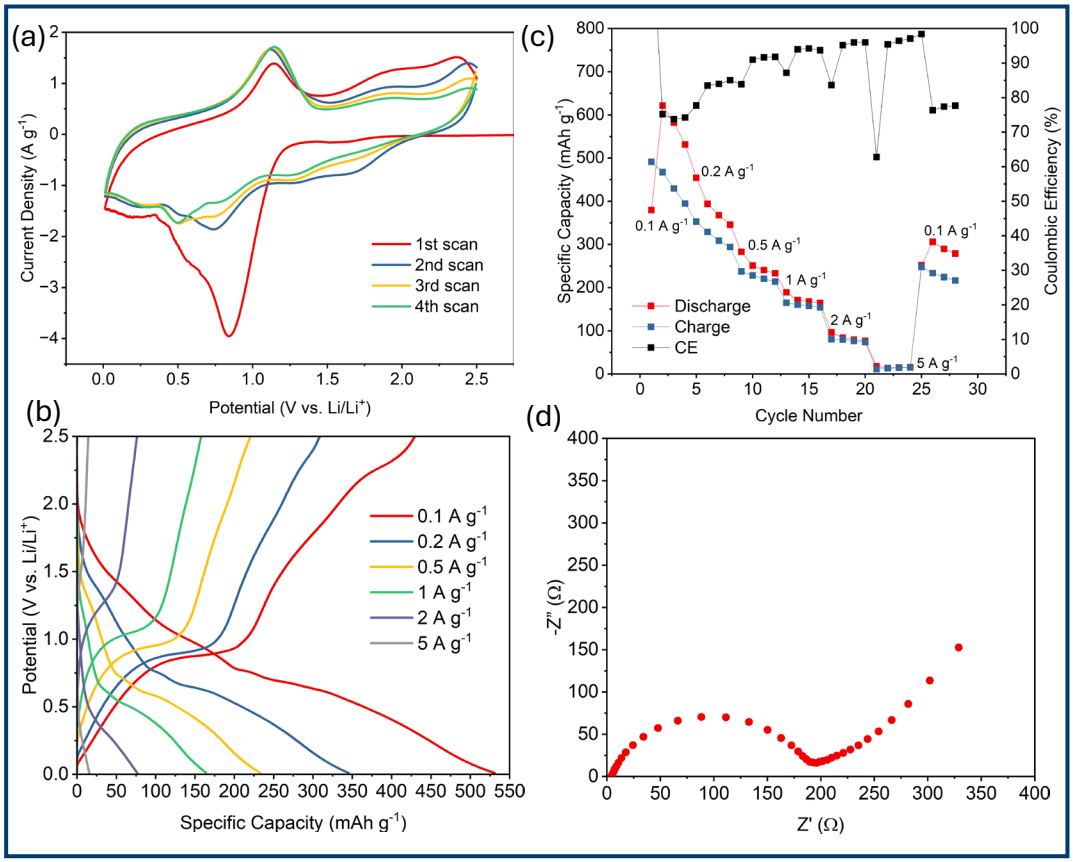

Figure 3.10 (a) Cyclic voltammogram of the first 4 scans of pure BFO slurry electrode in lithium-ion battery system. (b) Galvanostatic charge-discharge curves as

a function of specific capacity. (c) Rate capability and coulombic efficiency. (d) Nyquist plot of electrical impedance spectrum before cycling.

The last application of BFO considered herein depends on the most commonly studied property of BFO and the reason that it is such a well-known material. The multiferroic properties, and specifically ferroelectricity of BFO are of major interest in many fields but especially in microelectronics. In this case, xerogel nanoparticles synthesized via a simple wet chemical route were tested for ferroelectric behavior to see if this synthesis is capable of producing a viable multiferroic. Historically, the multiferroic properties of BFO are only emergent in highly ordered and carefully grown thin films and crystals, and the properties are often overcome by competing crystallographies in nanocrystalline systems. The xerogel nanoparticles were pressed into solid pellets and tested for ferroelectric response. This usually requires highly sensitive experiments and/or powerful, high voltage physical property measurement systems. Here, a simple potentiostat is used to collect electrical impedance data and calculate the dielectric constant of the material (Figure 3.11). The dielectric constant is calculated with the following equations, first calculating capacitance, C, then dielectric constant ε_r:

$$C = \frac{1}{2}\pi f Z \qquad \text{(Eq. 3.3)}$$

$$\varepsilon_r = \frac{Cd}{\varepsilon_0 A} \qquad \text{(Eq. 3.4)}$$

where f is the frequency, Z is the impedance, d is the pellet thickness, ε_0 is vacuum permittivity constant, and A is the pellet area.

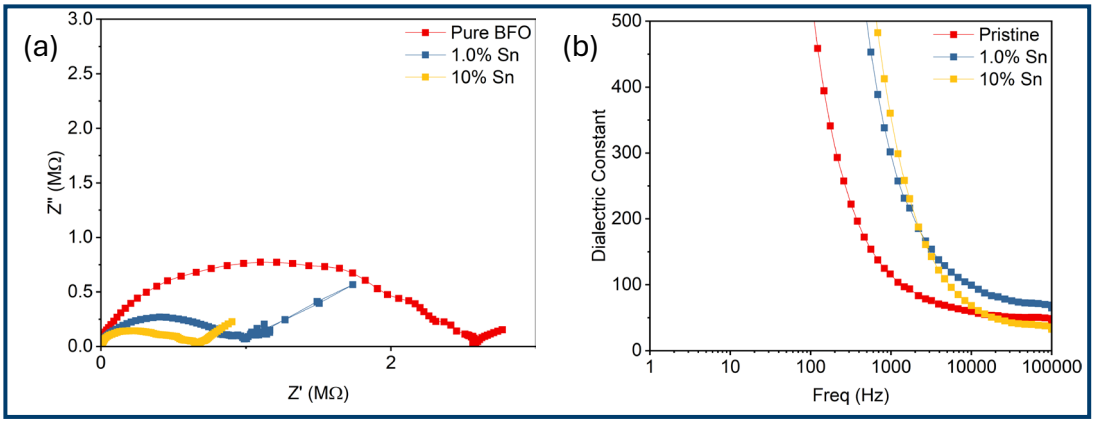

Figure 3.11 (a) Nyquist plot of electrical impedance spectrum. (b) Dielectric constant calculated from electrical impedance data.

Nyquist plots for all samples exhibit depressed semicircular arcs in the MΩ regime, consistent with resistive-capacitive responses from coupled grain interior and grain boundary contributions characteristic of polycrystalline ceramic oxides. The depression of the arcs below the real axis indicates a distribution of relaxation times arising from grain size and microstructural inhomogeneity and is more accurately modeled using constant phase elements rather than ideal capacitors in an equivalent circuit description. For the 1.0% Sn sample, partial resolution of two overlapping arcs suggests that grain and grain boundary relaxation processes possess sufficiently distinct time constants to be deconvoluted through equivalent circuit fitting, whereas in pure BFO these contributions are superimposed into a single broad arc. EIS reveals a systematic reduction in bulk resistance with increasing Sn content, from

approximately 2.8 MΩ in pure BFO to 0.8 MΩ at 10% Sn, consistent with enhanced electronic conductivity through Sn-mediated charge carrier introduction. This trend is corroborated by the dielectric constant versus frequency data, in which increasing Sn content shifts the space charge relaxation onset to higher frequencies, reflecting the reduced resistivity of the grain boundary network and its diminished ability to impede charge carrier accumulation at low frequencies. The low-frequency dielectric inflation observed across all samples is therefore attributed to Maxwell-Wagner interfacial polarization at grain boundaries rather than intrinsic ferroelectric permittivity enhancement[122]. The conduction mechanism cannot be definitively assigned without complementary Hall effect measurements, but the impedance and dielectric data are consistent with small polaron hopping mediated by Fe^{2+}/Fe^{3+} pairs, as commonly reported in donor-doped BFO ceramics[123].

3.5 Conclusion

Four wet-chemical synthesis routes: potentiostatic co-electrodeposition, Pechini solgel deposition, solution drop-casting, and xerogel nanoparticle, were developed and evaluated for the production of pure and doped $BiFeO_3$ thin films and powders. Each route presents distinct tradeoffs between phase purity, morphological control, substrate compatibility, and flexibility for dopant incorporation. Co-electrodeposition produced only occasional single-phase BFO and suffered from poor reproducibility in Bi:Fe stoichiometry, making it unsuitable as a general-purpose BFO synthesis route without significant further optimization. Pechini solgel deposition provided the most controllable thin film synthesis, producing morphologically

uniform, tunable-thickness coatings with acceptable phase purity, though secondary phase formation remains a persistent challenge. The solution drop cast method, while simple, produced films with substantially lower conductivity than solgel counterparts, as demonstrated by linear sweep voltammetry. The xerogel synthesis proved most versatile, reproducibly yielding phase-pure nanoparticles of approximately 50 nm diameter and accommodating a broad range of dopant species including transition metals and lanthanides, making it the primary platform for the multi-application characterization presented here.

Photoelectrochemical measurements confirm that both pure and Sn-doped BFO exhibit the characteristic limitations of this material class: photocurrents confined to the μA cm^{-2} scale and minimal photovoltaic response under AM 1.5G illumination, underscoring that synthesis route and dopant strategy alone are insufficient to overcome poor charge separation and surface reaction kinetics without further interface engineering. The aqueous pseudocapacitance measurements in both KOH and Na_2SO_4 confirm the Faradaic character of BFO charge storage, with the slower ion diffusion in neutral Na_2SO_4 relative to alkaline KOH reflected in the increased peak broadening and separation at elevated scan rates. In the lithium-ion battery system, BFO follows the expected multi-step conversion mechanism, and the rapid capacity fade and low initial coulombic efficiency (~70%) observed here are consistent with the known limitations of conversion-type anodes, a promising theoretical energy density tempered by poor reversibility. Dielectric characterization of Sn-doped pellets reveals systematic resistance reduction with increasing Sn content

and low-frequency dielectric inflation attributable to Maxwell-Wagner interfacial polarization rather than intrinsic ferroelectric permittivity, consistent with small polaron hopping conduction mediated by Fe^{2+}/Fe^{3+} pairs.

The photoluminescence data for Yb/Er co-doped BFO represent the most speculative results presented here and are offered explicitly as motivation for future investigation rather than definitive characterization. The complete quenching of the near-band-edge emission in the heavily lanthanide-doped sample indicates substantial perturbation of the BFO electronic structure at the dopant concentrations required for an ETU system, the mechanistic origin of which, bandgap widening, phase change, or severe disorder, remains unresolved. Confirming photon upconversion activity in lanthanide-doped BFO will require near-infrared or infrared excitation and anti-Stokes emission detection, instrumentation not available for this study. Together, the results presented in this chapter establish wet-chemical BFO synthesis as a tractable, if non-trivial, foundation for continued investigation, and identify the specific instrumentation, contact quality, and doping regime challenges that must be addressed in subsequent work.

3.6 References

1. Radamson, H. H.; Miao, Y.; et al. *Nanomaterials (Basel)* **2024**, *14* (10), 837.
2. Shalf, J. *Philos Trans A Math Phys Eng Sci* **2020**, *378* (2166), 20190061.
3. Etiemble, D. arXiv:2206.03201v1 [cs.ET].
4. Ergun, S.; Dik, A.; et al. *Sustainability* **2025**, *17* (3), 1311.
5. Prol, J. L.; Schill, W.-P. *Annual Review of Resource Economics* **2021**, *13*, 443–467.
6. Buehner, C.; Magableh, S. K.; et al. In *2025 IEEE Power & Energy Society General Meeting (PESGM)*; **2025**; 1–5.
7. Incorvia, J. A. C.; Xiao, T. P.; et al. *Nat Rev Electr Eng* **2024**, *1* (11), 700–713.
8. Dong, S.; Xiang, H.; et al. *Natl Sci Rev* **2019**, *6* (4), 629–641.
9. Chu, Y.-H.; Martin, L. W.; et al. *Materials Today* **2007**, *10* (10), 16–23.
10. Liu, Y.; Wang, Y.; et al. *Progress in Materials Science* **2022**, *127*, 100943.
11. Li, X.; Singh, H.; et al. *Nano Lett* **2023**, *23* (15), 6845–6851.
12. *Global Energy Review 2025 – Analysis*. IEA.
13. *Executive summary – Electricity 2025 – Analysis*. IEA.
14. Xi, Z.; Liu, M. *npj Mater. Sustain.* **2025**, *3* (1), 18.
15. Cheng, C.; Zhang, W.; et al. *Energy Science & Engineering* **2022**, *10* (4), 1526–1543.
16. Abdul Nasir, J.; Munir, A.; et al. *Advanced Materials* **2021**, *33* (52), 2105195.
17. Zhao, Y.; Niu, Z.; et al. *Electrochem. Energy Rev.* **2023**, *6* (1), 14.
18. Wang, G.; Wang, H.; et al. *Nano Lett.* **2011**, *11* (7), 3026–3033.

19. Tamirat, A. G.; Rick, J.; et al. *Nanoscale Horiz.* **2016**, *1* (4), 243–267.

20. Sivula, K.; Le Formal, F.; et al. *ChemSusChem* **2011**, *4* (4), 432–449.

21. *DOE Invests More Than $9 Million To Advance Clean Hydrogen Projects*. netl.doe.gov.

22. *DOE Hydrogen Program Plan.* hydrogen.energy.gov

23. Bullock, M.; More, *Basic Energy Sciences Roundtable* **2021**, 1834317.

24. Zhu, Y.; Raimi, D.; et al. *Resources for the Future* **2025**, 25-07 .

25. Wang, J.; Neaton, J. B.; et al. *Science* **2003**, *299* (5613), 1719–1722.

26. Béa, H.; Bibes, M.; et al. *Appl. Phys. Lett.* **2005**, *87* (7), 072508.

27. Xu, J.-P.; Zhang, R.-J.; et al. *Nanoscale Res Lett* **2014**, *9* (1), 188.

28. Kartavtseva, M. S.; Gorbenko, O. Yu.; et al. *Surface and Coatings Technology* **2007**, *201* (22), 9149–9153.

29. Micard, Q.; Condorelli, G. G.; et al. *Nanomaterials* **2020**, *10* (4), 630.

30. Brown, C.; Harris-Lee, T. R.; et al. *European Journal of Inorganic Chemistry* **2025**, *28* (25), e202500333.

31. Acharya, M.; Joshi, C. R.; et al. *Chem. Mater.* **2024**, *36* (16), 7633–7646.

32. Somrani, N.; Maaloul, A.; et al. *J Mater Sci: Mater Electron* **2015**, *26* (5), 3316–3323.

33. Cha, J.; Ahn, J.; et al. *Journal of the Korean Physical Society* **2009**, *54* (9), 844–848.

34. Jian, S.-R.; Chang, H.-W.; et al. *Nanoscale Res Lett* **2013**, *8* (1), 297.

35. Jiang, Z.-Z.; Guan, Z.; et al. *Materials Characterization* **2017**, *131*, 217–223.

36. Ihlefeld, J. F.; Tian, W.; et al. *IEEE Transactions on Ultrasonics, Ferroelectrics, and Frequency Control* **2009**, *56* (8), 1528–1533.

37. Cantrell, S. R.; Miracle, J. T.; et al. *Materials* **2025**, *18* (9), 2022.

38. Gebhardt, J.; Rappe, A. M. *Phys. Rev. B* **2018**, *98* (12), 125202.

39. Mohan, M.; Shetti, N. P.; et al. *Journal of Power Sources* **2023**, *574*, 233166.

40. Jha, S. K.; Priyadarshi, P. K. *International Journal of Engineering and Science Invention* **2024**, *13* (10), 40–44.

41. Li, C.; Soh, K. C. K.; et al. *Journal of Alloys and Compounds* **2004**, *372* (1), 40–48.

42. Priya, A. S.; Henry, J.; et al. *Ceramics International* **2025**, *51* (20, Part A), 29877–29908.

43. Palewicz, A.; Przeniosło, R.; et al. *Acta Cryst B* **2007**, *63* (4), 537–544.

44. Doig, K. I.; Aguesse, F.; et al. *Phys. Rev. B* **2013**, *88* (9), 094425.

45. Royen, P.; Swars, K. *Angewandte Chemie* **1957**, *69* (24), 779–779.

46. Teague, J. R.; Gerson, R.; et al. *Solid State Communications* **1970**, *8* (13), 1073–1074.

47. Carranza-Celis, D.; Cardona-Rodríguez, A.; et al. *Sci Rep* **2019**, *9* (1), 3182.

48. Cheng, Z. X.; Li, A. H.; et al. *J. Appl. Phys.* **2008**, *103* (7), 07E507.

49. Spaldin, N. A.; Fiebig, M. *Science* **2005**, *309* (5733), 391–392.

50. Hu, A.-Y.; Wang, H.-Y. *J. Appl. Phys.* **2014**, *116* (19), 193903.

51. Hill, N. A. *J. Phys. Chem. B* **2000**, *104* (29), 6694–6709.

52. Cui, Y. F.; Zhao, Y. G.; et al. *Appl. Phys. Lett.* **2010**, *97* (22), 222904.

53. Ahmed, S.; Barik, S. K.; et al. *Appl. Phys. A* **2019**, *125* (5), 303.

54. Calzada, M. L.; Bretos, I.; et al. *ACS Appl. Energy Mater.* **2025**, *8* (5), 2845–2868.

55. Sagar, E.; Mahesh, R.; et al. *Journal of Physics and Chemistry of Solids* **2017**, *110*, 316–326.

56. Catalan, G.; Scott, J. F. *Advanced Materials* **2009**, *21* (24), 2463–2485.

57. Yang, C.-H.; Kan, D.; et al. *Phys. Chem. Chem. Phys.* **2012**, *14* (46), 15953–15962.

58. Ali, A.; Afrin, S.; et al. *Journal of Environmental Management* **2025**, *391*, 126512.

59. Mocherla, P. S. V.; Karthik, C.; et al. *Appl. Phys. Lett.* **2013**, *103* (2), 022910.

60. Sharma, S.; Kumar, M. *Materials Today: Proceedings* **2020**, *28*, 168–171.

61. Benyoussef, M.; Saitzek, S.; et al. *Catalysts* **2022**, *12* (2), 215.

62. Ihlefeld, J. F.; Podraza, N. J.; et al. *Appl. Phys. Lett.* **2008**, *92* (14), 142908.

63. Cantrell, S. R.; Miracle, J. T.; et al. *Materials (Basel)* **2025**, *18* (9), 2022.

64. Sando, D.; Carrétéro, C.; et al. .

65. Seo, D.; Grieder, A.; et al. *J. Mater. Chem. A* **2024**, *12* (31), 20437–20448.

66. Mallek-Zouari, I.; Kaddar, Y.; et al. *Int J Mol Sci* **2025**, *26* (10), 4671.

67. Lv, J.; Ning, H. *Materials (Basel)* **2024**, *17* (9), 2072.

68. Sun, Z.; Wei, J.; et al. *Inorganic Chemistry Frontiers* **2023**, *10* (4), 1315–1327.

69. Yang, T.; Wei, J.; et al. *ACS Appl. Mater. Interfaces* **2019**, *11* (26), 23372–23381.

70. Richards, B. S.; Hudry, D.; et al. *Chem. Rev.* **2021**, *121* (15), 9165–9195.

71. Jiang, Y.; Ning, H.; et al. *AIP Advances* **2018**, *8* (12), 125334.

72. Xu, H.-M.; Wang, H.; et al. *Nanomaterials* **2016**, *6* (11), 215.

73. Bharathkumar, S.; Sakar, M.; et al. *J. Phys. Chem. C* **2016**, *120* (33), 18811–18821.

74. Hossain, M. S.; Palanivel, B.; et al. *Surfaces and Interfaces* **2023**, *41*, 103240.

75. Nassereddine, Y.; Benyoussef, M.; et al. *Nanomaterials (Basel)* **2023**, *14* (1), 51.

76. Wang, M.; Wei, H.; et al. *Physics Letters A* **2020**, *384* (32), 126831.

77. Wu, F.; Guo, Y.; et al. *J. Phys. Chem. C* **2014**, *118* (28), 15200–15206.

78. You, L.; Zheng, F.; et al. *Science Advances* **2018**, *4* (7), eaat3438.

79. Chu, M.-W.; Chen, Y.-W.; et al. *ACS Appl. Mater. Interfaces* **2025**, *17* (32), 46339–46352.

80. Gunawan, M.; Bowdler, O.; et al. *ChemRxiv 2024* (0829).

81. Elumalai, N. K.; Vijila, C.; et al. *Mater Renew Sustain Energy* **2015**, *4* (3), 11.

82. Jang, J.-W.; Friedrich, D.; et al. *Advanced Energy Materials* **2017**, *7* (22), 1701536.

83. Cooper, J. K.; Ling, Y.; et al. *J. Phys. Chem. C* **2012**, *116* (33), 17360–17368.

84. Pesci, F. M.; Wang, G.; et al. *J. Phys. Chem. C* **2013**, *117* (48), 25837–25844.

85. Xiao, J.; Huang, H.; et al. *Journal of Catalysis* **2017**, *350*, 48–55.

86. Song, J.; Kim, T. L.; et al. *Nano Res.* **2018**, *11* (2), 642–655.

87. Lee, H.; Kim, H.-S.; et al. *J. Mater. Chem. A* **2020**, *8* (20), 10377–10385.

88. Chen, E. Y.; Milleville, C.; et al. *MRS Energy & Sustainability* **2019**, *5* (1), 14.

89. Liang, W.; Nie, C.; et al. *Nat. Photon.* **2023**, *17* (4), 346–353.

90. Wang, F.; Liu, X. *Chem. Soc. Rev.* **2009**, *38* (4), 976–989.

91. Mai, H.; Lu, T.; et al. *ACS Appl. Mater. Interfaces* **2018**, *10* (35), 29786–29794.

92. Zhao, C.; Kong, X.; et al. *Nanoscale* **2013**, *5* (17), 8084–8089.

93. Chen, G.; Qiu, H.; et al. *Chem. Rev.* **2014**, *114* (10), 5161–5214.

94. Wu, Y.; Chan, S. Y.; et al. *Chemistry – An Asian Journal* **2021**, *16* (18), 2596–2609.

95. Ende, B. M. van der; Aarts, L.; et al. *Phys. Chem. Chem. Phys.* **2009**, *11* (47), 11081–11095.

96. Han, S.; Deng, R.; et al. *Angewandte Chemie International Edition* **2014**, *53* (44), 11702–11715.

97. Mason, S. F. *Inorganica Chimica Acta* **1984**, *94* (1), 88.

98. Govindaraju, G. V.; Morbec, J. M.; et al. *J. Phys. Chem. C* **2018**, *122* (34), 19416–19424.

99. Purohit, S.; Bhojak, N. *Research & Reviews: Journal of Chemistry* **2013**, *2* (2), 1–3.

100. Bünzli, J.-C. G.; Eliseeva, S. V. *Chem. Sci.* **2013**, *4* (5), 1939–1949.

101. Bünzli, J.-C. G.; Piguet, C. *Chem. Soc. Rev.* **2005**, *34* (12), 1048–1077.

102. Lisnevskaya, I. V.; Myagkaya, K. V.; et al. *Ceramics International* **2020**, *46* (5), 6333–6341.

103. Song, Q.; Chen, H.; et al. *Materials Today Chemistry* **2026**, *52*, 103383.

104. In *Upconversion Nanophosphors*; Elsevier, **2022**; 391–406.

105. Fan, W.; Bai, H.; et al. *CrystEngComm* **2014**, *16* (15), 3059–3067.

106. Magazov, Y.; Aliyev, A.; et al. *RSC Adv.* **2026**, *16* (2), 1643–1661.

107. Nayak, A. K.; Gopalakrishnan, T. *ACS Appl. Nano Mater.* **2022**, *5* (10), 14663–14676.

108. Dutta, N.; Bandyopadhyay, S. K.; et al. *Remarkably high value of Capacitance in BiFeO3 Nanorod*. arXiv.org.

109. Geelani, K. A.; Alotaibi, B. M.; et al. *Journal of Energy Storage* **2024**, *85*, 111054.

110. Saha, U.; Rom, T.; et al. *ACS Appl. Energy Mater.* **2024**, *7* (6), 2241–2254.

111. Pan, Q.; Yang, C.; et al. *Electrochimica Acta* **2021**, *393*, 139079.

112. Das, R.; Shelake, A. R.; et al. *Ionics* **2025**, *31* (10), 11115–11127.

113. Oli, N.; Flórez Gómez, J. F.; et al. *ACS Appl. Energy Mater.* **2023**, *6* (21), 10853–10861.

114. Li, J.; Hwang, S.; et al. *Nat Commun* **2019**, *10* (1), 2224.

115. Haydous, F.; Scarisoreanu, N. D.; et al. *Sci Rep* **2018**, *8* (1), 15826.

116. Nie, Z.; Yan, X.; et al. *Ceramics International* **2022**, *48* (24), 36279–36286.

117. Pandey, D. K.; Modi, A.; et al. *J Mater Sci: Mater Electron* **2017**, *28* (22), 17245–17253.

118. Prashanthi, K.; Thakur, G.; et al. *Surface Science* **2012**, *606* (19), L83–L86.

119. Ramadan, A.; Ramadan, W. *Journal of Energy Storage* **2024**, *100*, 113702.

120. Kumar, A. M.; Ragavendran, V.; et al. *Colloids and Surfaces A: Physicochemical and Engineering Aspects* **2023**, *656*, 130529.

121. Agrawal, B.; Sharma, A.; et al. *Journal of Energy Storage* **2026**, *147*, 120230.

122. Wang, T.; Hu, J.; et al. *Journal of Applied Physics* **2017**, *121*, 084103.

123. Tanasescu, S.; Botea, A.; et al. In *Ferroelectrics - Physical Effects*; IntechOpen, **2011**.

Chapter 4

Ga Doped Lithium Manganese Oxide Toward Improved Stability in Aqueous Li^+ Ion Recovery From Dilute Sources

4.1 Abstract

In recent decades Li has established itself as one of the most critical elements to the global energy and technology economy. Nearly all portable electronic devices that have become a part of daily life for many rely on the unparalleled energy density of the Li-ion batteries (LIBs) that power them. Additionally, transportation and renewable energy systems have begun a large-scale switch to LIBs that further strains the Li supply. Acquiring Li has gotten cheaper and more efficient as the world has mobilized to meet the growing demand by investing in infrastructure and developing trade relationships. However, demand continues to outgrow supply, and global trade is always at the whim of ever-changing geopolitical landscape and relations. With this in mind, it is a primary focus to improve the efficiency of current Li extraction methods or develop new materials that would allow us to reach untapped sources of Li. Toward this end, traditional LIB electrode materials have been studied for use in electrochemical Li extraction from dilute sources. Unfortunately, each material has its own drawback, and many currently lack the stability or efficiency to scale to commercial or industrial use. Here, heteroatom doping of lithium manganese oxide ($LiMn_2O_4$, LMO)—a simply produced, preexisting LIB cathode material composed of earth-abundant elements—is explored for improved stability and capacity of Li.

While several dopants are considered, Ga is of particular interest due to its superior effect on the stability and capacity of LMO in aqueous environments. In Li electrolytes at dilute concentrations at or even below the most dilute industrially available brines, Ga doped LMO shows a ~25% capacity increase over commercially available LMO. LMO is also notorious for rapid degradation and poor cycling stability in aqueous environments, often losing 50% of its initial capacity after just 100 cycles.[1–4] Remarkably, Ga doped LMO is shown to retain over 85% of its initial capacity over 1000 cycles, highlighting a promising route to make LMO and electrochemical Li recovery industrially relevant.

4.2 Introduction

The global transition toward decarbonized energy systems has positioned lithium as one of the most strategically important elements of the 21st century. Lithium-ion batteries (LIBs) form the foundation for the electrification of transportation and the stabilization of intermittent renewable energy sources, achieving roughly 90% cost reduction since 2010 while dominating both electric vehicle (EV) and grid-scale storage applications.[5] Global battery demand surpassed 1.0 TWh in 2024 and is projected to reach 4.2 TWh by 2030[6], with lithium demand expected to grow eightfold by 2040 under net-zero scenarios as EVs and battery storage come to account for over 90% of total lithium consumption (Figure 4.1).[7] This trajectory has been accompanied by significant supply-side vulnerabilities: lithium prices surged eightfold during 2021–2022 before collapsing over 80% by late 2023[8], and the average market share of the top three producers of key critical

minerals rose to 86% in 2024, concentrating supply risk in a small number of nations.[9] Expanding export restrictions and geopolitical tensions further threaten supply chain reliability[10,11],underscoring the urgent need for diversified and sustainable lithium acquisition methods.

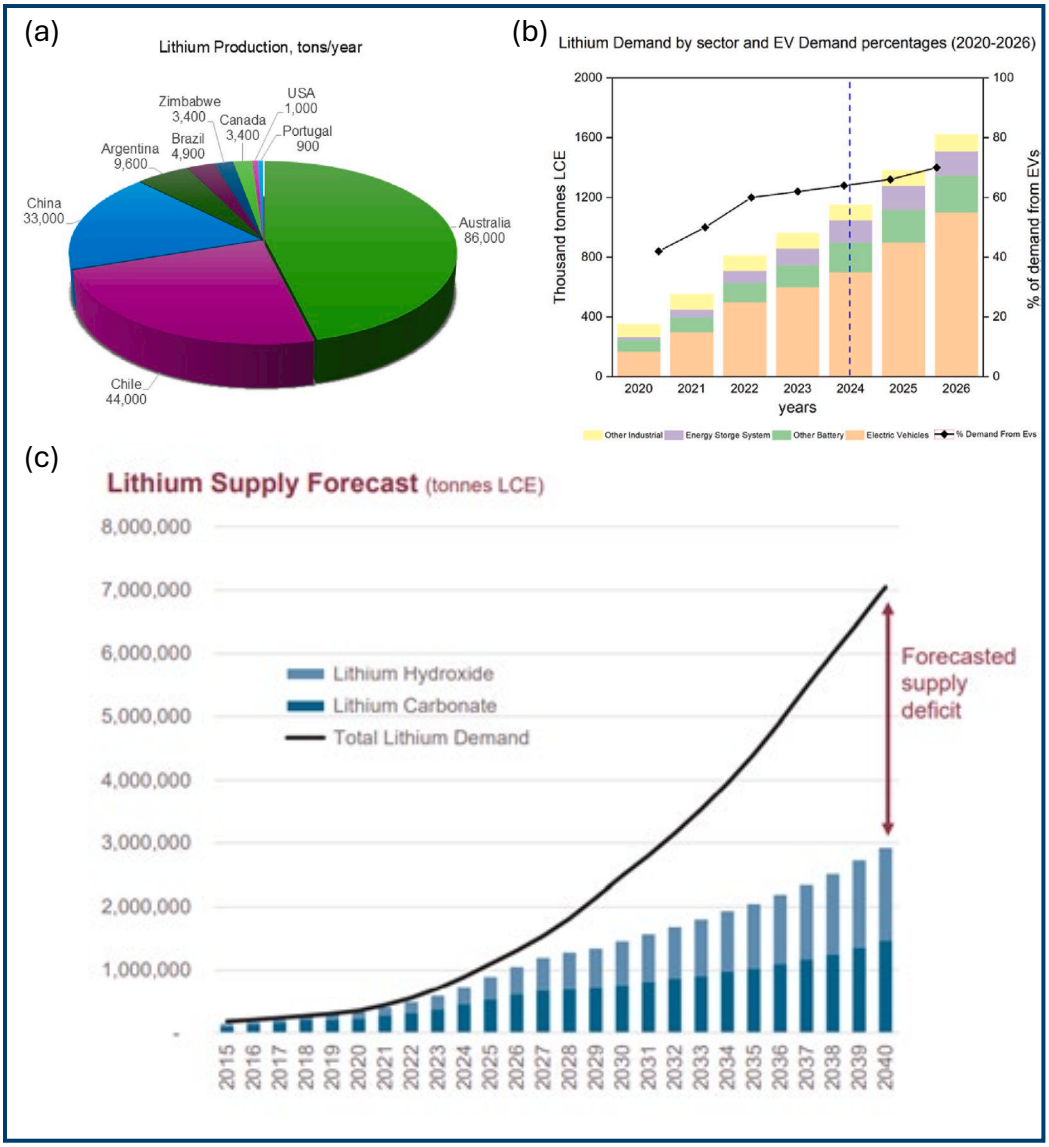

Figure 4.1 (a) Current estimates of worldwide annual Li production. (b) Li demand by sector, highlighting rapid EV growth. (c) Forecast of Li supply and demand.

Reproduced with permission from ref. ([12]). Copyright 2025 The Authors. Published by Elsevier Ltd.

Lithium is commercially sourced from two primary resources: continental brines and hard rock spodumene ores. Brine extraction relies on solar evaporation in open ponds over 12–18 months followed by chemical precipitation[13], a process criticized for its enormous water consumption and the depletion of ecologically sensitive salt flat ecosystems (Figure 4.2).[14,15] (Table 4.1) shows industrially relevant source water concentrations. Hard-rock mining employs energy-intensive sulfuric acid roasting of spodumene at high temperatures, achieving 85–90% yield but generating large volumes of acidic residues and consuming substantial energy.[1,16]

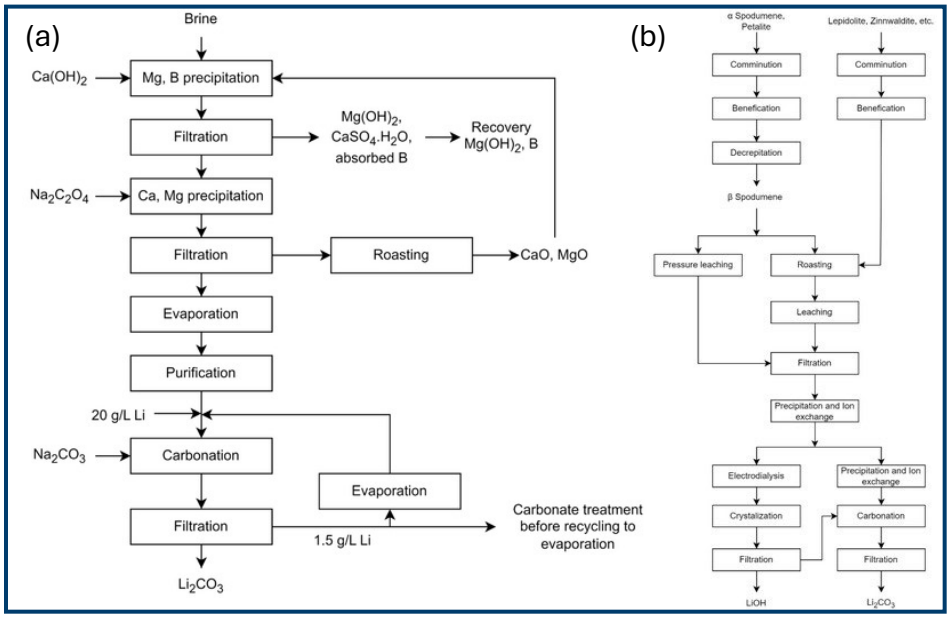

Figure 4.2 Two examples of the complicated process of extracting Li from the two main sources: Brine (a) and spodumene (b). Reproduced with permission from ref. ([17]). Copyright 2023 by the authors. Licensee MDPI, Basel, Switzerland.

Table 4.1 The Li^+ concentrations of most common industrially relevant sources. "Com" denotes commercial use, "Dev" denotes in development, and "Research" denotes lab-scale research

Source	Li^+ (mg/L)	Li^+ (mM)	Mg/Li (mass)	Na/Li (mass)	Na/Li (molar)	Status
Salar de Atacama, Chile	1,500–1,800	216–259	~6:1	~55:1	~17:1	Com
Salar del Hombre Muerto, Argentina	600–900	86–130	~1.4:1	~129:1	~39:1	Com
Zabuye Salt Lake, Tibet	500–1,500	72–216	~0.01:1	~14:1	~4:1	Com
Salar de Uyuni, Bolivia	321–530	46–76	~19:1	~188:1	~57:1	Dev
Clayton Valley (Silver Peak), USA	200–300	29–43	~1.4:1	~252:1	~76:1	Com
Salton Sea Geothermal, USA	150–400	22–58	Low	~211:1	~64:1	Dev

East Taijinar, Qaidam Basin, China	90–300	13–43	~30–100:1	~256:1	~76:1	Dev
Oilfield/produced water	1–150	0.1–22	Variable	Variable	Variable	Research
Desalination reject brine	0.4–4	0.06–0.6	Very high	Very high	Very high	Research
Seawater	0.17	0.024	~6,000:1	~63,500:1	~19,200:1	Research

Other methods under development like adsorption, solvent extraction, ion exchange, and membrane separation each suffer from limitations in selectivity, chemical consumption, waste generation, or scalability.[18,19] Collectively, these shortcomings have driven the search for alternative extraction technologies, particularly those capable of accessing unconventional and dilute lithium sources such as geothermal brines, seawater, and desalination concentrates.[19,20]

Electrochemical lithium extraction (ELE) has emerged as a particularly promising direct lithium extraction technology. First demonstrated by Pasta et al.[21], who used a $LiFePO_4$/Ag battery-like cell to convert a sodium-rich brine (Li:Na = 1:100) into a lithium-enriched solution (Li:Na = 5:1) at an energy cost of only 144 Wh per kg of lithium recovered, (ELE) exploits the selective intercalation of Li^+ into battery-type cathode materials.[3] The approach offers high selectivity, low energy consumption, rapid kinetics, and minimal chemical waste compared to conventional

methods.[22,23] Liu et al.[24] further advanced the field by developing pulsed electrochemical intercalation methods with TiO_2-coated $FePO_4$ electrodes that achieved Li^+ selectivity of approximately 1.8×10^4 over Na^+ from seawater. More recently, Yan et al.[25] demonstrated the production of battery-grade (>99.5% purity) lithium hydroxide from Salton Sea geothermal brine at a levelized cost of 4.6 USD/kg, highlighting the commercial viability of electrochemical approaches.

Among the various intercalation electrode materials, spinel $LiMn_2O_4$ (LMO) has attracted considerable attention due to its low cost, environmental friendliness, three-dimensional Li^+ diffusion pathways, and high theoretical adsorption capacity of 35–60 mg Li^+/g.[23,26] The spinel structure provides tetrahedral 8a sites that are size-selective for Li^+, preferentially accommodating the small lithium ion (0.76 Å) over competing cations such as Na^+ (1.02 Å) (Figure 4.3).[23,27]

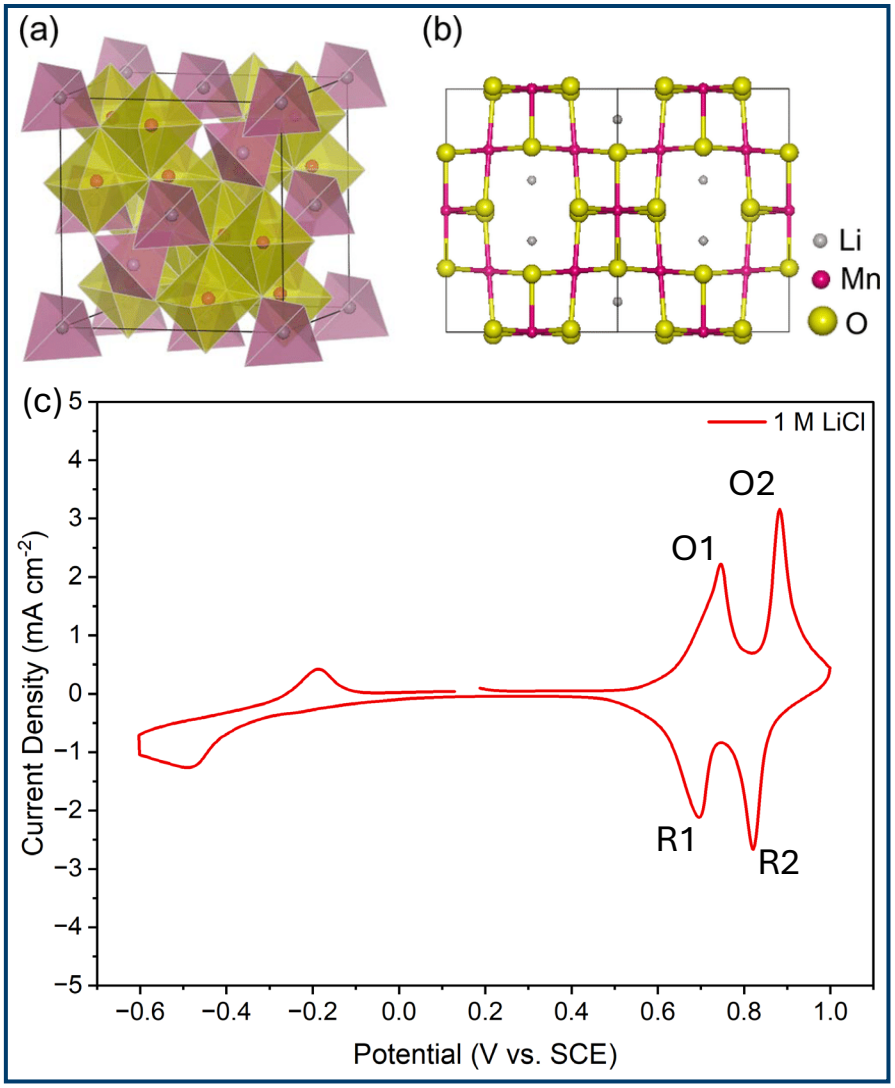

Figure 4.3 Spinel crystal structure of LMO with octahedral and tetrahedral coordination surfaces (a) and ball and stick O sub-lattice along the [110] direction (b) representation. Reproduced with permission from ref. ([28]). Copyright 2013 AIP Publishing.

LMO undergoes a two-step de/intercalation reaction that maintains the spinel structure as λ-MnO_2:

O1 $$LiMn_2O_4 \rightarrow Li_{0.5}Mn_2O_4 + 0.5Li^+ + 0.5e^-$$

O2 $$Li_{0.5}Mn_2O_4 \rightarrow \lambda\text{-}MnO_2 + 0.5Li^+ + 0.5e^-$$

R2 $$\lambda\text{-}MnO_2 + 0.5Li^+ + 0.5e^- \rightarrow Li_{0.5}Mn_2O_4$$

R1 $$Li_{0.5}Mn_2O_4 + 0.5Li^+ + 0.5e^- \rightarrow LiMn_2O_4$$

Reversible reactions O1/R1 occur at ~4 V vs. Li^+/Li and O2/R2 occur at ~4.15 V vs. Li^+/Li. However, two persistent challenges limit LMO's practical deployment. First, Mn^{3+} undergoes a disproportionation reaction:

$$2\mathrm{Mn}^{3+}{}_{(s)} \rightarrow \mathrm{Mn}^{4+}{}_{(aq)} + \mathrm{Mn}^{2+}{}_{(s)} \qquad \text{(Eq. 4.1)}$$

This causes dissolution of Mn^{2+} into the electrolyte and progressive capacity loss.[27,29,30] This is particularly a problem in aqueous applications. Second, the octahedral coordination of Mn^{3+} (d^4) by relatively low-field O^{2-} ions causes crystal field splitting of the d-orbitals and the electrons to adopt a high spin state. The Jahn-Teller effect induces tetragonal lattice distortion to break symmetry and lower the energy by further splitting degenerate orbitals (Figure 4.4). This degrades structural integrity over repeated use, as well as weakens Mn—O bonds along certain axes, allowing for easier Mn dissolution.[31]

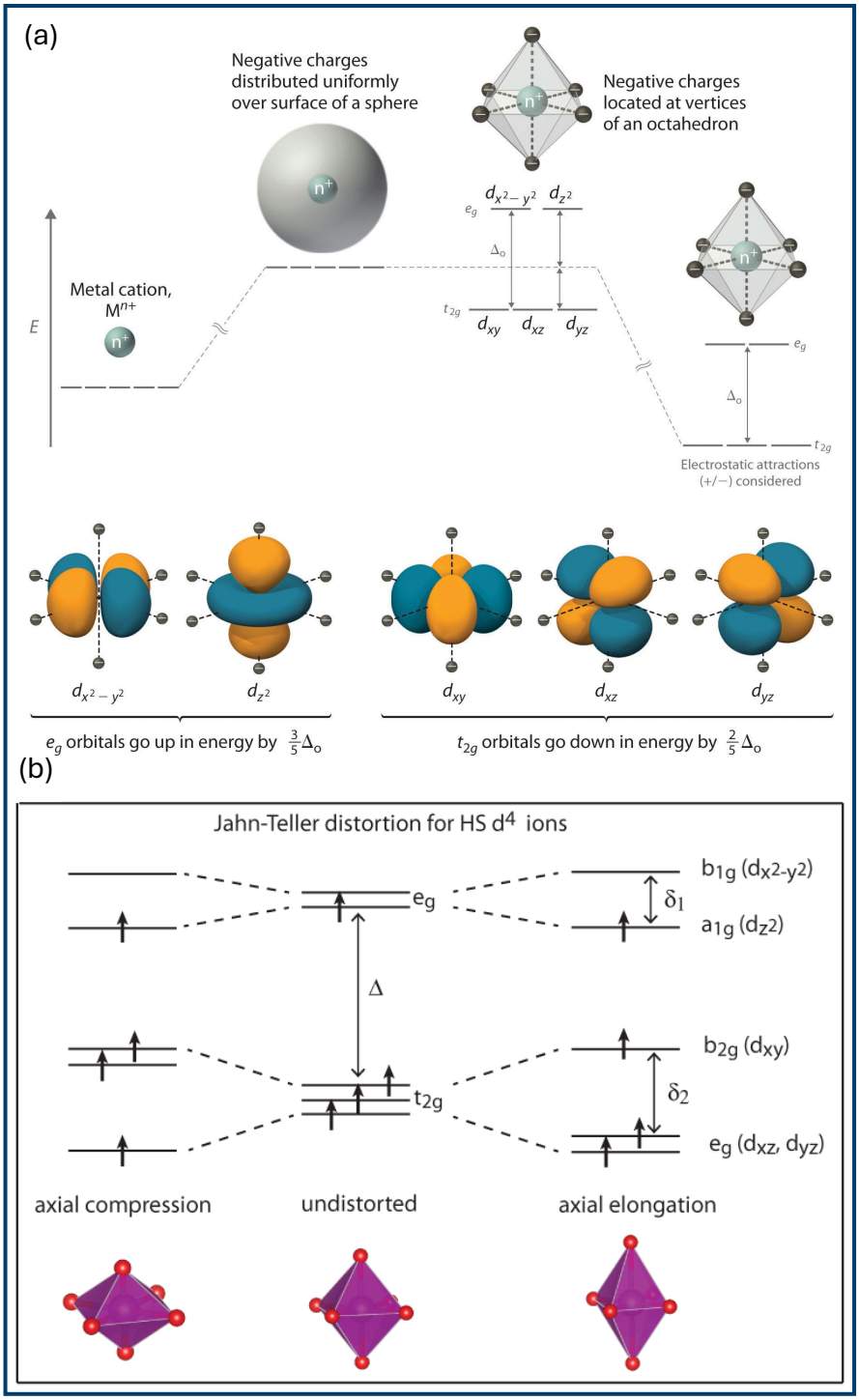

Figure 4.4 (a) Explanation of crystal field splitting and the origin of e_g and t_{2g} orbitals from d orbital interaction with the crystal field. Reproduced with permission from

ref. ([32]). Copyright 2012 the author. (b) Diagram of two types of Jahn-Teller distortion that occurs to reduce the energy of a high spin system as is the case with Mn^{3+} in LMO.

Heteroatom doping has emerged as the most widely investigated strategy for addressing these limitations, operating through a general mechanism in which the partial substitution of Mn with aliovalent cations forces the oxidation of remaining Mn^{3+} to the more stable Mn^{4+}, thereby suppressing both disproportionation and Jahn-Teller distortion.[33] Isovalent doping is also beneficial and among the most effective approaches: Al^{3+} contracts the lattice constant, narrowing intercalation channels to exclude larger competing cations while lowering the Li^+ migration barrier, yielding Li^+/Na^+ selectivities exceeding 1650 and intercalation capacities of 21.7 mg g^{-1}.[34] A dual strategy combining Al^{3+} doping with γ-Al_2O_3 surface coating reduced Mn dissolution to 0.05% per cycle and improved capacity retention from 50.8% to 92.1% over 250 cycles.[34] Nickel doping raises the average Mn oxidation state, with $LiNi_{0.05}Mn_{1.95}O_4$ achieving a selectivity coefficient α(Mg/Li) of 214 and a capacity of 20.99 mg g^{-1} in brine with Mg/Li = 46.[35] Nickel-cobalt co-doping synergistically improves both kinetics and stability, with $Li_{1-x}Ni_{0.025}Co_{0.025}Mn_{1.95}O_4$ achieving 97.93% capacity retention over 50 cycles compared to 83.92% for undoped LMO.[35] Chromium doping is particularly notable for long-cycle durability: $LiMn_{1.8}Cr_{0.2}O_4$ sustained stable (de)lithiation over 500 cycles at a Mn dissolution rate of only 0.027% per cycle.[36] Cobalt doping at the 8a site induces Mn vacancies that raise the average Mn valence and lower the Li^+ migration energy barrier, increasing Li^+ permeation

flux by approximately 50%.[37] Boron doping narrows lattice spacing via an anion-site substitution mechanism, achieving a Li/Na selectivity of 1211.68.[38] Magnesium doping-and-coating strategies have yielded Mn dissolution as low as 0.34% after 20 cycles[39], while lanthanum doping combined with epitaxial $LaMnO_3$ coating simultaneously reduces Mn^{3+} content and the Li^+ migration barrier for extended cycling stability.[40] Strontium doping stabilizes the Mn–O framework through strong Sr–O bonding, reducing Mn dissolution from 13% to 2.2% over 50 cycles.[41] Most recently, multi-cation approaches such as Ni-Co-Al co-doping have demonstrated complementary effects—elevating Mn^{4+} fraction from 41.51% to 52.12% while enhancing both electronic conductivity and framework rigidity.[35] This work has represented the state-of-the-art of LMO electrochemical lithium recovery but still reports rarely extend cycling past 50 or 100 cycles, leaving a large gap between research and industrial application.

This work investigates Ga doped LMO to further advance the performance of LMO-based electrodes for electrochemical lithium extraction from dilute brines and perhaps concentrated seawater, aiming to simultaneously improve capacity and long-term cycling stability for industrial application. Samples of pure, denoted LMO-synth, and doped LMO with a series of Ga concentrations, 1%, 3%, 5%, and 10% denoted LGMO-1, LGMO-3, LGMO-5, LGMO-10 were synthesized. All were tested in various industrially relevant conditions and compared to commercially available LMO hereafter referred to as simply LMO.

4.3 Experimental

4.3.1 Synthesis

Xerogel Nanoparticle Synthesis

A 45 g L^{-1} Ga^{3+} stock precursor solution was prepared by dissolving an appropriate amount of Ga_2O_3 in 5 M NaOH. Ga_2O_3 is a notorious refractory oxide, so this must be done with vigorous stirring for at least 6 hrs. Then, in the case of Ga doped samples, a stoichiometric aliquot of this stock solution was diluted to ~80 mL and then acidified using concentrated HNO_3 dropwise with stirring. This was done visually by observing a white precipitate form, then disappear again. Into this solution, stoichiometric ratios of each metal precursor, LiCl and $Mn(CH_3COO)_2 \bullet 4H_2O$ were dissolved. The amounts were calculated based on a desired yield of 3 g and assumed perfect stoichiometry for each concentration of LGMO. Additionally, an excess of 7% Li was included to account for loss due to the volatility of Li during the high temperature annealing process. LMO-synth samples were prepared in just pure deionized water. Once all metals were in solution, anhydrous citric acid was added in a 2:1 molar ratio with the total amount of metal. This was allowed to stir for 10 minutes for the citric acid chelation to achieve equilibrium before adding anhydrous ethylene glycol to a 1:1 molar ratio with citric acid. The beaker was then placed into an oil bath at 80 ˚C and allowed to continue to stir while the citric acid/ethylene glycol polymerization reaction took place. This was done for approximately 12 h as most of the water evaporated to form the gel. During

this time, it is necessary to monitor the reaction and adjust pH with concentrated HNO_3 to avoid hydrolysis. As the gel becomes more viscous, it begins to bubble and form a highly porous stable matrix. At this point, the stir bar was removed, and the beaker was placed in an oven at 120 ˚C for 48 h until completely dried and brittle. The resulting xerogel was then ground in a mortar and pestle until a fine powder.

The resulting xerogel powder was then placed in an alumina crucible and heated in a muffle oven at 3 ˚C min^{-1} to 500 ˚C for 6 hrs. This burns off the organic polymer residue and forms intermediate metal oxide and hydroxide species. The temperature was then ramped at 3 ˚C min^{-1} to 800 ˚C for 10 h. The sample was then allowed to cool at 3 ˚C min^{-1} to produce final product LMO-synth and LGMO.

4.3.2 Nanoparticle Characterization

Powder X-Ray Diffraction (XRD)

Nanoparticle samples were analyzed using a Rigaku SmartLab high-resolution powder X-ray diffractometer with a Cu K_α X-ray source in parallel beam mode. Samples were finely ground with a mortar and pestle and spread in a depressed glass slide sample holder. Scans were run from 2θ angles of 10˚- 80˚ with 0.02˚ steps at a rate of 1˚ min^{-1}. The resulting scans were generally background corrected and indexed using entries from the Crystallography Open Database (COD).

4.3.3 Electrochemical Measurements

All electrochemical measurements were performed with either a SP-300 BioLogic or CHI660D electrochemical workstation.

Electrode Fabrication

All samples were prepared in a carbon-based slurry by mixing 80 wt.% active material, 10 wt.% acetylene black, 10 wt.% polyvinylidene fluoride binder in N-methyl-2-pyrrolidone solvent spread at a thickness of 200 μm onto 400 μm thick carbon paper. The electrodes were placed in a vacuum oven at 60 ˚C for 12 h.

Stability and Capacity Measurements

The electrodes' long-term stability were studied in a 3-electrode beaker cell with a saturated calomel reference electrode (SCE), carbon paper counter electrode, and 50 mM LiCl electrolyte. Cyclic voltammetry (CV) was run from 0.2 to 1.2 V vs. SCE at 1 mV s^{-1} for 3 full scans to activate the electrode and allow equilibrium of the solid electrolyte interphase to be established. Then a series of 5 galvanostatic charge-discharge (GCD) cycles at each current density: 100, 50, 25, and 5 mA g^{-1} was done to determine the sample's capacity as a function of operating current. Then, finally, the samples were tested for long term stability at 100 mA g^{-1} for 1000 GCD cycles.

Ion Selectivity Measurements

Sample selectivity toward common ions was tested with the same 3-electrode beaker cell setup but in varying solutions of 1 M NaCl, KCl, $MgCl_2 \cdot 6H_2O$, and

$CaCl_2$. CV was done at 0.1 and 1 mV s^{-1} from -0.6 to 1.2 V vs. SCE to ensure there was no major electrochemical response, Faradaic or surface adsorption. Then various mock extraction solutions matching common industrial brines and seawater were prepared to observe how the presence of multiple ions may affect Li^+ uptake.

4.4 Results and Discussion

4.4.1 Crystallography

Pure and doped LMO nanoparticles were successfully prepared via a xerogel synthesis. The particles were well defined octahedra, found to be ~100 nm in size. Understanding the crystal structure of synthesized LGMO samples is essential to forming the structure-function relationship for the stability of the material. Upon Ga incorporation it was found that there was measurable lattice contraction as a function of Ga concentration (Figure 4.5). The d-spacing of each reflection is calculated according to Bragg's Law:

$$n\lambda = 2dsin(\theta) \quad \text{(Eq. 4.2)}$$

where n is an integer, λ is the wavelength of diffracted light (0.15406 nm), d is the d-spacing of the reflection, and θ is the angle of reflection. This means that the d-spacing and angle of reflection are inversely proportional. The gradual shift to higher reflection angles represents a shift to smaller d-spacing in the lattice plane. XRD data is complemented by TEM lattice fringe analysis in which the d-spacing can be directly measured from electron micrographs. The images are fast Fourier transformed and the lattice planes appear as points in reciprocal space. These points

are masked from the rest of the image and inverse Fourier transformed to produce a clear image of the lattice planes in question. Then, the distance between these is measured. (Table 4.2) summarizes and compares the d-spacing measurements of each reflection from both XRD and TEM.

Table 4.2 Calculated (XRD) and measured (TEM) d-spacings of principal crystal lattices (111) and (311) in LMO and LGMO samples.

Sample	**XRD $d_{(111)}$ (nm)**	**TEM $d_{(111)}$ (nm)**	**XRD $d_{(311)}$ (nm)**	**TEM $d_{(311)}$ (nm)**
LMO	0.48165	0.483	0.25014	0.250
LGMO-1	0.47805	0.478	0.24947	0.249
LGMO-3	0.47754	0.477	0.24893	0.249
LGMO-5	0.47652	0.476	0.24853	0.249
LGMO-10	0.474	0.474	0.24721	0.247

The most intense reflection (111) in pure LMO was measured at 18.42 degrees and in LGMO-10 at 18.72.This is a significant contraction of the lattice that is expected for several reasons. First, the Ga^{3+} is slightly smaller (0.62 Å) than the Mn^{3+} in the high spin state (0.645 Å). This alone would have only a moderate effect, but Ga^{3+} doping also effectively increases the Mn^{4+} content relative to Mn^{3+}.[42,43] In pure, stoichiometric LMO, the Mn^{3+}/Mn^{4+} ratio is 50/50, but when Ga^{3+} is

substituted, charge neutrality must be maintained despite there being a less than stoichiometric amount of Mn. This means that more Mn is in the oxidize 4+ state.[44–46] This is a significantly smaller ion (0.53 Å) and causes significant lattice contract. Furthermore, as discussed above, the Jahn Teller distortion caused by Mn^{3+} d^4 degeneracy generally causes axial elongation. This distortion is suppressed with the reduction of Mn^{3+} content, relieving some of the lattice expansion observed in pure LMO.

XPS measurements corroborate this explanation of Ga dopant induced lattice contraction (Figure 4.6). The deconvoluted Ga 3d peak area scales linearly with Ga concentration ($R^2 = 0.9977$) indicating that the dopant id present in the sample and not lost during synthesis. Furthermore, it is unlikely that any major surface segregation occurred and that incorporation is consistent. Besides no apparent secondary phases in the XRD, Mn 3s and O 1s spectra also show clear evidence of substitutional doping. The Mn 3s doublet peak separation can be correlated to the oxidation state of Mn ions in the lattice. After photoemission of one 3s electron, the remaining 3s electron is aligned either parallel or antiparallel to unpaired d electrons. This results in a doublet splitting of peak energies where the number of unpaired d electrons is directly proportional to difference in binding energy of the doublet.[47–49] Therefore, a higher number of unpaired d electrons (lower oxidation state) has a larger peak separation. The Ga 3s spectra show a systematic decrease in peak separation with nominal concentration, even suggesting that LGMO-10 has predominantly Mn^{4+} present.

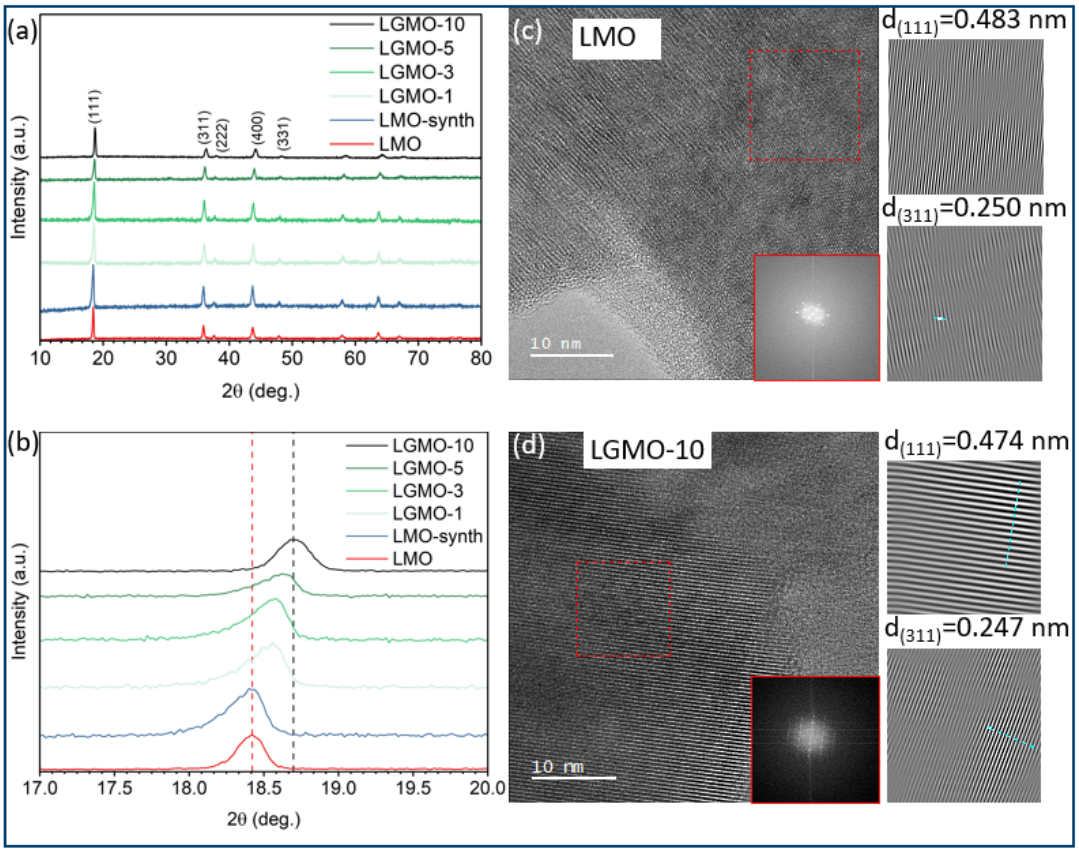

Figure 4.5 (a) Full XRD pattern of each sample showing positive single phase of highly crystalline LMO and LGMO. (b) Zoomed in view of (111) reflection showing slight shift to higher angles with increasing Ga concentration. Vertical dotted lines show peak position for LMO (red) and LGMO-10 (black). (c,d) TEM micrographs of LMO and LGMO-10 particles respectively. Lattice fringe d-spacing analysis using masked fast Fourier transform for the two principal reflections (111) and (311).

This significant increase in Mn^{4+} concentration is expected to be accompanied by lattice contraction and a reduction in Jahn Teller distortion along the octahedral axes. As such, the O octahedra are closer about the cations, changing their chemical environment. O 1s spectra show that the deconvoluted lattice oxygen peak begins to

shift to lower binding energy with increasing Ga content. This shift is attributed to electronic shielding from an increase in electron density around the O ion that would be expected from the lattice contraction and shorter Mn—O bond length.[50,51] These findings, paired with XRD and TEM lattice contraction are good evidence that Ga is substitutionally incorporating into the Mn-site of the lattice and inducing meaningful structural and chemical change to the material.

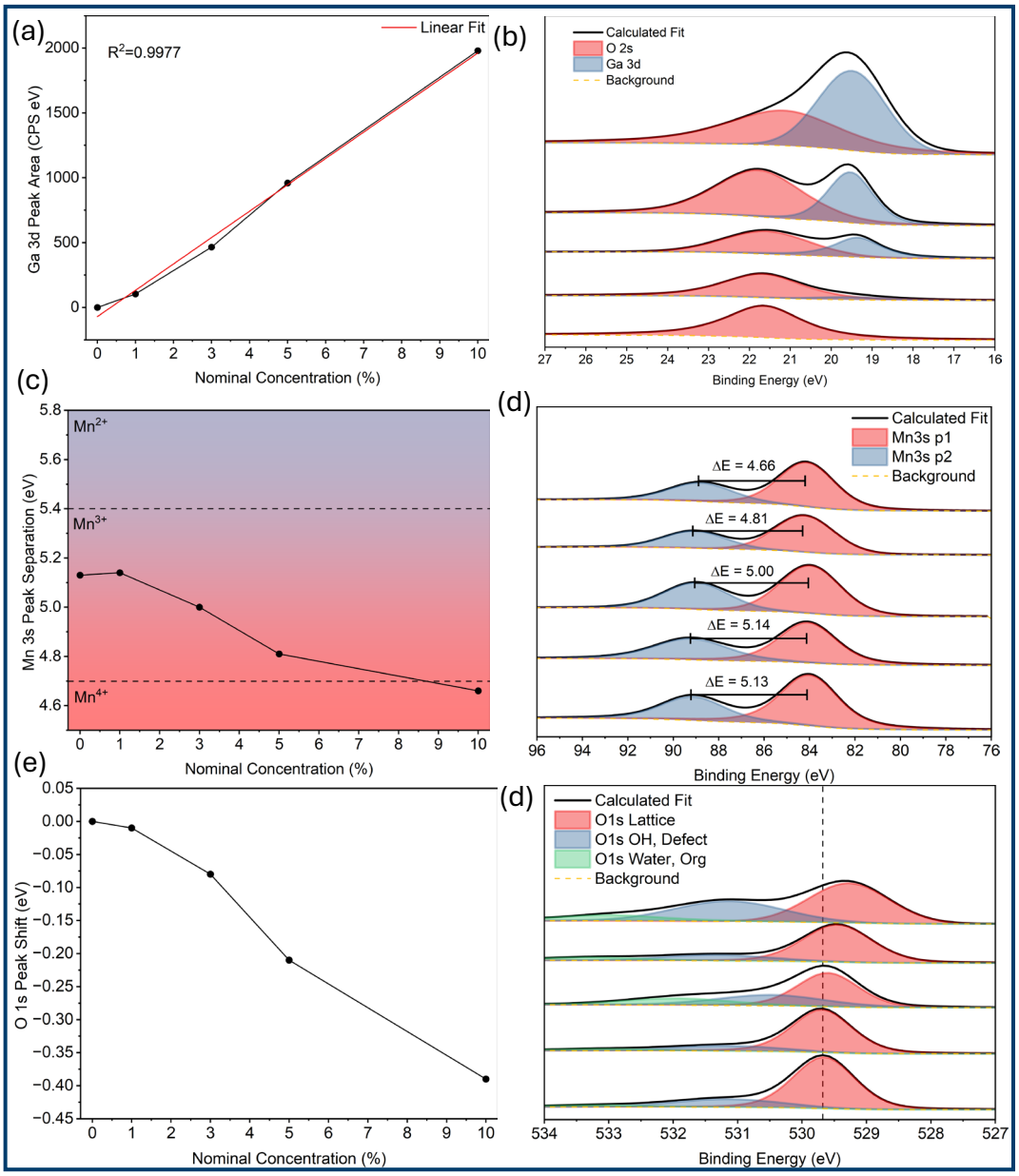

Figure 4.6 (a,b) The increase in Ga 3d signal deconvoluted from neighboring O 2s signal as a function of nominal Ga concentration. (c,d) The decrease in Mn 3s peak separation as a function of nominal Ga concentration. Horizontal dotted lines in (c) show the generally accepted ranges correlating peak separation to Mn oxidation state.

(e,f) The decrease in O 1s lattice O peak position as a function of nominal Ga concentration.

With a clear picture of the structural and chemical changes induced by the dopant, the electrochemical behavior of LMO and LGMO in dilute LiCl can be measured, compared and more mechanistically understood(Figure 4.7). 50 mM LiCl is approximately as dilute as the most dilute industrially relevant brines across the world. Interestingly, LGMO-1 shows a large peak shift to lower potentials, then this shift slowly increases back to the original, expected redox potentials as Ga content is increased. The initial decrease in potential is likely due to Ga favorably altering the electronic structure about Mn ions, lowering the energy barrier for oxidation. LGMO-1 shows very small contraction to the lattice, so Li^+ diffusion pathways are largely uninterrupted. As Ga content increases, the lattice contraction becomes more significant and can impact the Li^+ diffusion, overcoming any electronic benefit provided by the dopant. Increased diffusion resistance would manifest as kinetic overpotential in CV.[44,52] This is also clearly the case as the anodic and cathodic peak separation increases with Ga content. Kinetic limitations spread the O1/R1 and O2/R2 reactions as Li^+ struggles to diffuse through the smaller lattice pathways.[46] Additionally, the peak sharpness quickly deteriorates with ga concentration. It appears that the intermediate phase between O1 and O2 is less ordered and that Li^+ diffusion occurs through a more continuous process rather than discrete, stoichiometric, ordered, phase changes.[53]

As expected, LMO and LGMO samples displayed exceptional selectivity toward Li^{3+} when compared against other common brines ions. The full de/lithiation reaction is apparent in LiCl, while no appreciable current response is apparent in any of the other electrolytes. The diffusion channels in LMO are quite small and suited for smaller ions like Li^{+}, and Mg^{2+}. However, the prohibitively high hydration energy of Mg^{2+} makes it much less likely to desolvate and intercalate. That being said, Mg^{2+} is bar far the biggest intercalation competitor in source brines. The ionic radii and solvation energies of relevant ions are listed in (Table 4.3), In more dilute applications of LMO like seawater, the main competing ion turns out to be Na^{+}. Despite a much larger ionic radius, it has a relatively low hydration energy and most often exists in a large excess in brines and seawater. The extremely high Na^{+}:Li^{+} ratio means that although less thermodynamically favorable, statistically, Na^{+} tends to intercalate into the material and degrade capacity. It is therefore important to test stability and selectivity in mock brine or seawater solutions mimicking the absolute and relative concentrations of each ion of concern. This should be carried out in following studies.

Table 4.3 Ionic radii and solvation energies of common brine and seawater cations,

Ion	Ionic Radius (pm)	Hydration Energy (kJ mol^{-1})
Li^{+}	69	-515
Na^{+}	102	-405
K^{+}	138	-320

Mg^{+}	72	-1,922
Ca^{2+}	100	-1,590

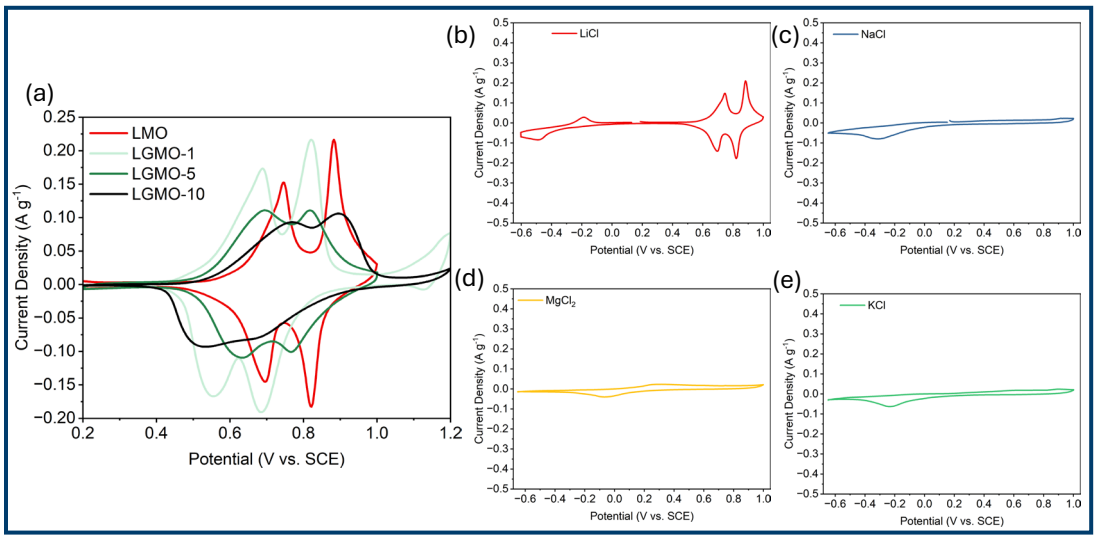

Figure 4.7 (a) Cyclic voltammogram of LMO and LGMO samples at a scan rate of 0.1 mV s^{-1}. Selectivity voltammograms of LMO in LiCl (a), NaCl (c), $MgCl_2$ (d), KCl (e).

It is expected that, while the effect would be minimal, a decrease in Mn^{3+}:Mn^{4+} ratio reduce the capacity of the LGMO. The de/intercalation reaction is dependent on the reversible oxidation of Mn^{3+} and so any decrease in Mn^{3+} concentration would directly lower capacity. Considering that the study is carried out at modest concentrations <10%, it is expected that the capacity would not be meaningfully diminished beyond 10%. This is the case for higher concentrations such as LGMO-5 and LGMO-10 that have similar or slightly diminished capacity during

GCD cycling of the electrodes (Figure 4.8). Again, LGMO-1 behaves differently, exhibiting a significantly increased capacity, 121.3 mAh g^{-1} at 5 mA g^{-1}, although this improvement is not strongly maintained across operating currents. In general, all other samples had good rate capability, with near constant capacity at all tested currents, but LGMO-1 sees a steady decrease as operating current increases. At the long-term operating current of 100 mA g^{-1}, the capacity dropped to 101.6 mAh g^{-1}. While this is still an improvement over LMO, that constitutes a nearly 20% drop in capacity at operating current.

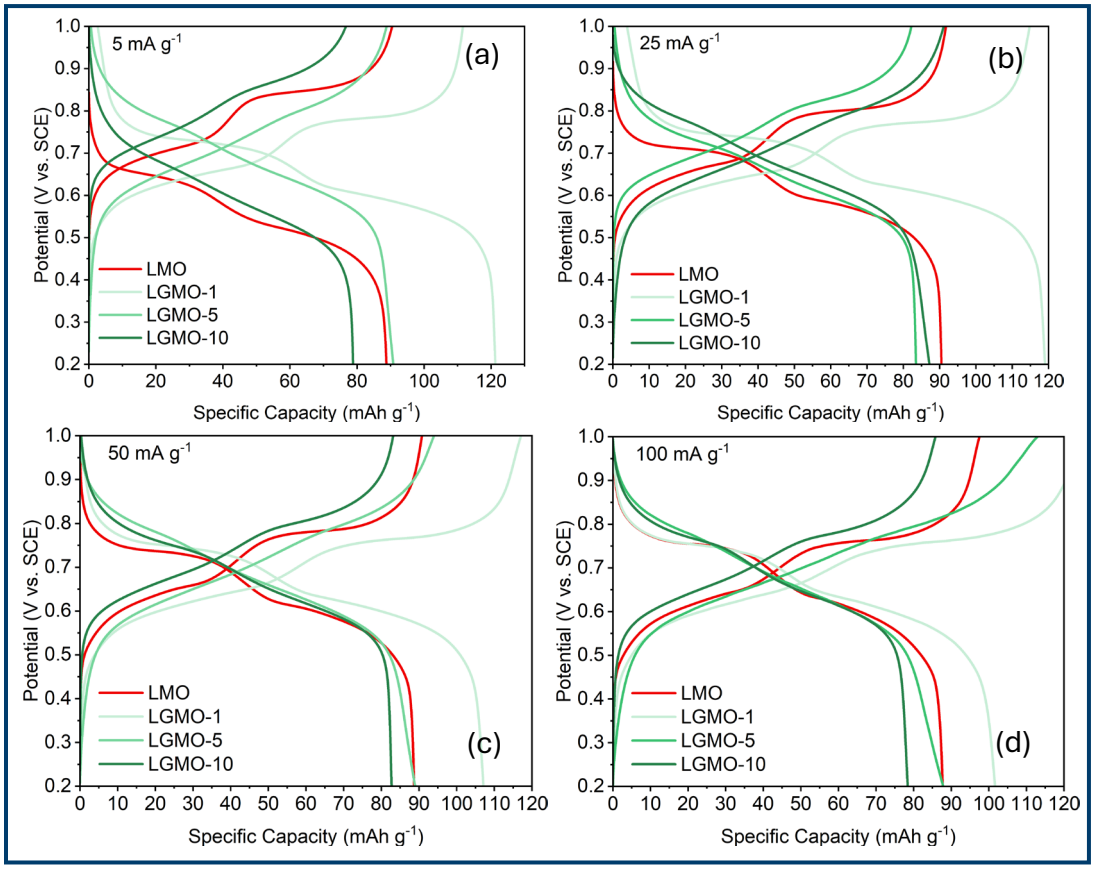

Figure 4.8 Representative GCD curves plotted as a function of specific capacity for a series of operating currents: 5 mA g^{-1} (a), 25 mA g^{-1} (b), 50 mA g^{-1} (c), 100 mA g^{-1} (d).

One of the main limitations of LMO for electrochemical lithium recovery is its instability in aqueous systems. Mn dissolution occurs much more quickly in water due to proton assistance and how readily water solvates the Mn^{2+} ion especially when compared to most common nonaqueous batter electrolyte solvents.[2,54,55]is leads to rapid degradation of the structure of LMO electrodes, and hence, their capacity during cycling. It is well documented and exhibited here that LMO can lose half of its capacity within 100 cycles.[1–4,12,15,22] Ga doping, and the resultant increase in Mn^{4+} concentration, suppression of Jahn Teller distortion, and lattice contraction leading to stronger Mn—O bonds, is expected to measurably reduce the Mn dissolution and maintain capacity overt cycling. This is immediately apparent as all three LGMO samples maintain over 85% capacity retention over 100 cycles. The effect is only very slight in LGMO-1, with still a nearly linear decrease in capacity like LMO, but at a much slower rate. LGMO-5 and LGMO-10 are both more stable over the first 100 cycles, but LGMO-5 is of particular note with 100% retention over 100 cycles and 85% retention over 1000 cycles. Because this is a slow intercalation process, 1000 cycles at the relatively low mass loading of these electrodes took nearly 2 months of continuous cycling. The electrolyte was analyzed after the cycling with inductively coupled plasma-optical emission spectroscopy to determine the Mn concentration. All Mn in the electrolyte would be a product of unwanted, sample

degradation from Mn dissolution from the Mn disproportionation reaction (Eq. 4.1). The Mn concentration of LGMO-5 was about 40x less than LMO and LGMO-1 further supporting the Ga suppression of dissolution as the source of this newfound stability (Table 4.4). It seems that there is an optimal doping concentration that balances the competing mechanisms of electronic and structural effects to produce a high capacity, long cycling lithium recovery material.

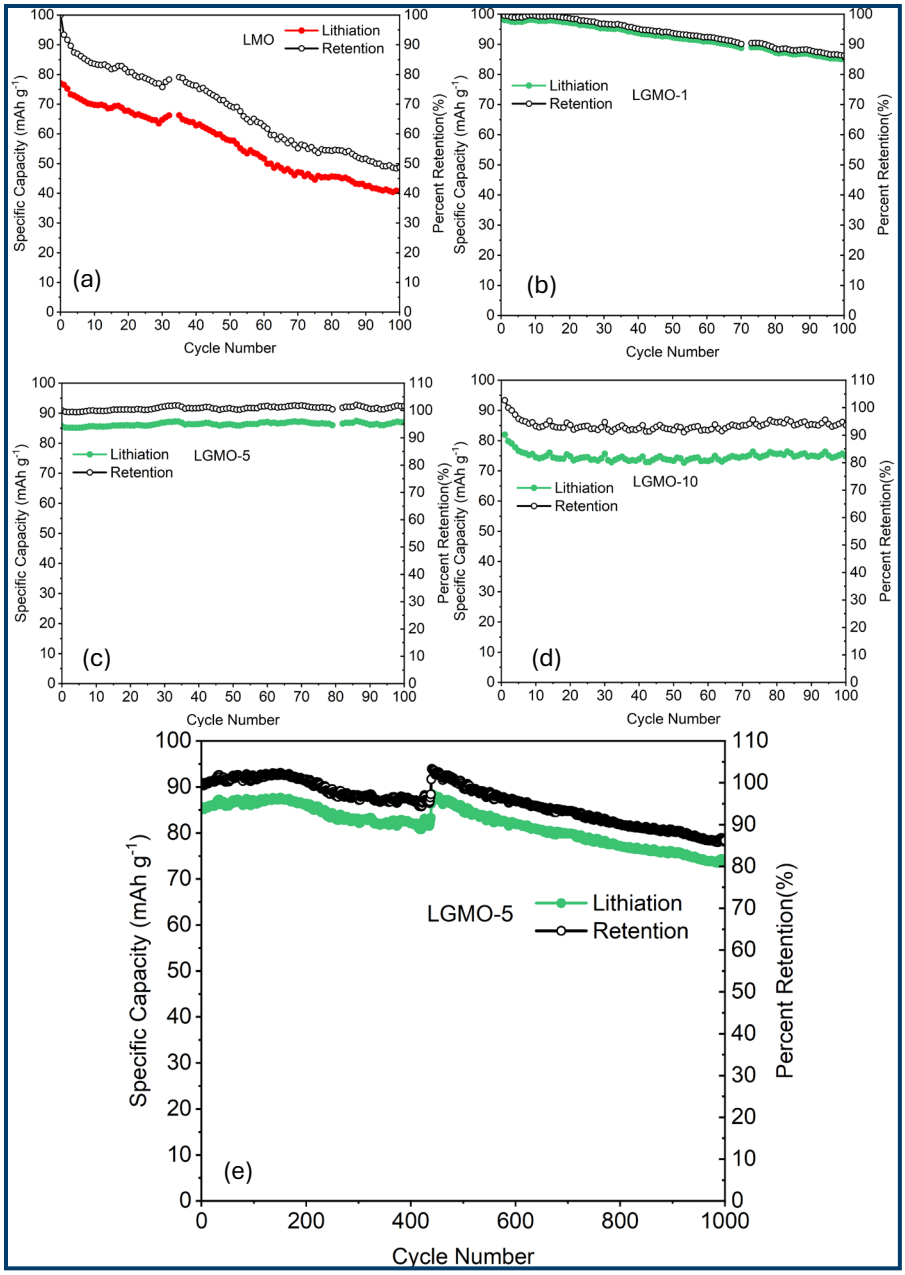

Figure 4.9 First 100 cycles of LMO (a), LGMO-1 (b), LGMO-5 (c), and LGMO-10 (d) cycled at 100 mA g^{-1} in 50 mM LiCl. (e) Shows extended performance of LGMO-5 out to 1000 GCD cycles in the same conditions.

Table 4.4 Mn concentrations in the electrolyte after long term cycling experiments.

Sample	Mn Concentration (ppm)
LMO	46
LGMO-1	47
LGMO-5	1.2
LGMO-10	22

4.5 Conclusion

This work demonstrates that Ga doping of spinel $LiMn_2O_4$ is an effective strategy for simultaneously improving the capacity and long-term cycling stability of LMO electrodes for electrochemical lithium extraction from dilute aqueous sources. A series of Ga-doped LMO samples (LGMO-1, LGMO-3, LGMO-5, and LGMO-10) were synthesized via a xerogel route and systematically characterized by XRD, TEM, XPS, and electrochemical methods.

Structural characterization revealed that Ga^{3+} incorporation into the Mn octahedral site induces measurable lattice contraction, confirmed by both XRD peak shifts and TEM lattice fringe analysis. XPS Mn 3s multiplet splitting measurements provided direct evidence that Ga doping progressively increases the Mn^{4+}:Mn^{3+} ratio, consistent with the charge compensation mechanism expected from trivalent dopant substitution. The accompanying shift of the O 1s lattice oxygen peak to lower binding

energy further corroborates a shortened Mn–O bond environment resulting from the lattice contraction and Jahn-Teller distortion suppression.

Electrochemical evaluation in 50 mM LiCl, a concentration representative of the most dilute industrially relevant brines, revealed that Ga doping produces competing effects on performance that are concentration dependent. LGMO-1 exhibited a notable capacity enhancement over undoped LMO, attributed to favorable electronic structure modification at the Mn site with minimal disruption to Li^+ diffusion pathways. At higher doping levels, significant lattice contraction increased kinetic resistance to Li^+ transport, manifested as broadened CV peaks, increased anodic-cathodic peak separation, and diminished rate capability.

The most significant finding of this study is the dramatic improvement in cycling stability achieved by Ga doping. While undoped LMO lost approximately half its initial capacity within 100 cycles, consistent with the well-documented aqueous degradation behavior of this material, LGMO-5 retained 100% capacity over 100 cycles and 85% over 1000 cycles of continuous galvanostatic charge-discharge at 100 mA g^{-1}. ICP-OES analysis of the electrolyte after extended cycling confirmed that the Mn concentration for LGMO-5 was approximately 40 times lower than for undoped LMO, directly linking the stability improvement to suppressed Mn disproportionation and dissolution. This 1000-cycle stability in dilute aqueous electrolyte substantially exceeds the cycling lifetimes reported in the current literature for doped LMO in electrochemical lithium recovery applications, where most studies are limited to 50–100 cycles.

These results suggest that an optimal Ga doping concentration exists near 5% in this system. This seems to balance electronic stabilization (suppression of Jahn-Teller distortion and Mn disproportionation) against structural constraints (narrowed Li^+ diffusion channels) to produce a high-performance electrode material. The higher Mn dissolution observed in LGMO-10, despite its high Mn^{4+} content, warrants further investigation and may indicate excessive lattice strain, surface segregation effects, or secondary phase formation at high dopant loading.

Future work should explore the performance of Ga-doped LMO in real brine matrices containing competing cations (Na^+, K^+, Mg^{2+}, Ca^{2+}) at industrially relevant ratios, quantify Li^+/cation selectivity coefficients, and evaluate electrode performance in continuous flow electrochemical extraction systems. Complementary characterization including electrochemical impedance spectroscopy, post-mortem electron microscopy of cycled electrodes, and computational modeling of Ga site energetics would further elucidate the structure-performance relationships identified here. The exceptional stability demonstrated by LGMO-5 represents a meaningful step toward closing the gap between laboratory-scale electrochemical lithium recovery research and industrial deployment.

4.6 References

1. Murphy, O.; Haji, M. N. *Front. Chem. Eng.* **2022**, *4*.
2. Gonzalez-Rosillo, J. C.; Guc, M.; et al. *Chem. Mater.* **2024**, *36* (12), 6144–6153.
3. Calvo, E. J. *ACS Omega* **2021**, *6* (51), 35213–35220.
4. Xue, N.; Wu, X.; et al. *ACS Nano* **2024**, *18* (49), 33743–33753.
5. *Batteries and Secure Energy Transitions – Analysis*. IEA.
6. *Building new advantages for batteries by 2035 | McKinsey*.
7. *Outlook for key minerals – Global Critical Minerals Outlook 2024 – Analysis*. IEA.
8. *Executive summary – Global Critical Minerals Outlook 2025 – Analysis*. IEA.
9. *Diversification is the cornerstone of energy security, yet critical minerals are moving in the opposite direction - News*. IEA.
10. *Growing geopolitical tensions underscore the need for stronger action on critical minerals security – Analysis*. IEA.
11. Wang, B.; Wang, L.; et al. *Front. Energy Res.* **2023**, *10*.
12. Ali, A.; Afrin, S.; et al. *Journal of Environmental Management* **2025**, *391*, 126512.
13. Nilges, B.; Reinert, C.; et al. *Journal of Cleaner Production* **2024**, *434*, 140062.
14. Cai, B.; Feng, K.; et al. *Resources, Conservation and Recycling* **2024**, *205*, 107570.
15. Flexer, V.; Baspineiro, C. F.; et al. *Science of The Total Environment* **2018**, *639*, 1188–1204.

16. Dessemond, C.; Lajoie-Leroux, F.; et al. *Minerals* **2019**, *9* (6), 334.

17. Marcinov, V.; Klimko, J.; et al. *Metals* **2023**, *13* (7), 1213.

18. Luo, G.; Li, X.; et al. *Desalination* **2023**, *548*, 116228.

19. Baudino, L.; Santos, C.; et al. *Advanced Science* **2022**, *9* (27), 2201380.

20. Battistel, A.; Palagonia, M. S.; et al. *Advanced Materials* **2020**, *32* (23), 1905440.

21. Pasta, M.; Battistel, A.; et al. *Energy Environ. Sci.* **2012**, *5* (11), 9487–9491.

22. Kim, J.-S.; Lee, Y.-H.; et al. *Environ. Sci. Technol.* **2015**, *49* (16), 9415–9422.

23. Lee, J.; Yu, S.-H.; et al. *Phys. Chem. Chem. Phys.* **2013**, *15* (20), 7690–7695.

24. Liu, C.; Li, Y.; et al. *Joule* **2020**, *4* (7), 1459–1469.

25. Kong, L.; Yan, G.; et al. *Nat Commun* **2025**, *16* (1), 806.

26. Kanoh, H.; Feng, Q.; et al. *J. Electrochem. Soc.* **1995**, *142* (3), 702.

27. Xu, S.; Song, J.; et al. *Journal of Membrane Science* **2021**, *635*, 119441.

28. Mukai, K.; Andreica, D.; et al. *J. Appl. Phys.* **2013**, *113* (5), 053904.

29. Shi, W.; Zhang, Y.; et al. *Separation and Purification Technology* **2026**, *394*, 137690.

30. Zhou, G.; Sun, X.; et al. *J. Phys. Chem. Lett.* **2020**, *11* (8), 3051–3057.

31. Sun, X.; Xiao, R.; et al. *Langmuir* **2021**, *37* (17), 5252–5259.

32. *Principles of General Chemistry - Table of Contents*.

33. Tan, G.; Wan, S.; et al. *Advanced Materials* **2024**, *36* (14), 2310657.

34. Yin, R.; Xu, W.; et al. *Desalination* **2026**, *620*, 119647.

35. Wu, Y.; Shi, P.; et al. *Energy Fuels* **2023**, *37* (5), 4083–4093.

36. Tian, G.; Gao, J.; et al. *Electrochimica Acta* **2024**, *475*, 143361.

37. Li, Y.; Pan, Y.; et al. *Journal of Electroanalytical Chemistry* **2026**, *1009*, 119981.

38. Liao, G.; Yu, L.; et al. *Water Research* **2025**, *274*, 123131.

39. Fan, W.; Ma, L.; et al. *Desalination* **2025**, *615*, 119260.

40. Fang, D.; Liu, F.; et al. *Desalination* **2025**, *604*, 118692.

41. Fang, D.; Zhang, X.; et al. *Chemical Engineering Journal* **2025**, *521*, 166161.

42. Shannon, R. D. *Acta Cryst A* **1976**, *32* (5), 751–767.

43. Yu, Y.; Guo, J.; et al. *Sci Rep* **2019**, *9* (1), 16864.

44. Iturrondobeitia, A.; Goñi, A.; et al. *Journal of Power Sources* **2012**, *216*, 482–488.

45. Li, X.; Xu, Y.; et al. *Journal of Alloys and Compounds* **2009**, *479* (1), 310–313.

46. Lan, L.; Li, S.; et al. *Nanoscale Res Lett* **2018**, *13* (1), 251.

47. Cerrato, J. M.; Hochella, M. F. Jr.; et al. *Environ. Sci. Technol.* **2010**, *44* (15), 5881–5886.

48. Ilton, E. S.; Post, J. E.; et al. *Applied Surface Science* **2016**, *366*, 475–485.

49. Isaacs, M. A.; Graf, A.; et al. *Surface and Interface Analysis* **2025**, *57* (4), 285–290.

50. Yang, M.; Ma, J.; et al. *Journal of Alloys and Compounds* **2024**, *986*, 174122.

51. Ou, S.; Li, Z.; et al. *Particuology* **2024**, *94*, 146–157.

52. Lin, Y.; Li, F.; et al. *Small Methods* **2025**, *9* (8), 2402233.

53. Yamada, A.; Tanaka, M.; et al. *Journal of Power Sources* **1999**, *81–82*, 73–78.

54. Tesfamhret, Y.; Liu, H.; et al. *ChemElectroChem* **2021**, *8* (8), 1516–1523.

55. Huang, J.; Xue, L.; et al. *Nat Commun* **2024**, *15* (1), 6666.

Chapter 5

Hydrogen Treatment of Metal Oxides: Methods, Mechanisms, and Implications

5.1 Abstract

Manipulating and tailoring the properties of metal oxides towards specific applications is key to achieving current economic and technological goals. Different forms of hydrogen treatment, either during synthesis or in a post-process treatment, can have wide-ranging effects on a metal oxide material. Hydrogen has the potential to reduce the material by inducing oxygen vacancies at the surface and in bulk but also can be integrated as a substitutional or interstitial dopant. Reports of improved material, optoelectronic, and magnetic properties after such treatments have spurred a large response from the scientific community. The ability of hydrogen treatment to tune these properties has cast a wide net for possible applications, many especially relevant to current initiatives towards sustainable energy generation and storage, and electronic components. This research reached a height in the 2010s with studies exploring the fundamental chemistry of the underlying mechanisms or optimizing the process of inducing these observed changes. Interest in hydrogen treatment has waned in recent years and this review aims to reinvigorate the field by summarizing some of the profound effects that hydrogen treatment has on metal oxides, as well as some of the unanswered questions of how hydrogen treatment achieves these effects.

5.2 Introduction

Metal oxides (MOs) are a broad class of compounds that have long been studied for their material[1], optoelectronic[2,3], magnetic[4,5], and electrochemical[6–8] properties. They are noted for normally possessing relative stability and facile syntheses compared to other metal compounds like pnictogenides, chalcogenides, or halides. This makes MOs a good starting point when designing materials that can meet our economic and environmental demands. In the last 100 years, a deeper understanding of MO crystal and electronic structure, specifically their semiconducting nature, has positioned them at the forefront of materials research and given rise to many essential electronic and optoelectronic components we use every day. While not all MOs are considered semiconductors, many exhibit semiconducting electronic energy band structures with moderate bandgaps. Typically, the occupied valence band is comprised of oxygen 2p orbitals, and the unoccupied conduction band is comprised of the metal d or s orbitals[9,10]. Many MOs have bandgaps of 3.5 eV or less, allowing them to conduct electricity under certain conditions[10]. Nevertheless, many MOs do not naturally meet the functional requirements of their technological applications and require some tuning to selectively improve various aspects of their function. Scientists have traditionally employed two strategies to engineer MOs for their needs: morphology engineering/nanostructuring[11–13], and crystal defect engineering[11,14–17]. Morphology engineering can have profound effects on interface chemistry and catalytic properties[18,19] of the material as well as it's light absorption and emission capabilities[20]. For instance, selective growth of specific

crystal facets can show improved reactivity towards reactions of interest[21], and 1-D and 2-D materials can display vastly different electrical properties[22,23]. Crystal defect engineering, including intrinsic and extrinsic defects, allow fine tuning of MO optoelectronic properties[11,14,16,24]. Intrinsic defects, such as atom vacancies, are often induced via chemical reduction or stoichiometric manipulation. Extrinsic defects like heteroatom doping and substitutional impurities are introduced by adding small amounts of dopant during synthesis. These strategies can result in marked changes to the band structure and conductivity of the materials, but the exact mechanisms toward improving MO properties remains an active area of research. For example, heteroatom doping in α-Fe_2O_3 has been shown experimentally to increase charge carrier density[11], and computationally to improve electrical conductivity by increasing the mobility of small polarons, the majority charge carrier in the material[16]. In other cases, heteroatom doping can tune the bandgap of a material to enhance its light absorption efficiency[25,26].

One emerging area of interest is the mechanism by which hydrogen treatment can improve MO properties. Studies have shown that hydrogen treatment can enhance various properties like light absorption, charge separation, and electrical conductivity[6,26–28]. However, the mechanism behind these improvements remains unclear. There is inconclusive evidence as to whether hydrogen treatment is merely reducing the material through induction of oxygen vacancies and surface hydrogenation, or if hydrogen atoms can diffuse into the material and occupy interstitial lattice sites. Understanding whether one or both of these processes are

occurring is critical as they have different implications for material properties. Determining the mechanism will advance the application of hydrogen treatment in MO optimization and help inform future research directions in the field.

5.3 Methods of Hydrogen Treatment

Hydrogen treatment of metal oxides involves a variety of methods, each characterized by distinct mechanisms and resulting effects. The most commonly studied method is exposing the material to a hydrogen- or water-containing atmosphere usually under high temperature, high pressure, or for prolonged treatment. In this process, hydrogen can interact with the material's surface to form O-H bonds and, with enough thermal energy or time, diffuse deeper into the material and exist interstitially[29]. Alternatively, hydrogen may also be introduced directly during the chemical synthesis of MOs such as the polymer solution process[27] or during physical vapor deposition (PVD) techniques like sputtering or pulsed laser deposition[30–32]. For example, hydrogen atoms are directly incorporated into the crystal as it forms by performing the PVD process in a hydrogen-containing atmosphere. Recently, other post-synthesis methods such as acid-mediated proton-electron co-doping have also been demonstrated to yield hydrogen doped metal oxides[33–35]. This method involves coupling the MO with a metal with a lower work-function than the material and treating them with an acid solution. Protons from the acid are injected into the MO alongside electrons from the paired metal, recombining to form neutral hydrogen atoms within the crystal lattice. A similar approach can also be achieved through electrochemical methods.[36–39] Understanding the differences and

similarities among these processes are important to study as each offers unique use-cases and outcomes. A summary of the most common hydrogen treatment methods is presented in (Table 1).

Numerous studies have reported the preparation of MOs followed by a post-process treatment of the material in a hydrogen-containing atmosphere at elevated temperatures. As early as 1980, Harris and Shumacher[38] reported improved conductivity in hydrogen-treated rutile TiO_2 after heating pristine TiO_2 under H_2 gas flow at 500 ˚C. Although the MO reduction with hydrogen had long been known, this was one of the earliest reports to show partial reduction of a MO toward improved properties. The results were comparable to other treatment methods such as vacuum annealing and electrochemical hydrogen loading.[38] This hydrogen treatment method produced the same characteristic blueish-black TiO_2 observed during cathodic hydrogen loading of vacuum reduced TiO_2. This color change has become a hallmark for reduced and hydrogen treated MOs, especially TiO_2, and is often attributed to mid-gap states resulting from O vacancies in the reduced material[25,40,41]. Various examples of this color change are depicted in (Figure 1).

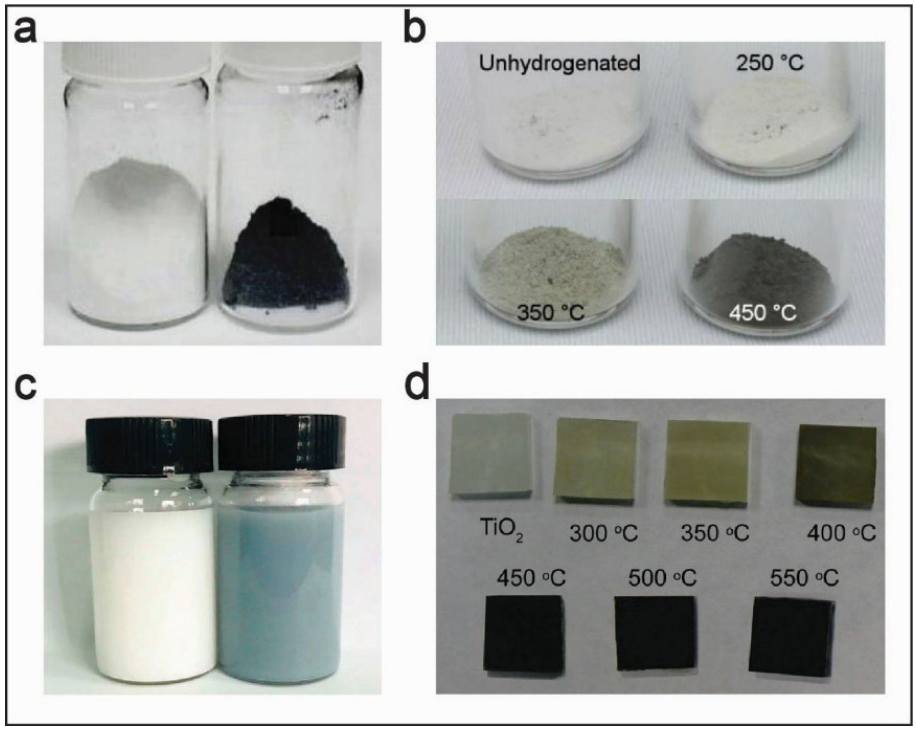

Figure 5.1 Examples of color change observed in post-process hydrogen-treated TiO_2 powders and films. (a) High pressure hydrogenation[28] Reproduced from ref. 28. Copyright 2011 Science b) High temperature hydrogenation[42] Reproduced from ref. 52. Copyright 2013 American Chemical Society (c) Proton-electron co-doping[34] (Reproduced from ref. 34. Copyright 2020 American Chemical Society) (d) High temperature hydrogenation.[43] Reproduced from ref. 47. Copyright 2011 American Chemical Society

TiO_2 is the most commonly reported hydrogen-treated MO, especially for photoelectrochemical and photocatalytic applications[42]. This same general approach has also been extensively applied to other MO studies. For example, Cushing *et al.*[24] demonstrated that pristine anatase TiO_2 heated in a quartz tube furnace at 600 ˚C for 3 h with a H_2 flow rate of 0.2 L min^{-1} yielded reduced TiO_2. This treatment induced a

notable color change from white to blue-black. The presence of Ti^{3+} in reduced TiO_2 was confirmed using a variety of characterization methods including X-ray photoelectron spectroscopy (XPS) and electron paramagnetic resonance (EPR). WO_3 is another common example of a hydrogen-treated MO. Lower temperature annealing of WO_3 nanoflake photoelectrodes in a hydrogen atmosphere (350-450 ˚C) improved carrier concentration and efficiency of charge collection[44]. Even higher temperatures, such as 700 and 800 ˚C, have yielded similar results for reduced TiO_2.[45] In some cases, treatment temperatures can exceed 1200 ˚C, depending on the MO under investigation.[46]

A modified approach to hydrogen annealing involves decomposing H_2 source gas into reactive forms such as radicals, atomic hydrogen, and ions. These reactive species are more efficient at reducing MOs. One such example reported by Wallinga et. al.[47] studied the temperature dependence and rate of SnO_2 reduction by hydrogen radicals. Using hydrogen radicals generated by hot-wire and plasma methods, the study shows that both temperature and the hydrogen source significantly influence the rate and degree of reduction. Reduction was slower and less complete at lower temperatures such as 230 ˚C. In contrast, SnO_2 was nearly fully reduced to metallic tin at higher temperatures like 430 ˚C. Hot-wire-produced hydrogen radicals were also more effective, achieving complete reduction within 1 minute, while plasma-generated hydrogen radicals took 4 times longer. Significantly, this process was found to be reversible, allowing SnO2 to regain its optoelectronic properties if the reduction was halted before the formation of elemental tin aggregates.

Despite promising results of post-process hydrogen treatment, there is growing interest in lowering energy costs and addressing safety concerns by conducting treatments under ambient or low-temperature conditions. However, such conditions are often insufficient for effective hydrogen treatment, and when successful, typically result in surface-level rather than bulk modifications. To overcome these limitations, additives have been used to lower the energy barrier and to enhance treatment efficiency. For example, noble-metal doping or surface decoration has vastly improved the hydrogen treatment process by enabling reductions at lower temperatures and pressures. Belousov *et al.*[48] reported the effect of Pd doping (0.3 – 0.5 wt.%) on the hydrogen treatment of over a dozen MOs. As shown in (Table 2), Pd doping not only reduced the temperature required for hydrogen treatment but also in some cases increased the overall degree of reduction or enabled reduction in cases where it was previously unattainable. Their findings also revealed that the hydrogen interaction rate is inversely proportional to the metal-oxygen bond strength, especially the surface oxygen bond. Pd doping actually enabled lower than ambient temperature reduction as low as 77 K, though it usually required low-pressure conditions as low as 0.001 kPa. A similar strategy was reported by Paladugu *et al*.[49] using Pt surface decoration to improve CeO_2 reduction. This approach lowered the reduction onset temperature from over 400 ˚C to well below 200 ˚C.

A simple and exciting strategy of hydrogen treatment at ambient conditions has recently been demonstrated by various groups. First applied to VO_2 and several

metals[33], this novel strategy leverages the difference in work function between a metal and a MO along with protons from an acid solution to simultaneously dope the material with electrons and protons. (Figure 2a) illustrates this process schematically, while (Figure 2b) shows an example where a 1 x 1 cm^2 VO_2 sample is immersed in 2 wt.% H_2SO_4 and placed in contact with various metals. The stability of VO_2 depends on the metal's work function relative to VO_2. Metals with a lower work function than VO_2, such as Al, Cu, and Ag, preserved the VO_2 after 5 h of treatment. In contrast, metals with higher work functions, like Pt and Au, caused significant corrosion, evidenced by a distinct color change from light brown to transparent. The calculated work functions were reported as follows: Pt > Au > VO_2 > Cu > Ag > $H_{0.5}VO_2$ > Zn > Al. This process is very efficient as a small piece of metal (~1 mm) can effectively facilitate hydrogenation of a full wafer sized VO_2 sample (>2 in.)

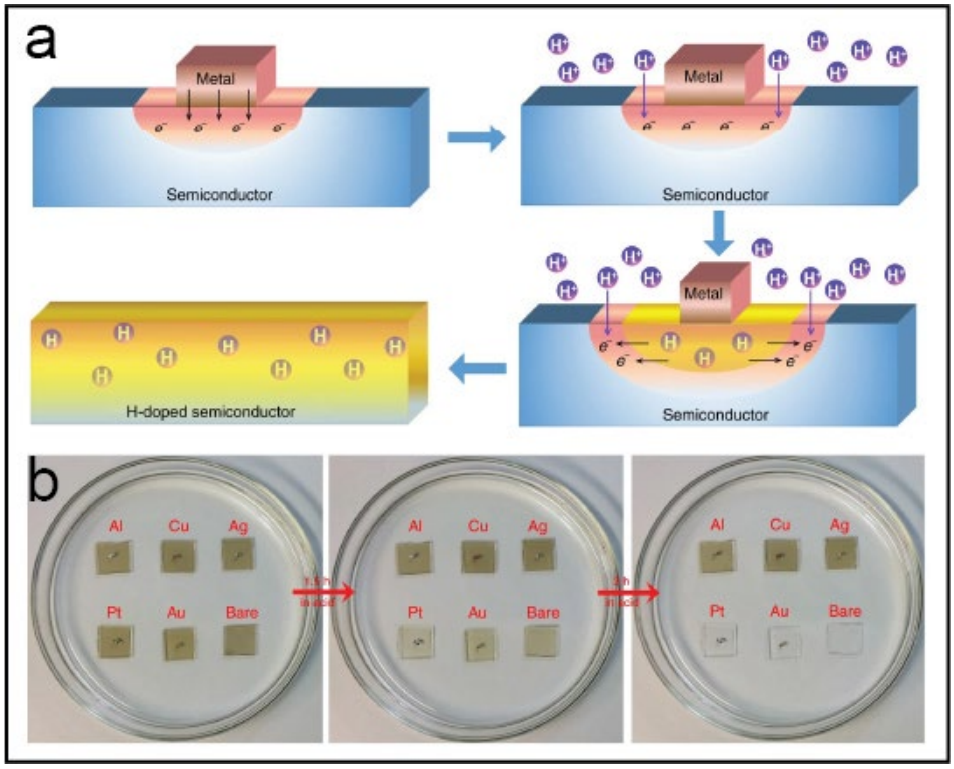

Figure 5.2 (a) The schematic illustration of the contagious electron–proton co-doping mechanism during metal-acid treatment of semiconductor. (b) Metals, such as Al, Cu, Ag, protect M-VO_2 (1 cm × 1 cm size) from corrosion in a 2%wt H_2SO_4 acid solution, whereas Pt and Au, do not.[33] Reproduced from ref. 33. Copyright 2018 Springer Nature.

When a metal (M) contacts a VO_2 film, electrons flow into the semiconductor. Once the metal/VO_2 is immersed into an acid solution, sequential chemical reactions occur:

$$M - x[e^-] \rightarrow M^{x+}$$

$$VO_2 + x[e^-] + x[H^+] \rightarrow H_xVO_2$$

Protons penetrate the VO_2 to combine with electrons, creating a conductive H-doped structure. Meanwhile, the metal is gradually dissolved in acid to form M^+ cations to balance the charges in solution. The process continues as electrons flow from conductive H-doped regions to undoped areas, driving further proton penetration and phase transition. This cycle repeats until full H-doping is achieved.

This same process has been explored further and applied to systems such as WO_3, TiO_2, Nb_2O_5, and MoO_3.[34] For example, anatase TiO_2 (work function 6.67 eV) was treated with an HCl solution in the presence of Zn particles (work function 4.29 eV). The Zn particles injected electrons into the TiO_2, creating a net negative charge that attracted H^+ ions from solution to migrate into the material. Then, protons combined with electrons to form neutral H atoms that donate electron density to oxygen atoms. This mechanism was investigated using DFT simulations, revealing that the negative charge condition created by electron injection into the MO is essential for hydrogenation. Experimentally, if the MO was introduced to the acid solution after the metal particles dissolved, then no hydrogenation was observed, as confirmed by ^{1}H-NMR or ESR measurements. Similarly, no hydrogenation was observed if metals with higher work function than the MO were used. These findings agree with DFT simulations. Furthermore, a greater difference in work function between the metal and MO results in a higher concentration of hydrogen doping, driven by a stronger negative charge condition. This process, of course, depends on the MO's stability in acidic solutions as well as its work function, but it demonstrates

a promising and facile way to induce hydrogen doping of MOs under ambient conditions.

Electrochemical hydrogenation is another post-process method for MOs under ambient conditions.[37] This approach has been applied to a wide variety of MOs such as Nb_2O_3, $BaTiO_3$, TiO_2, WO_3, and $Pb(Zr,Ti)O_3$.[36,37,39,50,51] This process involves immersing the MO electrode in an suitable electrolyte and applying a sufficient DC voltage to electrolyze water at the MO cathode. The resultant hydrogen containing species can interact with the MO surface and even diffuse into the bulk material resulting in effective hydrogen doping. Researchers found that, in addition to surface hydroxyl interactions, there are highly mobile and transient neutral hydrogen species within the crystal. For instance, when an Nb_2O_5 cathode was submerged in a 0.01 M NaOH solution and held at 6 V DC voltage, followed by subsequent immersion in 0.5 M $CuSO_4$, a thin layer of Cu was deposited on the surface (Figure 3a). This demonstrated the presence of reactive, hydrogen-induced properties. (Figure 3b) shows images of the hydrogen-treated sample and the deposited copper layer on the surface. The transient nature of the hydrogen in the Nb_2O_5 was confirmed by time-resolved powder X-ray diffraction and FTIR (Figures 3c and 3d), showing the signals associated with incorporated hydrogen decay over a 10-hour aging period. This behavior followed an exponential decay pattern, as seen by the expansion of the (002) lattice plane (Figure 3e). After 10 hours of aging, the material lost its ability to spontaneously reduce Cu^{2+} ions, suggesting that this capability depended on the transient hydrogen incorporation. Although this method of hydrogen incorporation is

short-lived, it offers valuable insights for developing low-temperature and low-pressure hydrogen treatment techniques for MOs. It reduces energy costs and safety risks while allowing the hydrogenation of thermally unstable MOs that would otherwise be unsuitable for high temperature treatments.

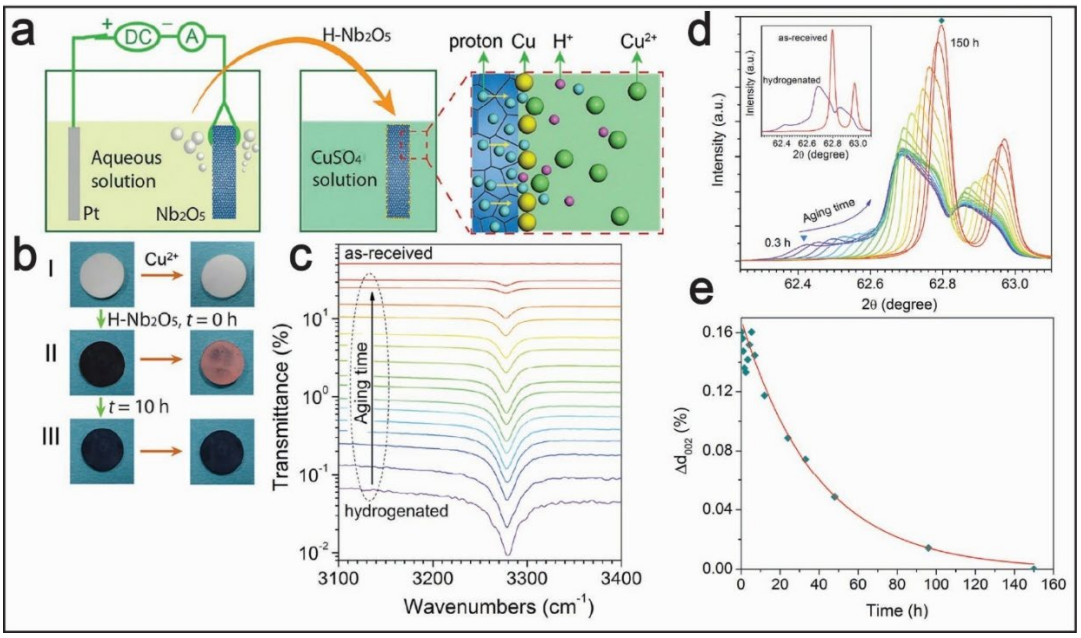

Figure 5.3 (a) schematic illustration of electrochemically hydrogenating an Nb_2O_5 ceramic pellet and then immersing it into a 0.5 M $CuSO_4$ solution at room temperature. (b) Optical images of Nb_2O_5 pellets before and after being immersed in 0.5 M $CuSO_4$ solution for 10 min: I. an as-sintered sample, II. A hydrogenated sample, III. A hydrogenated and 10 h-aged sample. (c) Infrared absorption spectra of an as-received rutile single crystal and a hydrogenated one measured after a series of aging times. The hydrogenation time is 120 h, and the aging times are 2, 9, 24, 34, 48, 72, 144, 192, 310, 500, 750, 1150, 1550, 2400, 3000 h for the spectra from top to bottom. (d) XRD patterns of an electrochemically hydrogenated (001) rutile single

crystal taken after a series of aging time. The hydrogenation time is 200 h, and the aging times are 0.3, 0.5, 0.8, 1.1, 1.7, 2.4, 3.4, 4.3, 5.4, 7, 12, 24, 33, 48, 96, and 150 h for the patterns from left to right. Inset: XRD patterns of an as-received (001) rutile single crystal and the electrochemically hydrogenated (001) rutile single crystal measured at an aging time of 0.3 h. (e) Lattice expansion of the (002) plane of the hydrogenated crystal compared to that of the undoped one as a function of aging time. The red curve is an exponential fit of the data. [37] Reproduced from ref. 37. Copyright 2013 Springer Nature.

Hydrogen incorporation at lower temperatures can also be achieved during the synthesis process. For example, in the chemical synthesis of indium gallium oxide,[27] polyvinyl alcohol, a hydroxyl-rich, low-acidity polymer, was added. Researchers observed improved transport properties of indium gallium oxide, initially unexplained by their studies, subsequent investigations found that these improvements were due to hydrogen doping. This conclusion was supported by both experimental and theoretical evidence. Techniques such as ToF-SIMS, FT-IR, ^{1}H-, ^{71}Ga-, and ^{115}In-MAS NMR spectroscopy confirm hydrogen doping, while *ab initio* simulations of M-OH bonds further validated the findings.

Another controlled approach to hydrogen incorporation during synthesis is through physical vapor deposition techniques, such as sputtering or pulsed laser deposition. When these techniques are performed in a hydrogen-containing atmosphere, hydrogen can be incorporated into the material during formation.[30–32] For example, in the case of sputtered ZnO thin films for optoelectronic devices, hydrogen

incorporation was achieved by adding H_2O to the plasma chamber.[31] The sputtering process was conducted under O_2 and H_2O plasma, which introduces H and OH radicals into the growing ZnO crystal, effectively incorporating hydrogen into its structure.

5.4 Effects of Hydrogen Treatment

Hydrogen treatment can influence the host MO materials in various ways, depending on the treatment outcome, such as surface hydrogenation, bulk hydrogen doping, or effective reduction, *etc*. Generally, hydrogen treatment has been found to improve multiple material properties, including materials' structure, stability as well as their optical and electronic properties, motivating extensive studies on optimizing the process for specific goals.

Structure and Stability

Hydrogen interacts with MOs through two primary mechanisms.[10,52] The first involves the reduction of the MO by inducing oxygen vacancies within the crystal lattice. This usually occurs during post-processing, where an as-synthesized MO is treated in a hydrogen-containing atmosphere. In this process, H_2 molecules typically adsorb onto the MO surface, where they can then dissociate into atomic hydrogen. These H atoms then react with O atoms in the MO lattice to form hydroxyl groups. These hydroxyl groups further react with additional adsorbed H atoms to produce H_2O, resulting in the overall reaction:

$$MO + H_2 \rightarrow M + H_2O$$

This introduction of O vacancies leads to the reduction of metal cations to maintain local charge neutrality in the crystal.[52] This is primarily a surface reaction dependent on the transport and diffusion of O atoms through the crystal to achieve bulk reduction. The formation of oxygen vacancies requires breaking a M—O bond in the MO. Therefore, the degree and rate of reduction are influenced by the strength of the M—O bond, which various among different MOs. Theoretical studies have shown that the energy required to form oxygen vacancies (E_v) correlates with the free energy of formation of the bulk MO, and the formation enthalpy of MOs, an indirect measure of M—O bond strength. Furthermore, Hayashi *et al.*[53] observed that E_v is phase dependent for MOs with the same chemical formula but different crystal structures. This implies that crystal phase, specific crystallographic plane, and defects and disorder can significantly influence E_v and the extent of reduction through hydrogen treatment.

The second mechanism involves the interstitial incorporation of hydrogen into the MO, which often occurs during synthesis or under conditions that promote hydrogen diffusion into the crystal. In hydrogenated MOs, H typically forms covalent bonds with O atoms, a feature observable via infrared spectroscopy, particularly the stretch mode of O—H bond at 3279 cm^{-1}.[37,54] This type of H incorporation, in some cases, can improve the stability of MO crystals, allowing them to exist longer in corrosive acidic environments. Despite the small size of H atoms, interstitial H can cause small changes in the lattice parameters of MOs. The donated electron density from the H atoms to O atoms often reduce nearby metal cations to maintain local

charge neutrality. This reduction can slightly increase the ionic radius of the metal cation, distorting the lattice to accommodate the larger species.[34] Depending on the uniformity of H incorporation and its overall concentration of hydrogen, the induced structural changes can either cause lattice disorder or enhance lattice stability.

More exotic or short-lived forms of hydrogen incorporation in MOs have also been reported, such as highly mobile proton in Nb_2O_5[37] or "invisible" molecular H_2 in ZnO[54]. However, these are rare occurrences. Hydrogen is typically observed as either atomic interstitials within the bulk material or as surface hydroxyls, both contributing to the reduction of the MO.

Optical Properties

The structural changes induced by hydrogen treatment, such as reduction of metal cations and the creation of oxygen vacancies, can significantly impact the optical properties of MO semiconductors. One notable effect is a pronounced color change in the material, suggesting a change in visible light absorption. This effect has been observed in various MOs but is especially prominent in TiO_2. Extensive research has been conducted to understand the underlying mechanisms of these changes. For instance, Chen *et al*.[28] investigated disorder-engineered TiO_2 nanocrystals, which consists of a highly crystalline TiO_2 quantum dot core surrounded by a hydrogen-doped disordered shell (Figure 4). These structures were produced by treating the as-synthesized TiO_2 nanocrystals in a H_2 atmosphere (20 bar) at 200 ˚C for 5 days. The introduction of the engineered disorder is thought to give rise to mid-gap states, which when in large numbers, form a continuum rather than shallow donor states near

the conduction band minimum and valence band maximum (Figure 4a). These continuums near each band edge would overlap and extend into the valance band and conduction band. These are called band tail states and effectively extend the band edge positions above and below the valence and conduction bands.

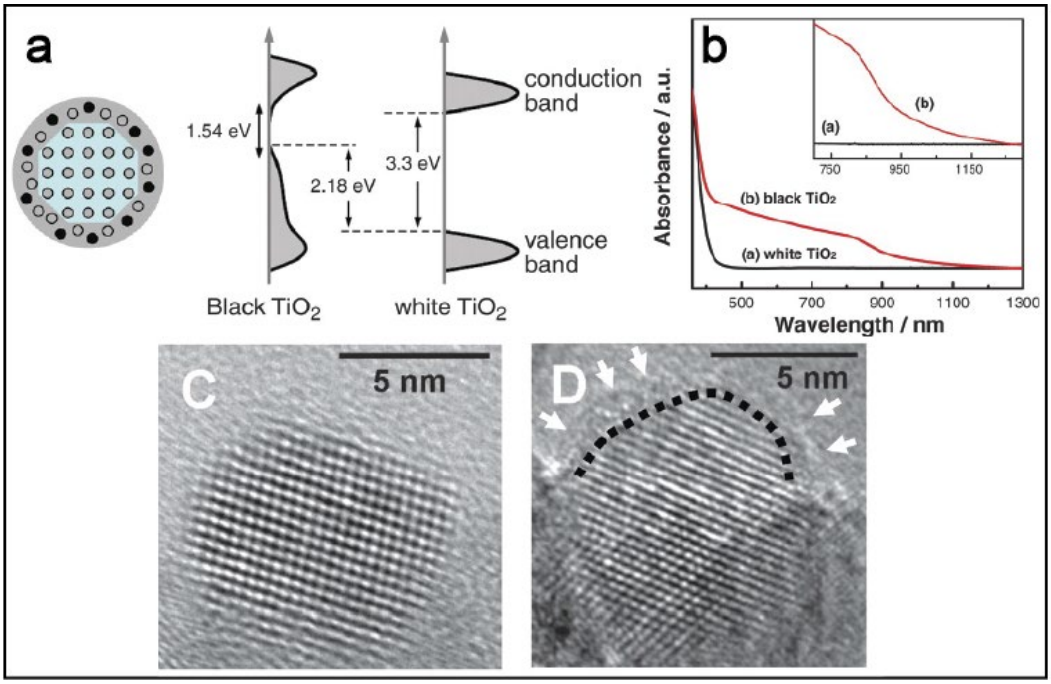

Figure 5.4 (a) Schematic illustration of the structure and electronic density of states of a semiconductor in the form of a disorder-engineered nanocrystal with dopant incorporation. Dopants are depicted as black dots, and disorder is represented in the outer layer of the nanocrystal. The band structures of the white and black TiO_2 are illustrated. The effect of disorder in black TiO_2, which creates broadened tails of states extending into the otherwise forbidden band gap. (b) Spectral absorbance of the white and black TiO_2 nanocrystals. Inset: enlarged absorption spectrum in the range from approximately 750 nm to 1200 nm. (c and d) HRTEM images of TiO_2

nanocrystals before and after hydrogenation, respectively. The dashed line in (d) outlines a portion of the interface between the crystalline core and the disordered outer layer (marked by white arrows) of black TiO_2.[28] Reproduced from ref. 28. Copyright 2011 Science.

Most excitations and relaxations occur within these extended tail states. The effective narrowing of the bandgap increases visible light absorption, as TiO_2 typically only absorbs UV light due to its large bandgap (>3.2 eV). UV-Vis spectroscopy shows a shift in the absorption edge from the UV to near-IR after high temperature hydrogen treatment, supporting the researchers' hypothesis. HRTEM confirmed that the surface shell of the TiO_2 nanocrystals became disordered at a thickness of about 1 nm. These hydrogen-treated, disorder-induced TiO_2 nanocrystals exhibit exceptional photocatalytic activity in decomposition of methylene blue and phenol, and hydrogen production.[28] Valence band XPS measurements revealed that the valence band maximum shifts upward to the vacuum level, effectively reducing the bandgap to ~1.5 eV. DFT calculations of TiO_2 nanocrystals before and after hydrogen treatment further corroborate these findings, aligning well with the experimentally measured density of states.

A similar conclusion was drawn for MoO_3 treated with the proton-electron co-doping strategy.[26] Hydrogen insertion was confirmed using ^{1}H-NMR and EDS elemental analysis. UV-vis-IR absorption spectra of pristine and hydrogenated MoO_3 reveal significantly enhanced visible and infrared absorption in the hydrogenated samples compared to the pristine samples. The results suggested that substantial

bandgap narrowing must have occurred. This effect was further demonstrated in WO_3 and Nb_2O_5 after metal-acid treatment.[26]

Another study on hydrogen-treated TiO_2 suggested that the observed enhancement in photocatalytic activity for hydrogen production was not primarily due to the improved visible light absorption, but rather almost entirely attributed to increased absorption of UV light.[43] This conclusion was supported by incident-photon-to-current-conversion efficiency (IPCE) measurements. Using a monochromator, the photocurrent was measured in response to specific wavelengths of incident light from a solar simulation lamp. The most significant increases in IPCE were observed at wavelengths below ~400 nm, entirely within the UV region. (Figure 5a) inset shows that there was a small increase in IPCE at longer wavelengths, but the contribution remained below 1%. This phenomenon was further studied by integrating the IPCE spectra to calculate the solar to hydrogen efficiency (STH). This removes any error that may arise from varying irradiance spectra from differences in the light sources used in different studies. (Figure 5b) again shows that the majority of increased absorption is in the UV region 400 nm and below. STH increases only very slightly at wavelengths longer than this. In this study, hydrogen treatment was carried out in a hydrogen-containing atmosphere at elevated temperatures, with TiO_2 in the form of vertically aligned nanowire arrays grown directly on a conductive substrate.

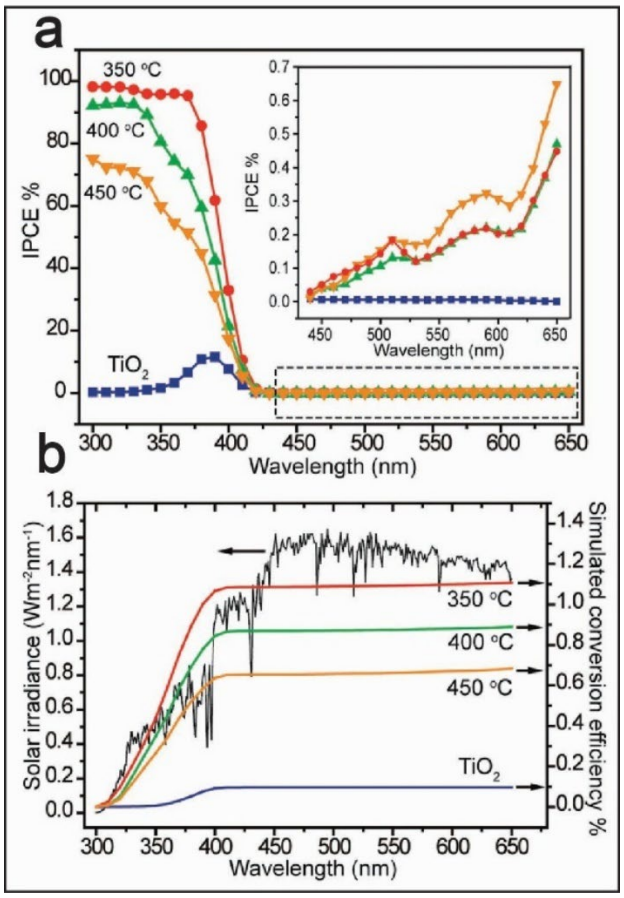

Figure 5.5 (a) IPCE spectra of pristine TiO_2 and H:TiO_2 nanowires prepared at 350, 400, and 450 °C, collected at the incident wavelength range from 300 to 650 nm at a potential of −0.6 V vs. Ag/AgCl. Inset: Magnified IPCE spectra that highlighted in the dashed box, at the incident wavelength range from 440 to 650 nm. (b) Simulated solar-to-hydrogen (STH) efficiencies for the pristine TiO_2 and H:TiO_2 nanowires as a function of wavelength, by integrating their IPCE spectra collected at −0.6 V vs Ag/AgCl with a standard AM 1.5G solar spectrum (ASTM G-173-03).[43] Reproduced from ref. 47. Copyright 2011 American Chemical Society

Cushing *et al.*[24] found that hydrogen treatment does not guarantee improvement in photocatalytic activity. Unlike similar studies, their high temperature hydrogen-treated TiO_2 nanobelts do not show significant improvement over pristine samples. Their results suggested that hydrogen treatment and subsequent chemical reduction from induced oxygen vacancies generate both shallow and deep bandgap states. The extended light absorption range was attributed to valence band-to-defect and defect-to-conduction band transitions. However, the former does not contribute to photocatalytic activity, while the latter has a lifetime too short to effectively drive photocatalysis. These shallow mid-gap states, arising from increased Ti^{3+} concentration due to reduction, are located 0.1-0.2 eV below the conduction band. While they extend the range of photocatalytically active wavelengths by approximately 40 nm, transient absorption measurements indicate a diminished charge carrier lifetime, resulting in no net gain in photocatalytic efficiency. This is in direct contrast with other studies[25,28,41,55–58], photoluminescence and transient absorption measurements carried out by Rex *et al.*[59] and Wheeler *et al.*[60] show that while electron-hole recombination is a problem exacerbated by defect states, improved carrier transport outweighs this for a net improvement in photoelectrochemical performance. Furthermore, it has been shown that photoelectrochemical performance is dependent on treatment temperature.[43,61] As shown in (Figure 5), the higher the treatment temperature, the lower the IPCE, STH, and consequently, the hydrogen production. Samples prepared by Cushing *et al.* were prepared by annealing in hydrogen atmosphere at 600 °C, which may explain the

discrepancy in observed optoelectronic dynamics. This balance of effects can be observed in other MOs studied for photocatalytic or photoelectrochemical applications such as $BiVO_4$[62] and ZnO[63,64] among others. This highlights the importance of sample preparation methods towards desired properties and suggests more thorough study is needed.

Conductivity

In addition to influencing absorption properties of MOs, hydrogen treatment also induces significant changes in their local and bulk electrical properties. One example is how hydrogen treatment notably affects the charge carrier lifetimes of $BiVO_4$.[57] Time-resolved microwave conductivity measurements showed that the minority carrier lifetime (photoinduced holes) more than doubled, increasing from 49 ns to 109 ns in hydrogen-treated samples. These values correspond to an average hole diffusion length of 57 and 101 nm, respectively. However, their carrier mobilities remained nearly unchanged, increasing only slightly from 0.07 $cm^2V^{-1}s^{-1}$ to 0.08 $cm^2V^{-1}s^{-1}$ for hydrogenated samples. These results suggested that hydrogen treatment can increase electrical conductivity in MOs, primarily by extending carrier lifetimes.

Yet, other studies suggest that improvements in electrical conductivity can also be attributed to enhanced carrier mobilities rather than extended carrier lifetimes. This is exemplified by hydrogen-treated In_2O_3, a transparent and conductive MO widely used in solar cells and liquid-crystal display, flat panels, and touchscreens. Koida *et al.*[65] demonstrated that hydrogen treatment could increase the carrier mobility of tin-doped In_2O_3 to 130 $cm^2V^{-1}s^{-1}$, compared to the typical 20-40 $cm^2V^{-1}s^{-1}$

observed in commercially available sample. This enhancement resulted from the elimination of O vacancies and the formation of H donors, which significantly reduced charge carrier scattering. The reduction in scattering occurs because oxygen vacancy act as doubly charged impurities, whereas H—O bonds introduce singly charged defects, thereby mitigating their disruptive effects. The benefits of hydrogen treatment were found to be optimal at a critical hydrogen flow rate of 2.5 sccm. Beyond this threshold, excessive hydrogen incorporation into interstitial sites led to a return of carrier scattering. These findings were further supported by theoretical work from Limpijumnong *et al*.[66]. This remarkable 3-4-fold increase in carrier mobility highlights the substantial improvements in electrical conductivity achievable through hydrogen treatment.

An even more dramatic increase was observed in hydrogen-treated MOs, a phenomenon known as insulator-to-metal transition.[35,67] This electronic phase transition typically occurs at elevated temperatures, where the Fermi level rises sufficiently to populate the conduction band. A theoretical study by Wang *et al.* demonstrated that hydrogen doping not only introduces mid-gap states but also alters the occupancy structure of conduction band edge states.[67] When bulk hydrogen doping is performed, assumed to be via metal-acid treatment, the conduction band of various MOs, including ZnO, TiO_2, and SnO_2, becomes partially occupied, with occupancy levels closely related to hydrogen concentration. Using TiO_2 as an example, inserting a single H atom bonded to an O atom into a Ti_2O_4 unit cell results in a metallic density of states (DOS), as shown in (Figure 6). The formation energy of

this system was found to be negative, suggesting high stability. The H dopant donates electron density to O, forming an H—O bond. The H-dopant electron occupies the Ti 3d orbitals in the conduction band, indirectly reducing neighboring Ti atoms and raising the Fermi level to the conduction band. As a result, an effective insulator-to-metal phase transition occurs under ambient conditions. Introducing a second H atom into the unit cell further increases conduction band occupancy. To confirm that this effect arises from charge transfer by doped H atoms, the researchers selectively removed H atoms from the simulation while keeping all other atom positions fixed. This reversal restored the band gap structure characteristic of a semiconducting or insulating material, confirming that hydrogen doping is responsible for the observed transition.

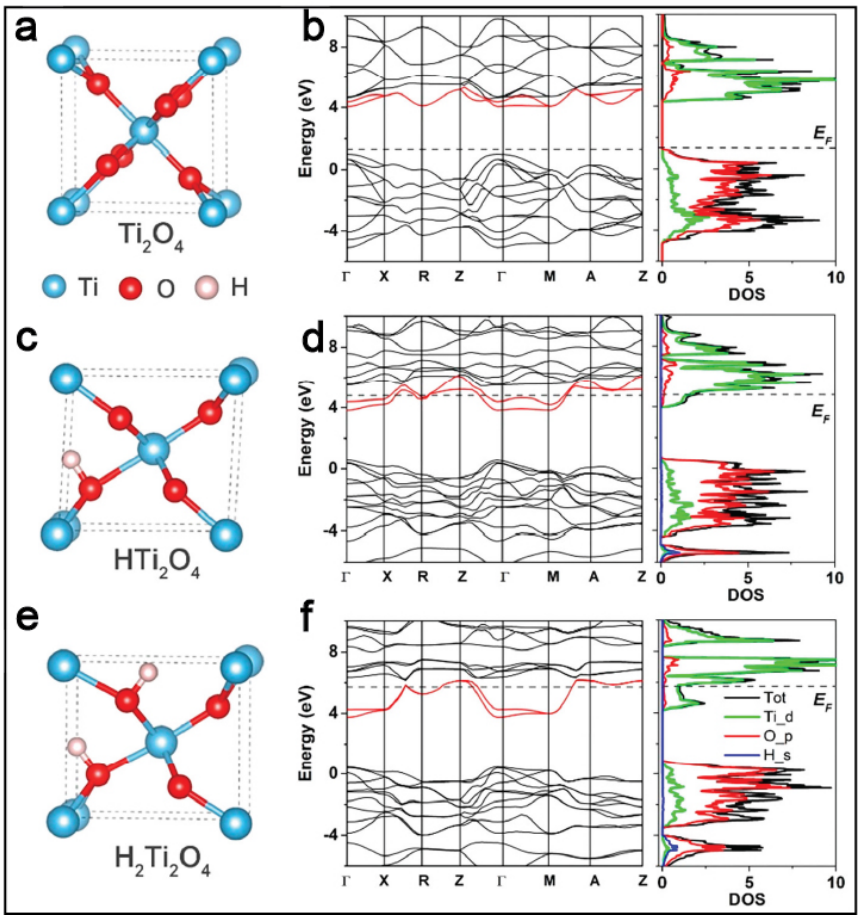

Figure 5.6 Optimized atomic structures, band structures, and DOS of pure rutile TiO_2 and H-doped TiO_2 cells. (a), (c), and (e) are the crystal structures of Ti_2O_4, HTi_2O_4, and $H_2Ti_2O_4$, respectively. (b), (d), and (f) are the electronic structures of Ti_2O_4, HTi_2O_4, and $H_2Ti_2O_4$, respectively.[67] Reproduced from ref. 71. Copyright 202 American Chemical Society.

In contrast, H doping can have the opposite effect when applied to already metallic rutile VO_2.[67,68] While the mechanism remains the same: introducing an H atom bonded to an O atom results in partial reduction of V and the electrons transferred from H occupy the 3d orbital of V. This leads to an upshift of the Fermi

level. With only one H atom per unit cell, the conduction band edge states are not fully occupied, H-doped VO_2 remains metallic. However, when a second H atom is added to the unit cell, these conduction band edge states become fully occupied and result in a metal-to-insulator electronic phase transition.

Magnetism

Hydrogen treatment can have a notable effect on MOs with magnetic properties, such as ferrous and nickel oxides. When Fe oxide nanoparticles were treated in a hydrogen-containing atmosphere at 300 ˚C, some were reduced to metallic Fe, resembling α-Fe and greatly increase nanoparticle size and crystallinity.[4] The presence of hydrogen on the surface and within the nanocrystal made these metallic nanoparticles resistant to oxidation and stable. Hydrogen treatment also induced phase and structural changes that enhanced key magnetic properties, including blocking temperature (T_B), coercive field (H_c), saturation (M_s), and remanence magnetization (M_R). The T_B marks the threshold above which magnetic nanoparticles transition from a frozen state as in bulk materials to a superparamagnetic regime. The H_C measures the material's resistance to demagnetization after being magnetized to saturation, M_s. M_R represents the residue magnetization after the external magnetic field is removed. By increasing these parameters, hydrogen treatment strengthens the material's magnetic properties, primarily through the reduction to metallic Fe and improved crystallinity. The extent of these enhancements can be tuned by controlled variation of temperature and duration of hydrogen treatment.

5.5 Applications of Hydrogen-Treated Metal Oxides

The effects of hydrogen treatment on MOs vary widely depending on the specific treatment method and conditions and the MO system being modified. This diversity makes it difficult to generalize how hydrogen treatment selectively improves certain properties. However, it also opens a range of possible applications where this strategy can be effectively utilized. It is rare that hydrogen treatment is studied solely for synthetic or mechanistic studies, rather it is far more commonly studied to determine the efficacy of hydrogen treatment towards specific functional properties. One key area of interest is the modification of optical properties to improve photocatalytic or photoelectrochemical performance. For example, hydrogen treatment has been applied to MOs used in photocatalytic and photoelectrochemical pollutant degradation, particularly in dye degradation studies. Dyes such as methyl orange or methylene blue[40] are often used model contaminants that can be photocatalytically degraded. In a study on TiO_2 photocatalytic methyl orange degradation, hydrogen-treated TiO_2 completely degraded the dye in 5 min, while pristine TiO_2 required 12 min.[41] Furthermore, samples treated with hydrogen plasma for 8 h showed greater photocatalytic efficiency than those treated for 4 h, both significantly outperform pristine TiO_2.

Moreover, many of the properties improved by hydrogen treatment of MOs have direct application for photocatalytic and photoelectrochemical hydrogen generation[24,28,43,45,55–58,69]. Increased light absorption, whether by expanding the range of wavelengths or increasing absorption efficiency, significantly improves the first

step of these processes. Greater light absorption creates more photogenerated charge carriers, thereby increasing the efficiency of photoelectrochemical devices. A major roadblock for MO semiconductors is their poor electrical conductivity and fast electron-hole recombination rate.[70–73] If the photogenerated charge carriers cannot be effectively separated and transported, then the initial absorption is for naught. Enhancing charge carrier concentration, mobility, and diffusion length is therefore critical for industrially relevant photoelectrochemical materials. (Figure 7) shows the improved performance of hydrogenated TiO_2 nanowires in a photoelectrochemical water-splitting cell.[43] Photoelectrode efficiency is measured directly by the hydrogen gas evolution (Figure 7a) and indirectly by photocurrent over time and linear potential sweep (Figures 7b and c). The improved photocurrent in (Figure 7c) is attributed to a combination of improved absorption as seen in (Figure 5) as well as improved electrical conductivity. (Figure 7d) shows the Mott-Schottky analysis of pristine and hydrogenated photoelectrodes suggesting higher charge carrier density, and thus electrical conductivity. TiO_2 serves as a prototypical photoelectrode system and hydrogen treatment has been studied extensively.

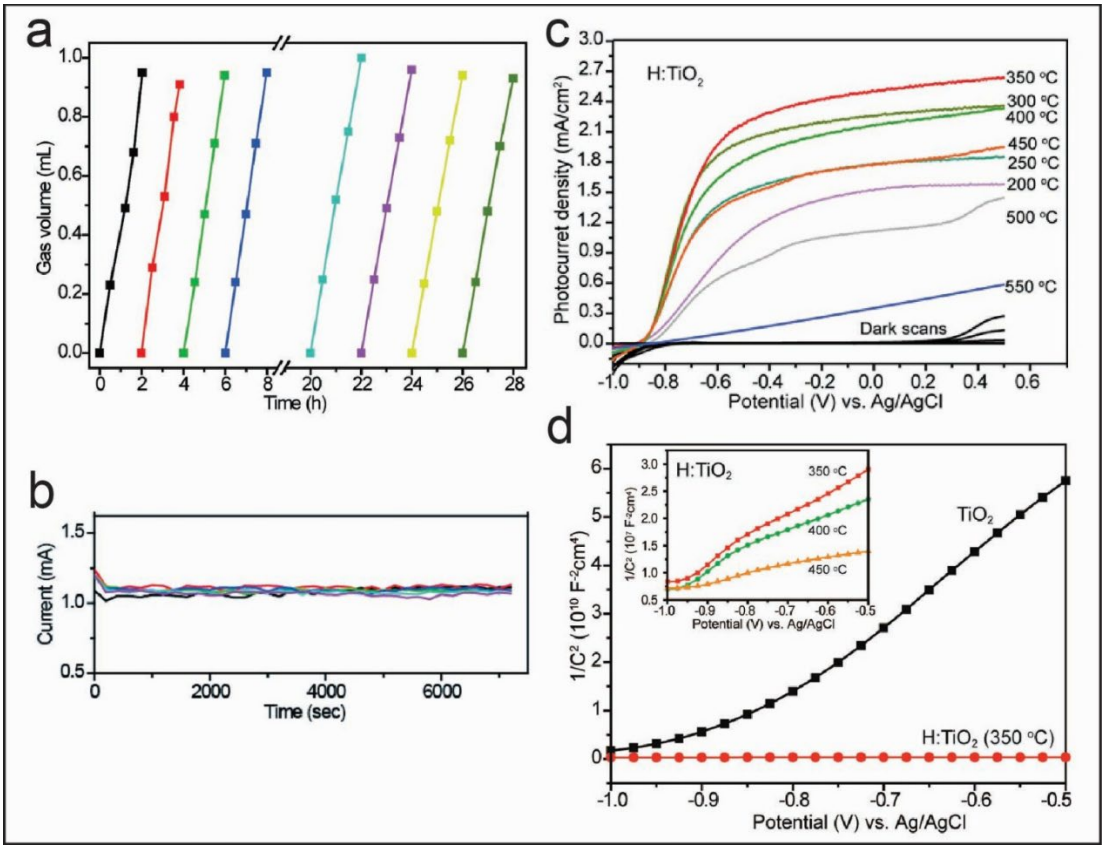

Figure 5.7 (a) Measured gas production of the H:TiO_2 nanowires annealed at 350 °C under at −0.6 V vs Ag/AgCl as a function of time, in a 1 M NaOH solution under 100 mW/cm^2 illumination. (b) The corresponding photocurrent–time profiles obtained for the H:TiO_2 nanowire photoanode during the gas collection cycles. (c) Linear sweeps of H:TiO_2 nanowire arrays prepared at different hydrogen treatment temperatures of 200, 250, 300, 350, 400, 450, 500 and 550 °C, in a 1 M NaOH solution with a scan rate of 50 mV/s under 100 mW/cm^2 illumination. (d) Mott–Schottky plots collected at a frequency of 5 kHz in the dark for the pristine TiO_2 and the H:TiO_2 nanowires annealed at 350 °C. Inset: Mott–Schottky plots of H:TiO_2 nanowires prepared at 350,

400, and 450 °C, collected under the same conditions.[43] Reproduced from ref. 47. Copyright 2011 American Chemical Society.

Employment of hydrogen treatment to tune the electronic properties of MOs and enhance their electrical conductivity is widely demonstrated.[32,57,65–67,74,75] Furthermore, while most MO materials are stable in aqueous electrolyte, water splitting cells are often acidic or basic, which can degrade these materials. Hydrogen treatment has been demonstrated to improve the stability of MOs in acidic environments.[34] This makes hydrogen treatment a promising strategy to make MOs more efficient and stable in photoelectrochemical water splitting.

Beyond photoelectrochemical applications, the improved electrical conductivity of hydrogen-treated MOs has significant implications for electrochemical and electronic technologies. Specifically, hydrogen-treated MOs have been used in electrochemical energy storage devices, such as supercapacitors and battery systems.[6,50,76–79] Supercapacitors are generally categorized into two main types based on their charge storage mechanism: electric double layer capacitors (EDLC) that store charge by charge accumulation at the electrode-electrolyte interface, and pseudocapacitors that rely on Faradaic reactions.[80] Battery systems refer to energy storage mechanisms that rely entirely on redox reactions and/or ion intercalation. MOs are primarily researched for supercapacitive systems; however, despite extensive research on a wide range of MOs, many still display low capacitance—compared to the theoretical values—or poor retention.[81] This can be mitigated to some degree by improving the conductivity of the MOs, which has been

explored through various strategies. Hydrogen treatment has emerged as a cost-effective method to improve electrochemical activity and conductivity of energy storage MOs. Hydrogen treatment creates oxygen vacancies and induces metal reduction, leading to increased carrier concentration and thus conductivity. Additionally, hydrogen treatment promotes surface hydroxylation, offering more active sites for redox processes.[69] (Figure 8) summarizes the work by Lu *et al.* where EDLC-type hydrogenated TiO_2 supercapacitors demonstrate improved cycling stability and capacitance, and low iR-drop, all signs of improved electrical conductivity and capacitive performance. This culminates in hydrogen treated samples showing a 40-fold improvement over untreated samples.

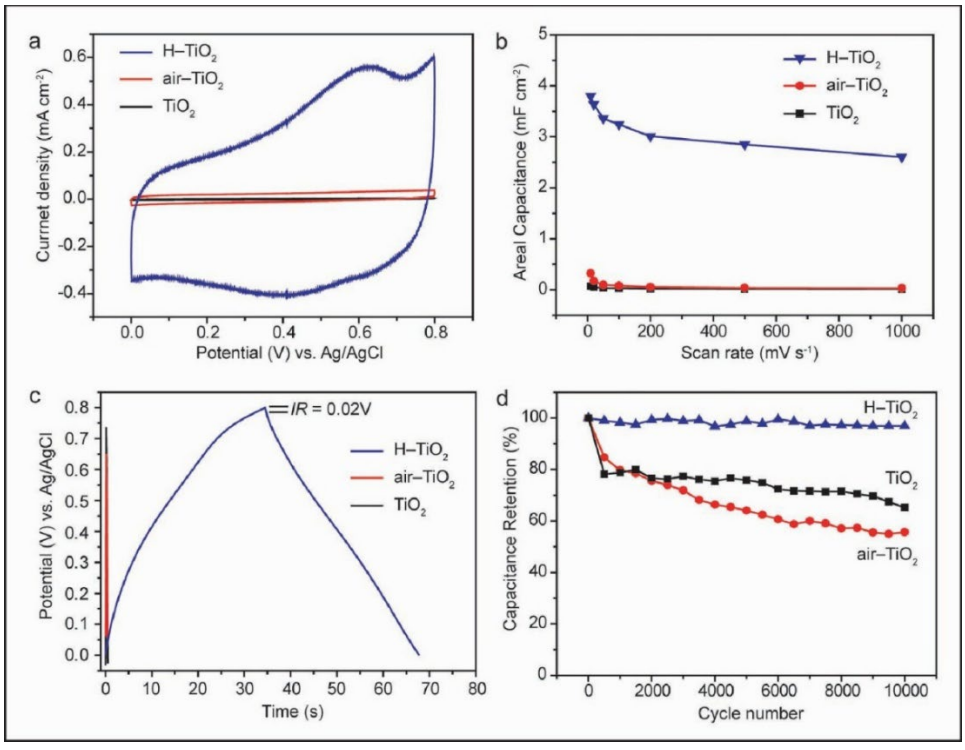

Figure 5.8 (a) CV curves of the untreated TiO_2, air–TiO_2, and H–TiO_2 NTAs obtained at a scan rate of 100 mV s^{-1}. (b) Areal capacitance of TiO_2 samples measured as a

function of scan rate. (c) Galvanostatic charge/discharge curves of TiO_2 samples collected at a current density of 100 μA cm^{-2}. (d) Cycle performance of TiO_2 samples measured at a scan rate of 100 mV s^{-1} for 10 000 cycles.[6] Reproduced from ref. 6. Copyright 2012 American Chemical Society.

These same effects also hold great promise for advancing electrical components and computing technologies. One such application is the memory resistor (or "memristor"), a fundamental electrical component similar to resistors, capacitors, and inductors.[82] Memristors are unique in their ability to retain previous states without power, making them valuable for memory storage and logic circuits, particularly in neuromorphic computing. Traditional memristors consist of two terminals, with resistance determined by the voltage and current previously applied.[83] More advanced three-terminal memristors has gained popularity by offering greater stability and the ability to modulate its resistive behavior. The key mechanism behind memristive behavior is the electrochemical migration of oxygen vacancies in MOs. Under external voltage, oxygen vacancies can be redistributed and causing a shift to a low resistance state.[82] This state change is reversible and can be precisely controlled through the external voltage, enabling the analog memory function of memristors. Since this mechanism relies on oxygen vacancies in MO materials, hydrogen treatment offers a powerful tool for tuning the properties of memristor materials.

Hydrogen treatment can also modify the magnetic properties of MOs, broadening their applications across multiple fields. Magnetic MOs have been used in a range of biomedical applications, including targeted drug delivery[84] and

imaging[85,86], catalysis[87,88], sensors[89], memory storage[82], and environmental remediation[90]. Magnetic properties pose a whole other dimension to these technologies that non-magnetically active materials cannot achieve. For instance, superparamagnetic Fe_3O_4 nanoparticles have been used to selectively release doxorubicin, an anticancer drug[84], in response to external magnetic field. Similarly, α-Fe_2O_3 nanoparticles exhibit magnetically dependent behavior when used as NO_2 gas sensors.[89]

MOs are among the most widely studied materials, playing a crucial role in almost every application involving inorganic semiconductors. Given that hydrogen treatment significantly affects fundamental properties of MOs, such as light absorption, electrical conductivity, and crystal structure, it is an important area of research. Decades of research have demonstrated its benefits across energy conversion and storage, lighting, electronics, computing, making it a valuable strategy wherever MOs are utilized.

5.6 Conclusion

The hydrogen treatment of MOs has emerged as a versatile and impactful method for modifying the properties of these materials, with significant implications for various applications such as photovoltaics, photoelectrochemical systems, batteries, and supercapacitors. This review has provided a comprehensive overview of various hydrogen treatment methods, including post-growth techniques like hydrogen or water annealing, electrochemical hydrogenation, and proton-electron co-doping, as well as processes during MO synthesis such as chemical synthesis and PVD methods.

Each technique offers unique advantages and challenges, contributing to the growing field of hydrogen-treated MOs.

Recent advancements have significantly improved our understanding of the mechanisms and effects of hydrogen incorporation, particularly how hydrogen interacts with material's surface and bulk to induce defects like oxygen vacancies or metal reduction. Researchers have successfully demonstrated how hydrogen treatment enhances electrical conductivity, catalytic activity, and material stability in various MOs, supporting by extensive characterization studies. However, a more detailed mechanistic understanding remains elusive, particularly regarding atomic-level interactions and the role of different hydrogen species in various MOs. While recent theoretical studies have provided valuable insights,[27,66,67,74] more experimental data is required to validate these models.

The long-term stability of hydrogen-doped MOs under operational conditions represents a major challenge. Key questions include: How long do hydrogen-induced properties persist? What is the rate of degradation over time? How does hydrogen diffusion or reoxidize, and can its stability be improved? Developing strategies to enhance durability and prevent degradation will be essential for real-world implementation. Furthermore, for hydrogen treatment to be industrially viable, the process must be scalable and energy efficient. Additionally, exploring hydrogen treatment in novel and less-studied MOs, such as complex or mixed oxides, could uncover new materials with unique properties and applications. Expanding research

beyond MOs to other material classes may also reveal different hydrogen-host material interactions and novel functionalities.

In general, the interest in hydrogen treatment research has declined in recent years, after peaking in the previous decade. However, the wealth of positive results and open questions should serve as a catalyst to revitalize the field. Continued exploration of hydrogen treatment methods and their effects could lead to groundbreaking advancements in material science, energy conversion and storage, and beyond.

Table 1 A non-exhaustive list of hydrogen treatment methods. Note: applications listed as "study" refer to papers with no specific application but rather study the effects of hydrogen treatment.

MO	Treatment	Relevant Conditions	Application	Reference
Nb_2O_5	Post-process	440 ˚C, 4% H_2/Ar, 20 min	Li+ battery electrode	[1]
Fe_2O_3 Fe_3O_4	Post-process	200-300 ˚C H_2 flow rate 100 mL min^{-1} 4 h	Study	[4]
TiO_2	Post-process	300-600 ˚C, H_2 gas flow 60 min	Supercapacitor	[6]
$LiCoO_2$	Post-process	300-600 ˚C, 5% H_2/Ar, 30 min	Photoelectrode	[7]
$Fe_1Co_1O_x$	Post-process	200-400 ˚C, H_2 2.0-4.0 Mpa,	Photoelectrode	[8]
TiO_2	Post-process	600 ˚C H_2 flow rate 0.2 L min^{-1} 3 h	Photocatalyst	[24]

TiO_2	Post-process	500 ˚C H_2 gas flow 1 h	Study	[25]
MoO_3 Nb_2O_5 WO_3	In-process	100 mL conc. HCl, superfluous Zn granules	Study	[26]
InGaO	In-process	polyvinyl alcohol in aqueous solution-process	Transistor	[27]
TiO_2	Post-process	200 ˚C, 20.0 bar H_2 5 days	Photocatalyst	[28]
$InGaZnO_4$	In-process	room temperature, hydrogen content 10^{20} cm^{-3}, O_2 and Ar gas flow 20 mL min^{-1}, total pressure 0.55 Pa	Transistor	[30]
ZnO	In-process	room temperature, O_2 + H_2O at 90 mTorr	Study	[31]
In_2O_3	In-process	room temperature, O_2 and Ar gas at 0.5 Pa, 2.8% H_2/Ar gas flow rate 0-700 mL min^{-1}	Photovoltaic	[32]
VO_2	Post-process	Al, Cu, Ag, Zn, or Fe in 2 wt.% H_2SO_4	Study	[33]
MoO_3 Nb_2O_5 TiO_2 WO_3	Post-process	Al, Zn, Cu, or Ag in conc. HCl	Study	[34]
WO_3	Post-process	0.01 M NaOH, 3 V DC cathode	Study	[36]

Nb_2O_5	Post-process	0.01 M NaOH, 6 V DC cathode,	Redox agent	[37]
TiO_2	Post-process	500 ˚C, H_2 gas flow	Photoelectrode	[38]
$BaTiO_3$	Post-process	0.01 M NaOH, 4.6 V DC cathode, 80 h	Study	[39]
WO_3	Post-process	250-500 ˚C, H_2 flow rate 50 mL min^{-1}, 1 bar, 20 min	Photoelectrode	[44]
SnO_2	Post-process	230-430 ˚C, atomic H from hotwire, plasma decomposition	Photovoltaic	[47]
TiO_2	Post-process	0.01 M NaOH	Study	[50]
$Pb(Zr,Ti)O_3$)	Post-process	0.1 M NaOH, 100 mA cm^{-2}, 6-48 h	Study	[51]
$BiVO_4$	Post-process	300 ˚C, 2.4% H_2/Ar, 10 min	Photoelectrode	[57]
MnO_2	Post-process	350 ˚C, H_2 flow rate 30 mL min^{-1}, 10 min	Photoelectrode	[91]
CeO_2	Post-process	600 ˚C, 10% H_2/Ar, 4 h	Photoelectrode	[92]
TiO_2	Post-process	200-550 ˚C, H_2 gas flow, 30 min	Photoelectrode	[43]
$Na_2Ti_3O_7$	Post-process	450 ˚C, 5% H_2/Ar, 2 h	Battery anode	[76]
ZnO	In-process	140 ˚C, Diethylzinc, H_2O	Memristor	[82]

Table 2 Temperature of reduction onset and H_2 capacity of various pure and Pd-doped oxides[48].

Oxide	**Surface area (*S*, m^2/g)**	**The temperature of initial reduction (*T*, K)**		**Capacity H_2 (cm^3/g (P_{H_2}=0.700kPa))**
Fe_2O_3	12.5	473	–	–
Pd-Fe_2O_3	12	–	293	0.01
WO_3	2.5	700	–	–
Pd-WO_3	2.5	–	293	0.01
MoO_3	3	700	–	–
Pd-MoO_3	3	–	293	0.01
V_2O_5	11	693	–	–
Pd-V_2O_5	11	–	293	0.01
Sb_2O_3	14	393	–	–
Pd-Sb_2O_3	14	–	293	0.01
PbO_2	28	493	–	–
Pd-PbO_2	28	–	293	0.01
U_3O_8	2.5	–	–	–
Pd-U_3O_8	2.5	–	293	0.01
Cr_2O_3	40	473	–	–

Pd-Cr_2O_3	40	–	293	0.01
NiO + Ni_2O_3	170	330	–	–
Pd (NiO + Ni_2O_3)	170	–	293	0.10
CuO	100	300	–	3
Pd-CuO	100	–	293	50
Co_3O_4	140	293	–	15
Pd-Co_3O_4	135	–	293	180
MnO_2	180	293	–	2.5
Pd-MnO_2	180	–	293	286
PdO	–	–	293	110
Ag_2O	1.3	–	293	1.5

5.7 References

1. Kim, K.; Kim, M.-S.; et al. *Chem. Mater.* **2016**, *28* (5), 1453–1461.
2. Asif, A. H.; Wang, S.; et al. *Current Opinion in Green and Sustainable Chemistry* **2021**, *28*, 100447.
3. Butson, J. D.; Narangari, P. R.; et al. *ACS Appl. Mater. Interfaces* **2019**, *11* (28), 25236–25242.
4. Greculeasa, S. G.; Palade, P.; et al. *Sci Rep* **2020**, *10* (1), 17174.
5. Cheng, Z. X.; Li, A. H.; et al. *Journal of Applied Physics* **2008**, *103* (7), 07E507.
6. Lu, X.; Wang, G.; et al. *Nano Lett.* **2012**, *12* (3), 1690–1696.
7. Kang, J.; Tang, D.; et al. *Ind. Eng. Chem. Res.* **2023**, *62* (9), 3882–3888.
8. Zhuang, L.; Jia, Y.; et al. *Nano Res.* **2018**, *11* (6), 3509–3518.
9. Lany, S. *J. Phys.: Condens. Matter* **2015**, *27* (28), 283203.
10. Zhuang, G.; Chen, Y.; et al. *Sci. China Mater.* **2020**, *63* (11), 2089–2118.
11. Li, M.; Yang, Y.; et al. *Nano Lett.* **2017**, *17* (4), 2490–2495.
12. Berglund, S. P.; Rettie, A. J. E.; et al. *Phys. Chem. Chem. Phys.* **2012**, *14* (19), 7065.
13. Zhang, X.; Klaver, P.; et al. *J. Phys. Chem. C* **2016**, *120* (32), 18201–18208.
14. Dai, Z.; Qin, F.; et al. *ACS Catal.* **2016**, *6* (5), 3180–3192.
15. Machreki, M.; Chouki, T.; et al. *ACS Omega* **2023**, *8* (37), 33255–33265.
16. Smart, T. J.; Ping, Y. *J. Phys.: Condens. Matter* **2017**, *29* (39), 394006.
17. Kofstad, P. *Oxid Met* **1995**, *44* (1), 3–27.
18. Sun, Y.; Chen, L.; et al. *Catalysts* **2016**, *6* (12), 188.

19. Hou, J.; Li, Y.; et al. *ACS Appl. Mater. Interfaces* **2014**, *6* (17), 14981–14987.
20. Toe, M. Z.; Pung, S.-Y.; et al. *Journal of Luminescence* **2021**, *229*, 117649.
21. Liu, G.; Yu, J. C.; et al. *Chem. Commun.* **2011**, *47* (24), 6763–6783.
22. Comini, E.; Baratto, C.; et al. *Progress in Materials Science* **2009**, *54* (1), 1–67.
23. Kumbhakar, P.; Chowde Gowda, C.; et al. *Materials Today* **2021**, *45*, 142–168.
24. Cushing, Scott. K.; Meng, F.; et al. *ACS Catal.* **2017**, *7* (3), 1742–1748.
25. Naldoni, A.; Allieta, M.; et al. *J. Am. Chem. Soc.* **2012**, *134* (18), 7600–7603.
26. Cheng, S.; Pan, X.; et al. *Chemical Engineering Journal* **2021**, *417*, 127980.
27. Huang, W.; Chien, P.-H.; et al. *Proceedings of the National Academy of Sciences* **2020**, *117* (31), 18231–18239.
28. Chen, X.; Liu, L.; et al. *Science* **2011**, *331* (6018), 746–750.
29. Rukini, A.; Rhamdhani, M. A.; et al. *J. Sustain. Metall.* **2022**, *8* (1), 1–24.
30. Tang, H.; Ishikawa, K.; et al. *Journal of Applied Physics* **2015**, *118* (20), 205703.
31. Hossein-Babaei, F.; Alizadeh, A. *J Mater Sci: Mater Electron* **2024**, *35* (20), 1420.
32. Li, S.; Shi, Z.; et al. *Journal of Alloys and Compounds* **2017**, *705*, 198–204.
33. Chen, Y.; Wang, Z.; et al. *Nat Commun* **2018**, *9* (1), 818.
34. Xie, L.; Zhu, Q.; et al. *J. Am. Chem. Soc.* **2020**, *142* (9), 4136–4140.
35. Zhu, Q.; Jiang, S.; et al. *Advanced Materials* **2020**, *32* (50), 2004059.
36. Chen, W. P.; Zhu, X. F.; et al. *J Mater Sci* **2007**, *42* (7), 2524–2527.
37. Chen, W. P.; He, K. F.; et al. *Sci Rep* **2013**, *3* (1), 1–5.

38. Harris, L. A.; Schumacher, R. *J. Electrochem. Soc.* **1980**, *127* (5), 1186.

39. Chen, W. P.; Jiang, X. P.; et al. *Journal of the American Ceramic Society* **2003**, *86* (4), 735–737.

41. Wang, Z.; Yang, C.; et al. *Advanced Functional Materials* **2013**, *23* (43), 5444–5450.

42. Leshuk, T.; Parviz, R.; et al. *ACS Appl. Mater. Interfaces* **2013**, *5* (6), 1892–1895.

43. Wang, G.; Wang, H.; et al. *Nano Lett.* **2011**, *11* (7), 3026–3033.

44. Wang, G.; Ling, Y.; et al. *Energy Environ. Sci.* **2012**, *5* (3), 6180–6187.

45. Vequizo, J. J. M.; Kato, K.; et al. *J. Phys. Chem. C* **2023**, *127* (22), 10411–10418.

46. Sabat, K. C.; Rajput, P.; et al. *Plasma Chem Plasma Process* **2014**, *34* (1), 1–23.

47. Wallinga, J.; Arnoldbik, W. M.; et al. *J. Phys. Chem. B* **1998**, *102* (32), 6219–6224.

48. Belousov, V. M.; Vasylyev, M. A.; et al. *Chemical Engineering Journal* **2003**, *91* (2), 143–150.

49. Paladugu, S.; Metz, P. C.; et al. *J. Phys. Chem. C* **2023**, *127* (7), 3689–3697.

50. Chen, W. P.; Wang, Y.; et al. *Applied Physics Letters* **2004**, *84* (1), 103–105.

51. Shafiei, A.; Nickchi, T.; et al. *Applied Physics Letters* **2011**, *99* (21), 212903.

52. Michalsky, R.; Botu, V.; et al. *Adv Energy Mater* **2015**, *5* (7), 1401082.

53. Hayashi, E.; Yamaguchi, Y.; et al. *J. Am. Chem. Soc.* **2019**, *141* (2), 890–900.

54. Shi, G. A.; Saboktakin, M.; et al. *Applied Physics Letters* **2004**, *85* (23), 5601–5603.

55. Liu, N.; Schneider, C.; et al. *Nano Lett.* **2014**, *14* (6), 3309–3313.

56. Amano, F.; Nakata, M.; et al. *J. Phys. Chem. C* **2016**, *120* (12), 6467–6474.

57. Jang, J.-W.; Friedrich, D.; et al. *Advanced Energy Materials* **2017**, *7* (22), 1701536.

58. Ros, C.; Fàbrega, C.; et al. *J. Phys. Chem. C* **2018**, *122* (6), 3295–3304.

59. Rex, R. E.; Yang, Y.; et al. *J. Phys. Chem. C* **2016**, *120* (6), 3530–3541.

60. Wheeler, D. A.; Ling, Y.; et al. *J. Phys. Chem. C* **2013**, *117* (50), 26821–26830.

61. Yang, Y.; Ling, Y.; et al. *European Journal of Inorganic Chemistry* **2014**, *2014* (4), 760–766.

62. Wang, G.; Ling, Y.; et al. *J. Phys. Chem. C* **2013**, *117* (21), 10957–10964.

63. Cooper, J. K.; Ling, Y.; et al. *J. Phys. Chem. C* **2012**, *116* (33), 17360–17368.

64. Lu, X.; Wang, G.; et al. *Chem. Commun.* **2012**, *48* (62), 7717–7719.

65. Koida, T.; Fujiwara, H.; et al. *Jpn. J. Appl. Phys.* **2007**, *46* (7L), L685.

66. Limpijumnong, S.; Reunchan, P.; et al. *Phys. Rev. B* **2009**, *80* (19), 193202.

67. Wang, Z.; Wang, X.; et al. *J. Phys. Chem. Lett.* **2020**, *11* (3), 1075–1080.

68. Pofelski, A.; Jia, H.; et al. *Nano Lett.* **2024**, *24* (6), 1974–1980.

69. Yan, Y.; Cheng, X.; et al. *ACS Sustainable Chem. Eng.* **2019**, *7* (1), 885–894.

70. Cheng, C.; Zhang, W.; et al. *Energy Science & Engineering* **2022**, *10* (4), 1526–1543.

71. Wang, Z.; Huang, H.; et al. *Applied Physics Reviews* **2021**, *8* (2), 021320.

72. Hsieh, P.-Y.; Wu, J.-Y.; et al. *Arabian Journal of Chemistry* **2020**, *13* (11), 8372–8387.

73. Pesci, F. M.; Wang, G.; et al. *J. Phys. Chem. C* **2013**, *117* (48), 25837–25844.

74. Das, P.; Kiran, N. U.; et al. *J. Phys. Chem. C* **2021**, *125* (29), 16191–16199.

75. Hong, J.; Katsumata, K.; et al. *Acta Materialia* **2016**, *103*, 844–849.

76. Fu, S.; Ni, J.; et al. *Nano Lett.* **2016**, *16* (7), 4544–4551.

77. Zheng, J.; Liu, L.; et al. *ACS Appl. Mater. Interfaces* **2016**, *8* (31), 20074–20081.

78. Wang, N.; Yue, J.; et al. *ACS Appl. Mater. Interfaces* **2015**, *7* (19), 10348–10355.

79. Lu, X.; Yu, M.; et al. *Advanced Materials* **2013**, *25* (2), 267–272.

80. Poonam; Sharma, K.; et al. *Journal of Energy Storage* **2019**, *21*, 801–825.

81. Olabi, A. G.; Abbas, Q.; et al. *Energy* **2022**, *248*, 123617.

82. Son, K.-H.; Kang, K.-M.; et al. *physica status solidi (a)* **2021**, *218* (16), 2000702.

83. Xiao, Y.; Jiang, B.; et al. *Science and Technology of Advanced Materials* **2023**, *24* (1), 2162323.

84. Singh, N.; Nayak, J.; et al. *Materials Science and Engineering: C* **2019**, *100*, 453–465.

85. Sun, X.; Gamal, M.; et al. *Applied Materials Today* **2019**, *15*, 267–279.

86. Kubíčková, L.; Brázda, P.; et al. *Journal of Magnetism and Magnetic Materials* **2019**, *480*, 154–163.

87. Veisi, H.; Moradi, S. B.; et al. *Materials Science and Engineering: C* **2019**, *100*, 445–452.

88. Medina, O. E.; Gallego, J.; et al. *Nanomaterials* **2019**, *9* (3), 401.

89. Hjiri, M.; Aida, M. S.; et al. *Sensors* **2019**, *19* (1), 167.

90. Magro, M.; Baratella, D.; et al. *Colloids and Surfaces B: Biointerfaces* **2019**, *181*, 102–111.

91. Zhuang, Q.; Ma, N.; et al. *Advanced Energy and Sustainability Research* **2021**, *2* (8), 2100030.

92. Lv, L.; Hao, Y.-R.; et al. *ACS Appl. Energy Mater.* **2021**, *4* (5), 5339–5347.

Chapter 6

Conclusion and Outlook

6.1 Summary of Principal Findings

This dissertation has investigated defect engineering strategies across four metal oxide semiconductor systems: hematite, bismuth ferrite, lithium manganese oxide, and a broad survey of hydrogen-treated oxides. with the unifying objective of understanding and overcoming intrinsic material limitations that constrain performance in energy conversion, energy storage, and electronic applications. The principal findings of each study are summarized below.

Hematite Doping and Dopant Oxide Remediation

The study of Sn- and Ge-doped hematite established that dopant oxide phases (SnO_2 and $Fe_8Ge_3O_{18}$) form fractionally above theoretically predicted critical concentrations and increase logarithmically with total dopant loading. Two remediation strategies were evaluated. Rapid thermal quenching using a custom induction heating and ice-bath quenching apparatus did not appreciably reduce dopant oxide formation, suggesting that precipitation occurs during the high-temperature hold rather than exclusively during cooling, or that the cooling was not achieved quickly enough. Post-process alkaline washing (5 M NaOH, 120 °C, 24 h) successfully removed approximately 90% of total dopant, but non-selectively: beneficial lattice-incorporated dopant was dissolved alongside the targeted surface-segregated oxide. This resulted in degraded photoelectrochemical photocurrent and,

most severely, diminished aqueous supercapacitor performance, falling below even pristine hematite. The results demonstrate that dopant spatial distribution, not merely total dopant concentration, is the critical parameter governing device performance, and that surface-segregated dopant species in hematite play a more complex role than simple passivating overlayers.

Bismuth Ferrite Synthesis and Multifunctional Characterization

Four wet-chemical synthesis routes were developed and compared for producing pure and doped $BiFeO_3$. The xerogel nanoparticle route emerged as the most versatile and reproducible, yielding phase-pure ~50 nm particles that accommodated transition metal (Sn, Ge) and lanthanide (Yb, Er) dopants without detectable secondary phases by XRD. Potentiostatic co-electrodeposition suffered from poor Bi:Fe stoichiometric control, while the Pechini sol-gel route provided the best thin-film uniformity and conductivity. Preliminary photoluminescence measurements of Yb/Er co-doped BFO revealed complete quenching of the near-band-edge emission at the high dopant concentrations required for energy transfer upconversion, indicating substantial electronic or structural perturbation whose mechanistic origin requires further investigation. Aqueous pseudocapacitance and lithium-ion battery characterization confirmed the expected electrochemical behavior of BFO nanoparticles, while dielectric measurements showed Sn-doping systematically reduces bulk resistance, consistent with small polaron hopping conduction enhanced by dopant-induced Fe^{2+}/Fe^{3+} pairs.

Gallium-Doped Lithium Manganese Oxide for Lithium Recovery

Ga doping of spinel $LiMn_2O_4$ was demonstrated as an effective strategy for simultaneously improving capacity and cycling stability in electrochemical lithium extraction from dilute aqueous sources. Structural characterization confirmed that Ga^{3+} substitutes at the Mn octahedral site, inducing lattice contraction, suppressing Jahn-Teller distortion, and progressively increasing the Mn^{4+}:Mn^{3+} ratio. At the optimal concentration of 5% Ga (LGMO-5), the material retained 100% capacity over 100 cycles and 85% over 1000 cycles in 50 mM LiCl, compared to approximately 50% retention within 100 cycles for undoped LMO. ICP-OES confirmed that Mn dissolution in LGMO-5 was approximately 40 times lower than in undoped material. LGMO-1 exhibited a notable ~25% capacity enhancement attributed to favorable electronic structure modification with minimal disruption to Li^+ diffusion, while higher doping levels introduced kinetic penalties from lattice contraction. This 1000-cycle aqueous stability substantially exceeds cycling lifetimes reported in the current literature for doped LMO in electrochemical lithium recovery.

Hydrogen Treatment of Metal Oxides

The comprehensive review established that hydrogen treatment is a versatile defect engineering tool capable of modifying structural, optical, electronic, and magnetic properties of metal oxides through multiple mechanisms: surface reduction via oxygen vacancy creation, interstitial hydrogen incorporation, and proton-electron co-doping. Key advances synthesized include the demonstration of

disorder-engineered band tail states for dramatic bandgap narrowing in TiO_2, the 3-4-fold carrier mobility enhancement in hydrogen-treated In_2O_3 through elimination of doubly-charged oxygen vacancy scattering centers, and hydrogen-induced insulator-to-metal transitions in several oxide systems. The review identified three critical gaps: the mechanistic ambiguity between surface reduction and bulk hydrogen doping in most experimental studies, the near-complete absence of long-term stability data for hydrogen-induced modifications under operational conditions, and the incomplete understanding of process-structure-property relationships needed to optimize treatment for specific applications.

6.2 Cross-Chapter Themes

Several themes emerge across the four studies that merit explicit articulation, as they inform both the interpretation of the present results and the design of future investigations.

The Primacy of Dopant Spatial Distribution

A recurring finding is that the location of a dopant atom within a crystal, substitutional versus surface-segregated versus precipitated as a secondary phase, often matters more than the total amount of dopant present. In hematite, surface-segregated Ge contributed to supercapacitor performance but was indiscriminately removed by alkaline washing. In LMO, Ga's effectiveness depends on its substitutional incorporation at the Mn site, where it can modulate the Mn^{4+} Mn^{3+} ratio. In BFO, the distinction between substitutional lanthanide incorporation and

secondary phase formation determines whether upconversion or simply phase impurity results. These observations argue for characterization approaches that provide spatial resolution of dopant distribution such as EXAFS, STEM-EDS mapping, and angle-resolved XPS rather than relying solely on bulk compositional analysis.

The Tension Between Thermodynamic and Kinetic Control

Many of the challenges encountered in this work arise from the tension between equilibrium thermodynamics and practical kinetics. Dopant oxide formation in hematite is thermodynamically favored above the critical concentration, yet kinetic trapping via rapid quenching was insufficient to override it. BFO phase purity is thermodynamically narrow, making kinetic factors during annealing (bismuth volatilization rate, nucleation kinetics of competing phases) decisive. Hydrogen incorporation in metal oxides can be thermodynamically stable (as in proton-electron co-doped systems) or kinetically transient (as in electrochemically hydrogenated Nb_2O_5). Understanding the balance between thermodynamic driving forces and kinetic barriers in each system is essential for rational process design.

6.3 Outlook and Future Directions

Hematite

The incomplete results from the rapid quenching study (Chapter 2) motivate refinement of the approach, potentially using more controlled rapid thermal processing equipment with better temperature regulation and faster quench rates. An

alternative strategy worth exploring is the use of protective surface coatings (e.g., thin Al_2O_3 or TiO_2 layers deposited by atomic layer deposition) applied before high-temperature annealing to physically confine dopants within the lattice. Additionally, in situ or operando X-ray absorption studies during annealing and cooling could directly resolve whether dopant precipitation occurs during the high-temperature hold, during cooling, or both. This is a question that the present work raises but cannot definitively answer. More selective etching conditions (lower temperature, shorter duration, or different alkaline media) should also be explored to see if a window exists for removing dopant oxide while retaining lattice-incorporated dopant.

Bismuth Ferrite

The most immediate priority is confirming or ruling out photon upconversion activity in Yb/Er co-doped BFO using appropriate near-infrared excitation (e.g., 980 nm laser) and anti-Stokes emission detection. If upconversion is confirmed, systematic optimization of Yb and Er concentrations, annealing conditions, and host crystal quality would follow. The complete quenching of near-band-edge emission observed at high lanthanide concentrations demands mechanistic investigation. It is unknown whether the cause is bandgap widening, phase transformation to a solid solution or secondary phase, or severe non-radiative quenching through concentration-dependent cross-relaxation. For energy storage applications, compositing BFO nanoparticles with conductive carbon supports (reduced graphene oxide, carbon nanotubes) is a well-established strategy that should be applied to the xerogel nanoparticles developed here. Finally, achieving meaningful ferroelectric

characterization will require either highly oriented thin films grown by more precise techniques or access to a dedicated ferroelectric measurement system capable of applying the electric field strengths needed for polarization-electric field (P-E) loop measurements on polycrystalline pellets.

Lithium Manganese Oxide

The exceptional 1000-cycle stability of LGMO-5 in pure LiCl electrolyte establishes a strong foundation, but several critical steps remain before practical relevance can be claimed. Testing in real brine matrices containing Na^+, K^+, Mg^{2+}, and Ca^{2+} at industrially relevant ratios and concentrations is essential to evaluate how competing cation co-intercalation affects capacity and selectivity. Quantitative Li^+/Na^+ and Li^+/Mg^{2+} selectivity coefficients should be measured, as selectivity is at least as important as capacity for practical lithium recovery. Post-mortem electron microscopy and XPS of cycled electrodes would reveal whether Ga remains substitutionally incorporated after extended cycling or undergoes redistribution. Electrochemical impedance spectroscopy as a function of cycle number would provide insight into impedance evolution and degradation mechanisms. And evaluation in a continuous flow electrochemical extraction cell would test scalability under conditions closer to industrial operation. The anomalous behavior of LGMO-10, high Mn dissolution despite high Mn^{4+} content, warrants investigation of possible surface segregation or secondary phase formation at high Ga loading.

Hydrogen Treatment

The review in Chapter 5 identifies several research directions that would substantially advance the field. Long-term stability studies tracking the persistence of hydrogen-induced property modifications under operational conditions (photocurrent generation, electrochemical cycling, thermal excursion) are critically needed. Distinguishing surface hydrogenation from bulk interstitial incorporation in a given experimental system requires complementary characterization by techniques such as depth-profiled XPS, secondary ion mass spectrometry (SIMS), neutron diffraction (sensitive to hydrogen positions), and solid-state NMR. The proton-electron co-doping strategy, which enables room-temperature hydrogen treatment without high-pressure equipment, deserves broader application to metal oxide systems beyond the handful studied to date. And computational screening of hydrogen incorporation energetics across a wider range of metal oxide structures and polymorphs could guide the selection of promising candidate materials for hydrogen treatment.

6.4 Concluding Remarks

The work presented in this dissertation demonstrates that defect engineering remains a fertile, necessary, and often underexplored approach for advancing metal oxide semiconductor technology. Each of the four studies contributes both to fundamental understanding and to practical materials development: the hematite work clarifies the consequences of dopant oxide formation and the limits of current remediation strategies; the BFO work establishes accessible synthesis routes and

identifies a novel potential application in photon upconversion; the LMO work achieves a step-change in aqueous cycling stability through gallium doping; and the hydrogen treatment review synthesizes a fragmented literature and charts a course for continued investigation.

The challenges described within like dopant solubility limits, phase competition during synthesis, structural degradation during cycling, ambiguous hydrogen incorporation mechanisms, are not unique to the specific systems studied. They are general challenges of metal oxide defect engineering that will recur in any effort to push these materials toward their theoretical performance limits. The strategies and insights developed in this work are therefore expected to inform research on a broad range of metal oxide systems and applications in the years ahead.